# GM 63963

INTERPRETATION REPORT, HIGH RESOLUTION AEROMAGNETIC AND GAMMA-RAY SPECTROMETRIC SURVEY, LAC DANIEL PROJECT

Documents complémentaires

*Additional Files*

Licence

*License*



Énergie et Ressources naturelles
Québec

# INTERPRETATION REPORT

## High Resolution Aeromagnetic and Gamma-ray Spectrometric Survey

## LAC DANIEL PROJECT
## Kangusulujuak, Northern Quebec

**For:**

**NorthWestern Mineral Ventures Inc.**
36 Toronto Street, Suite 1000
Toronto, Ontario; M5C 2C5
Tel.: (866) 437-9551
Fax: (416) 367-6891
www.northwesternmineral.com

**By:**

**Géophysique Camille St-Hilaire Inc.**
732 Gohier, Montreal
Quebec, Canada, H4l 3J1
Phone: (514) 243-8377



**Project: P08-01-008** **March 2008**

# Table of Content


1.0 INTRODUCTION ..... 1
2.0 GEOLOGICAL CONTEXT ..... 4
2.1 Property Description ..... 4
2.2 Previous Works ..... 4
2.3 Regional Geology ..... 5
2.3 Uranium Mineralization ..... 7
3.0 PRESENTATION OF THE MAGNETIC METHOD ..... 10
3.1 Fundamental ..... 10
3.2 Enhancement of Magnetic Grids ..... 11
3.3 Qualitative Data Interpretation ..... 12
3.4 Quantitative Data Interpretation ..... 12
3.4.1 Power Spectral Analysis ..... 12
3.4.2 Euler Deconvolution Method ..... 13
3.4.3 Depth Calculation, Peters's Technique ..... 14
4.0 PRESENTATION OF THE SPECTROMETRIC METHOD ..... 17
4.1 Fundamental ..... 17
4.2 Distribution of the radio-elements in rocks and soils ..... 19
4.3 Geological Mapping ..... 20
4.4 Direct Detection of Mineralization ..... 21
4.5 Enhancement of Gamma-Ray Spectrometric grids ..... 23
5.0 SURVEY DATA INTERPRETATION ..... 24
5.1 Block ABE ..... 24
5.1.1 Magnetic Data ..... 24
5.1.2 Spectrometric Data ..... 25
5.1.3 Conclusions ..... 26
5.2 Block C ..... 39
5.2.1 Magnetic Data ..... 39
5.2.2 Spectrometric Data ..... 39
5.2.3 Conclusions ..... 39
5.3 Block F ..... 51
5.3.1 Magnetic Data ..... 51
5.3.2 Spectrometric Data ..... 51
5.3.3 Conclusions ..... 52
5.4 Block G ..... 64
5.4.1 Magnetic Data ..... 64
5.4.2 Spectrometric Data ..... 64
5.4.3 Conclusions ..... 65
6.0 CONCLUSIONS ..... 76
REFERENCES ..... 77

# List of Figures

Figure 1: Block Locations ..... 8
Figure 2: Uranium Anomalies and Lac Daniel Project Location ..... 8
Figure 3: Simplified geology of the Lac Daniel Project Area (map 241) ..... 9
Figure 4: The Earth Magnetic Field ..... 10
Figure 5: Total Field Anomaly Shape (Field Inclination: 90°) ..... 16
Figure 6: A Typical Gamma-Ray Spectrum ..... 18
Figure 7: Total Magnetic Intensity Reduced to Pole(Bloc ABE) ..... 27
Figure 8: First Vertical Derivative (Block ABE) ..... 28
Figure 9: Analytic Signal (Block ABE) ..... 29
Figure 10: Total Counts (Block ABE) ..... 30
Figure 11: Potassium (%) (Block ABE) ..... 31
Figure 12: Equivalent Uranium (ppm) (Block ABE) ..... 32
Figure 13: Equivalent Thorium (ppm) (Block ABE) ..... 33
Figure 14: Ratio U/Th (Block ABE) ..... 34
Figure 15: Ratio U/K (Block ABE) ..... 35
Figure 16: Ratio Th/K (Block ABE) ..... 36
Figure 17: Interpretation Map (Block ABE) ..... 37
Figure 18: Magnetic Profiles A and B ..... 38
Figure 19: Total Magnetic Intensity Reduced to Pole (Bloc C) ..... 40
Figure 20: First Vertical Derivative (Block C) ..... 41
Figure 21: Analytic Signal (Block C) ..... 42
Figure 22: Total Counts (Block C) ..... 43
Figure 23: Potassium (%) (Block C) ..... 44
Figure 24: Equivalent Uranium (ppm) (Block C) ..... 45
Figure 25: Equivalent Thorium (ppm) (Block C) ..... 46
Figure 26: Ratio U/Th (Block C) ..... 47
Figure 27: Ratio U/K (Block C) ..... 48
Figure 28: Ratio Th/K (Block C) ..... 49
Figure 29: Interpretation Map (Block C) ..... 50
Figure 30: Total Magnetic Intensity Reduced to Pole (Bloc F) ..... 53
Figure 31: First Vertical Derivative (Block F) ..... 54
Figure 32: Analytic Signal (Block F) ..... 55
Figure 33: Total Counts (Block F) ..... 56
Figure 34: Potassium (%) (Block F) ..... 57
Figure 35: Equivalent Uranium (ppm) (Block F) ..... 58
Figure 36: Equivalent Thorium (ppm) (Block F) ..... 59
Figure 37: Ratio U/Th (Block F) ..... 60
Figure 38: Ratio U/K (Block F) ..... 61
Figure 39: Ratio Th/K (Block F) ..... 62
Figure 40: Interpretation Map (Block F) ..... 63
Figure 41: Total Magnetic Intensity Reduced to Pole (Bloc G) ..... 65
Figure 42: First Vertical Derivative (Block G) ..... 66
Figure 43: Analytic Signal (Block G) ..... 67

Figure 44: Total Counts (Block G) ..... 68
Figure 45: Potassium (%) (Block G) ..... 69
Figure 46: Equivalent Uranium (ppm) (Block G) ..... 70
Figure 47: Equivalent Thorium (ppm) (Block G) ..... 71
Figure 48: Ratio U/Th (Block G) ..... 72
Figure 49: Ratio U/K (Block G) ..... 73
Figure 50: Ratio Th/K (Block G) ..... 74
Figure 51: Interpretation Map (Block G) ..... 75

## List of Tables

Table 1: Block Co-ordinates (WGS84, UTM zone 20N) ..... 2
Table 2: Survey Specifications ..... 3
Table 3: Windows Used in Spectrometric Surveys ..... 18
Table 4: Block AEM, Gamma-Ray Spectrometric Anomalous Targets ..... 25
Table 5: Block AEM, Gamma-Ray Spectrometric Linear Anomalies ..... 26
Table 6: Selected Exploration Targets ..... 76

# 1.0 INTRODUCTION

This report concerns the interpretation of heliborne magnetic and spectrometric data acquired during September 2007 by **Geo Data Solutions Inc.** for **NorthWestern Mineral Ventures Inc. (NorthWestern)**. The survey was flown over four blocks (ABE, C, F and G) located near Kangusulujuak, Northern Quebec. Block locations are shown on figure 1 and table 1 defines their UTM co-ordinates. Numbers of line-kilometers acquired on each block are shown on table 2.

This project was initiated on a major regional uranium anomaly mapped from a bottom lake sediment campaign done in 1997. The primary goal of this airborne geophysical works was to provide high quality digitally recorded and processed geophysical data in order to assist geological mapping and to indicate structures potentially favorable to the presence of uranium mineralization.

All traverse lines were oriented N45°E with a spacing of 200 meters while control-lines were oriented N135°E with a spacing of 1000 meters (table 2). The survey was flown with a helicopter nominal ground clearance of 50 meters.

Geophysical data were sampled with an interval of 3.3 meters along traverse lines and tie-lines. Helicopter and sensors mean terrain clearance were:

- helicopter mean terrain clearances:
  - Block ABE: 48.0 m.
  - Block C: 66.3 m.
  - Block F: 48.3 m.
  - Block G: 49.4 m.
- magnetometer mean terrain clearances:
  - Block ABE: 32.5 m.
  - Block C: 50.8 m.
  - Block F: 32.8 m.
  - Block G: 33.9 m.
- spectrometer mean terrain clearance:
  - Block ABE: 48.0 m.
  - Block C: 66.3 m.
  - Block F: 48.3 m.
  - Block G: 49.4 m.

The following sections present:

- The geological context (section 2)
- An overview of the magnetic method and the interpretation techniques used (section 3)
- An overview of the spectrometric method and the interpretation techniques used (section 4)
- The interpretation results (section 5).

## Table 1: Block Co-ordinates (WGS84, UTM zone 20N)

| Block ABE | | |
|---|---|---|
| Vertex | X(m) | Y(m) |
| 1 | 332996 | 6467481 |
| 2 | 333317 | 6474607 |
| 3 | 332308 | 6475698 |
| 4 | 334490 | 6477892 |
| 5 | 335682 | 6476706 |
| 6 | 338210 | 6476624 |
| 7 | 338582 | 6477022 |
| 8 | 338885 | 6481833 |
| 9 | 338444 | 6482274 |
| 10 | 340884 | 6484708 |
| 11 | 343015 | 6482590 |
| 12 | 344516 | 6484046 |
| 13 | 344497 | 6486077 |
| 14 | 344251 | 6486329 |
| 15 | 347152 | 6489274 |
| 16 | 349327 | 6487042 |
| 17 | 348098 | 6485743 |
| 18 | 347984 | 6484122 |
| 19 | 348476 | 6483630 |
| 20 | 348861 | 6483618 |
| 21 | 348735 | 6480540 |
| 22 | 349435 | 6479847 |
| 23 | 349674 | 6479853 |
| 24 | 350418 | 6476158 |
| 25 | 363818 | 6475647 |
| 26 | 364367 | 6476252 |
| 27 | 365451 | 6475162 |
| 28 | 365086 | 6474821 |
| 29 | 364846 | 6467267 |
| 30 | 373113 | 6466983 |
| 31 | 372924 | 6460690 |
| 32 | 373964 | 6459605 |
| 33 | 371726 | 6457430 |
| 34 | 370477 | 6458666 |
| 35 | 365495 | 6458760 |
| 36 | 365502 | 6461566 |
| 37 | 361611 | 6461674 |
| 38 | 361800 | 6465974 |
| 39 | 361371 | 6466390 |
| 40 | 332989 | 6467412 |
| 41 | 333002 | 6467481 |

| BLOCK C | | |
|---|---|---|
| 1 | 384848 | 6470089 |
| 2 | 383675 | 6471218 |
| 3 | 383241 | 6470794 |
| 4 | 382167 | 6471825 |
| 5 | 382503 | 6472140 |
| 6 | 382720 | 6481149 |
| 7 | 381711 | 6482126 |
| 8 | 383968 | 6484394 |
| 9 | 385043 | 6483320 |
| 10 | 388527 | 6483222 |
| 11 | 388874 | 6483602 |
| 12 | 389558 | 6482983 |
| 13 | 389189 | 6482581 |
| 14 | 390253 | 6481442 |
| 15 | 388060 | 6479228 |
| 16 | 386834 | 6480432 |

| Block G | | |
|---|---|---|
| Vertex | X(m) | Y(m) |
| 1 | 323665 | 6491083 |
| 2 | 323304 | 6490732 |
| 3 | 322214 | 6491832 |
| 4 | 322741 | 6492359 |
| 5 | 322842 | 6495696 |
| 6 | 326605 | 6499459 |
| 7 | 327724 | 6499394 |
| 8 | 328352 | 6500005 |
| 9 | 329203 | 6499256 |
| 10 | 329360 | 6499376 |
| 11 | 329693 | 6499099 |
| 12 | 329517 | 6498877 |
| 13 | 330137 | 6498248 |
| 14 | 329536 | 6497536 |
| 15 | 329480 | 6496094 |
| 16 | 327946 | 6494494 |
| 17 | 327844 | 6491943 |
| 18 | 327104 | 6491277 |
| 19 | 325264 | 6491249 |
| 20 | 325255 | 6491000 |
| 21 | 323647 | 6491074 |

| Block F | | |
|---|---|---|
| 1 | 327271 | 6475577 |
| 2 | 326517 | 6476324 |
| 3 | 327054 | 6476834 |
| 4 | 327074 | 6480012 |
| 5 | 326925 | 6480161 |
| 6 | 327536 | 6480732 |
| 7 | 327387 | 6481126 |
| 8 | 328005 | 6481785 |
| 9 | 327183 | 6484114 |
| 10 | 326952 | 6484427 |
| 11 | 329214 | 6486675 |
| 12 | 330484 | 6485425 |
| 13 | 330280 | 6481139 |
| 14 | 331129 | 6480291 |
| 15 | 330667 | 6479829 |
| 16 | 330613 | 6477975 |
| 17 | 331747 | 6476868 |
| 18 | 329526 | 6474688 |
| 19 | 328399 | 6475835 |
| 20 | 327597 | 6475883 |
| 21 | 327251 | 6475543 |
| 22 | 327264 | 6475584 |

| | | |
|---|---|---|
| 17 | 386215 | 6480226 |
| 18 | 386096 | 6473269 |
| 19 | 387007 | 6472260 |
| 20 | 384848 | 6470089 |

**Table 2: Survey Specifications**

| Block | Traverse Direction | Control Line Direction | Traverse Spacing (m) | Control Line Spacing (m) | Line-Km |
|---|---|---|---|---|---|
| **ABE** | N45°E | N135°E | 200 | 1000 | 2,855 |
| **C** | N45°E | N135°E | 200 | 1000 | 336 |
| **F** | N45°E | N135°E | 200 | 1000 | 208 |
| **G** | N45°E | N135°E | 200 | 1000 | 248 |
| | | | | **Total line-km** | **3,647** |

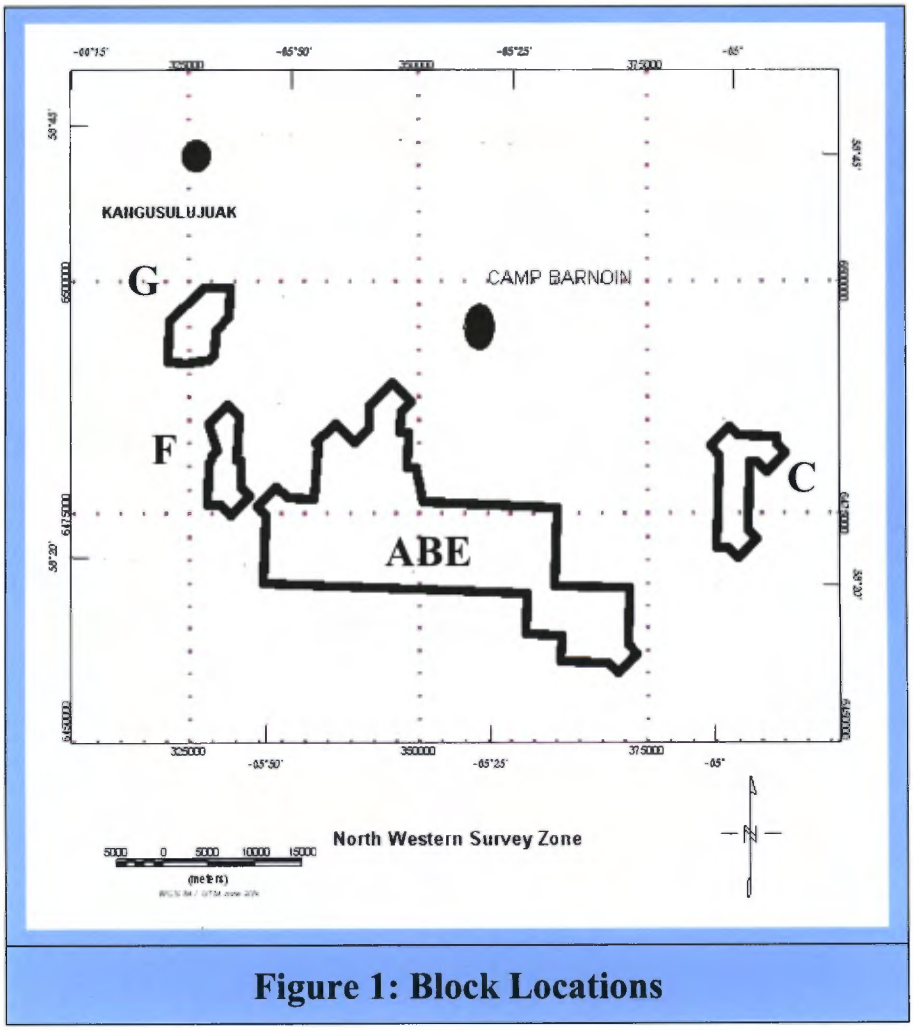


**Figure 1: Block Locations**

# 2.0 GEOLOGICAL CONTEXT

## 2.1 Property Description

The Lac Daniel mag/spec heliborne survey includes 4 blocks, ABE, C, F and G, located near Kangusulujuak, Northern Quebec (figures 1 and 2). The survey area is located between longitudes 64°45' and 66°02' West and latitudes 58°15' and 58°36' North. The survey covers part of the NTS sheet 24I, between the Ungava Bay to the West and the Labrador border to the East.

This territory is under the jurisdiction of the Nunavut regional administration, under the authority of the Kangiqsualujjuaq municipality.

The survey area is a region of highlands that culminate in the east with the Torngat mountain range, where the highest peaks (Mont Iberville) tower at over 1 500 meters of altitude. The main rivers in the area, the George River, which flows from South to North, and the Koroc River, which drains the Torngat Mountains from East to West, are important rivers, with rapid and elevated rate flow over most of their path.

A multitude of small and medium-sized lakes are scattered throughout the area. The most important are Lac Daniel and Lac Tasirlaq.

With the exception of the main valley bottoms, where grow a sparse forest composed of epicea, tamarack, birch, rhododendrons and other shrubs, the forest cover is absent. Soil cover is rare, and most of the area consists of lichen-covered rock outcrops or fields of blocks alternating with mossy, grassy or flowery zones. The area hosts a variety of animals including caribou, black bears, occasionally polar bears, wolfverines, arctic fox, lemmings, hares, as well as numerous species of birds.

## 2.2 Previous Works

(From Girard , 2007)

The area was initially mapped in 1967-1969 at 1:250,000 as part of the "Torngat Project" of the geological survey of Canada (Taylor, 1979). This map is amazingly accurate, considering the conditions in which the fieldwork was carried out. Most of the large lithological units were outlined and the geological framework was identified.

The NTS 24I map sheet was remapped at the same scale in 1997 by the Ministère des Ressources Naturelles du Québec (Verpaelst et al., 2000). This map does not provide significant improvement in terms of accuracy compared to Taylor's (1979). However, some improvements were made to the understanding of the geological framework.

The only geophysical data available is the federal government low-density aeromagnetic survey. A lake-bottom geochemical survey was carried out in 1997 by the Ministère des Ressources Naturelles du Québec. Although no report is available, the original data can be purchased. Lakes were sampled

at a density of one sample per 7 kilometers. Analytical procedure involved ICP-AES after aqua-regia digestion.

Only very limited exploration work has been carried out in this area. Some claims were acquired in 1998 for nickel exploration by the Cambior-Soquem-Virginia consortium, as a follow-up of the abovementioned lake bottom sediments survey. Very limited work has been released from these campaigns. Some prospecting for nickel was carried out the year before, in 1997 for Inco Ltd with no results available. Diamond exploration was carried out in the Koroc River area, to the north of the actual project. No mineral occurrences are known in the area.

Finally, in 2006, **NorthWestern Mineral Ventures Inc**. carried out ground works (geological mapping, rock and soil sampling, lake sediment sampling, hand-held spectrometer) and an airborne mag.-spec. survey on their North Rae property (Girard, 2007). Numerous uranium occurrences were identified.

## 2.3 Regional Geology

(Adapted from Verpaelst and al., 2001)

The Lac Daniel project lies within the eastern part of the Churchill Province. The Churchill consists of a number of Archean cratonic blocks and Early Proterozoic mobile zones, where the peak of metamorphism and deformation occurred at about 1.8 Ga. In northeastern Québec and northern Labrador, the Churchill comprises all Archean and Early Proterozoic rocks located between the Superior and Nain provinces. Their deformation is attributed to the Early Proterozoic Trans-Hudson Orogeny. The Churchill in NE Québec is composed of: the New Québec Orogen (Labrador Trough) in the west, the SE extension of the Rae Province, which we have called the Far North craton, in the central part, and the Torngat Orogen in the east, which links the Far North craton and the Nain Province further east, and which formed during the collision between the two cratons.

The area straddles the eastern margin of the Far North craton and the Torngat Orogen, which contains reworked terrains of the Far North craton and the Nain, as well as a variety of para- and orthogneisses of uncertain affinity wedged between the two cratons.

The Far North craton is divided into four lithodemic and lithostratigraphic units:

1) the Kangiqsualujjuaq Complex, formed during the Early Proterozoic, and composed of a series of tonalitic and granitic orthogneisses cross-cut by Archean granitoid dykes and plutons;
2) the Baudan Complex, also Early Proterozoic in age, composed of Archean granitic gneiss and diatexite, as well as wedges of paragneiss probably correlated to the Lake Harbour Group;
3) the Lake Harbour Group, an Early Proterozoic sequence of paragneiss, quartzite, calcitic and dolomitic marble, calc-silicate rock and metabasalt;
4) the Nuvulialuk mafic Suite composed of Early Proterozoic metamorphosed gabbroic and ultramafic dykes and sills intruding the Lake Harbour Group and the metamorphic complexes.

All these units are metamorphosed to the upper amphibolite facies.

The Torngat Orogen comprises, from west to east (figure 3):

1) the Sukaliuk Complex, a deformed assemblage of tonalitic, enderbitic and charnockitic orthogneisses, paragneiss, quartzite and ultramafic rocks metamorphosed to the granulite facies, which probably correspond to reworked equivalents of units in the Far North craton;
2) the Lomier Complex, composed of anorthositic, enderbitic, mangeritic and charnockitic orthogneisses, with bands and enclaves of paragneiss, granitoid rock and metagabbro;
3) the Tasiuyak Gneiss, a strongly deformed assemblage of granitic gneiss and Early Proterozoic paragneiss;
4) the Iberville Complex, formed of orthogneiss of the AMCG suite, located east of the Tasiuyak Gneiss.

The Torngat Orogen and the rocks of the Far North craton are cross-cut by late mafic dykes that we have assigned to the Falcoz Diabase.

The Far North craton displays an intense foliation, oriented NE-SW and dipping about 20° SE, as well as a strong tectono-metamorphic lineation that plunges 18° to the SE on average, both attributed to the Trans-Hudson Orogeny (Torngat). An early foliation (Archean?) is namely observed in mafic enclaves in the tonalitic gneiss. Contacts between stratigraphic units are defined by reverse faults that are parallel to the main foliation. Dextral and sinistral shear zones oriented NW-SE (such as the Falcoz zone) are interpreted as riedel shears related to major N-S strike-slip faults observed in the Torngat Orogen. Within the Torngat Orogen, the presence of a strong subvertical N-S foliation and a subhorizontal N-S lineation, in addition to predominantly sinistral kinematic indicators are associated with an intense shearing event. Brittle faults parallel to the ductile shear zones are the result of late tectonic activity.

Two tonalitic gneiss units in the Kangiqsualujjuaq Complex (SP-4044A1 and A2) represent lithologies from a Middle Archean (2.9 and 2.76 Ga) basement, reworked during a Late Archean tectono-thermal episode (2.623±0.004 Ga). An age of 1.85 Ga, obtained in an amphibolite, is interpreted as the age of emplacement for this lithology. It most likely indicates the tectonic juxtaposition of the Proterozoic amphibolite with the Archean tonalitic gneisses. A granitic dyke, with an emplacement age of 1.828±0.002 Ga, represents a magmatic event related to the tectono-thermal peak widely recognized in the entire Trans-Hudson Orogen, and which precedes the period of terrain exhumation. Samples from the Baudan Complex granitic gneisses helped pinpoint the occurrence of a Late Archean magmatic event at about 2.6 Ga, which represents both the emplacement of new material and the remobilization of older terrains. Ongoing studies on samples of the Falcoz zone have not yet revealed relevant information concerning the development of the shear zone.

The proposed sequence of events for the Lac Daniel area is as follows:

- the formation of an Archean tonalitic basement with remnants of supracrustal rocks (mainly amphibolites) between 2.920 Ga and 2.76 Ga;

- the intrusion of granitic rocks during the Archean (2.60 Ga - 2.623±0.004 Ga), accompanied by granulite-facies metamorphism and ductile deformation;
- the erosion of a magmatic arc and the emplacement of sediments and lavas of the Lake Harbour Group and the Nuvulialuk intrusive Suite (1.90 - 1.85 Ga), in a fore-arc basin;
- the Trans-Hudson Orogeny : metamorphism and remobilization of basement and supracrustal rocks to form the Baudan and Kangiqsualujjuaq complexes (1.82 - 1.828 Ga); granulitization at depth (Sukaliuk and Lomier complexes and Tasiuyak Gneiss). Deformation in an E-W compressional regime (Nain - Churchill and Churchill - Superior collisions) to generate N-S oriented folds, then transport of units from east to west (development of recumbent folds and thrust zones), thereby bringing rocks from deeper structural levels close to the surface;
- Evolution of the deformation from a compressional to a transpressional regime, generating N-S and NW-SE shear zones (ex: Lac Daniel fault, Falcoz zone), which cut and refold earlier N-S folds. Emplacement of syn- to post-transpressive deformation granite and granitic pegmatite dykes and veins.
- Intrusion of Falcoz Diabase.

## 2.3 Uranium Mineralization

(From Girard, 2007)

Results from ground prospecting and airborne geophysical surveys done in 2006 over an area located North of this project (North Rae project) leaded to the discovery of numerous uranium occurrences. Most of these occurrences are hosted in pink hudsonian pegmatites, injected in gneisses or associated with granites. Values up to 0.5% $U_3O_8$ were obtained on selected samples of pegmatite, on a set of dykes tracked for more than 7 kilometers. Grades of 0.1% $U_3O_8$ were fairly common throughout the properties, either in pegmatites, granites or basement gneisses (Girard, 2007).

Uranium-enriched granites and pegmatites are abundant in the area. According to Cuney (2006), development of giant deposits such as the Athabasca Basin is dependent upon the presence of enriched basement from which uranium is remobilized. North Rae and Lac Daniel areas has a regional enriched basement, so the exploration strategy should be to identify and substantiate potential traps that could precipitate uranium.

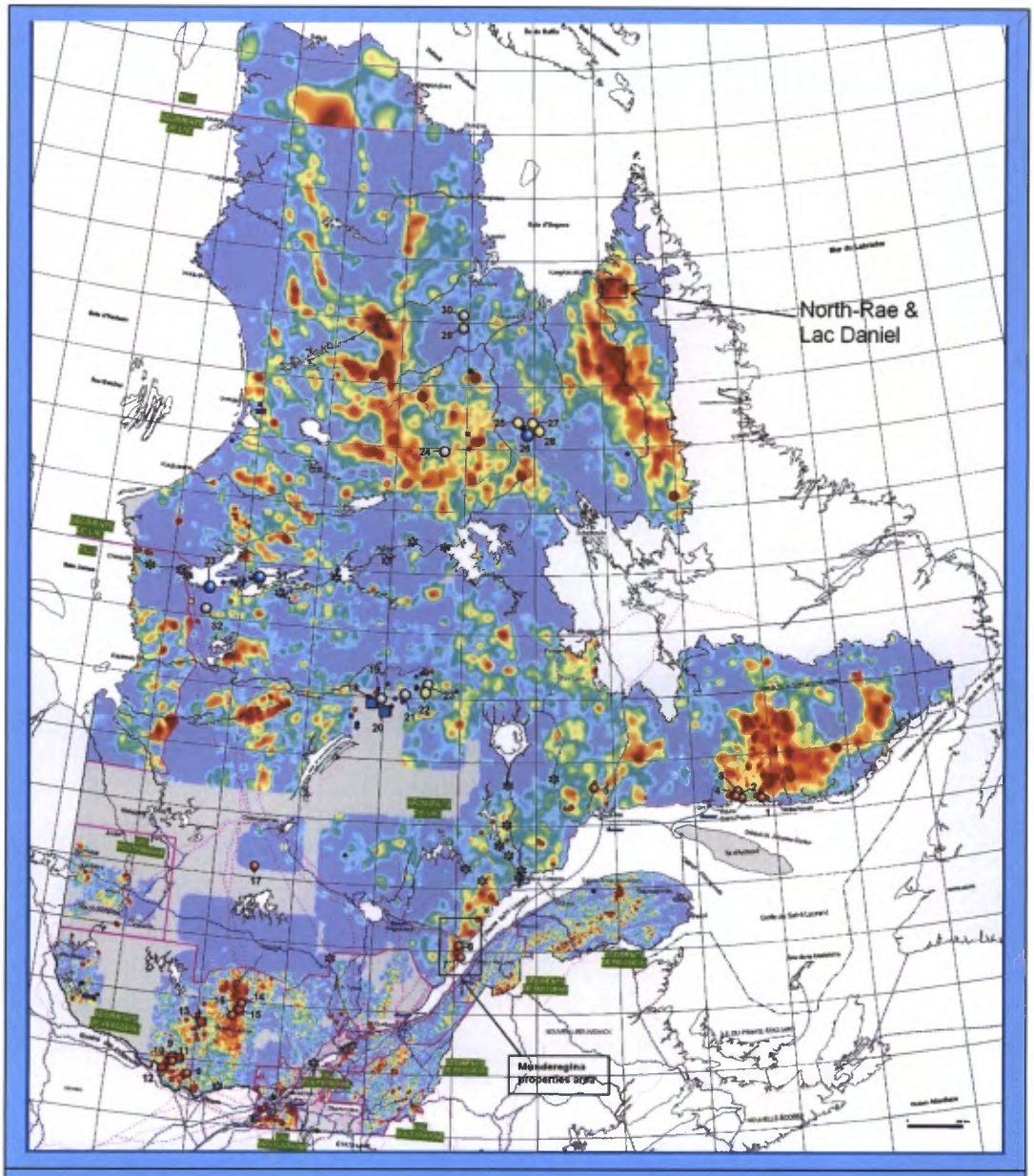


**Figure 2: Uranium Anomalies and Lac Daniel Project Location**

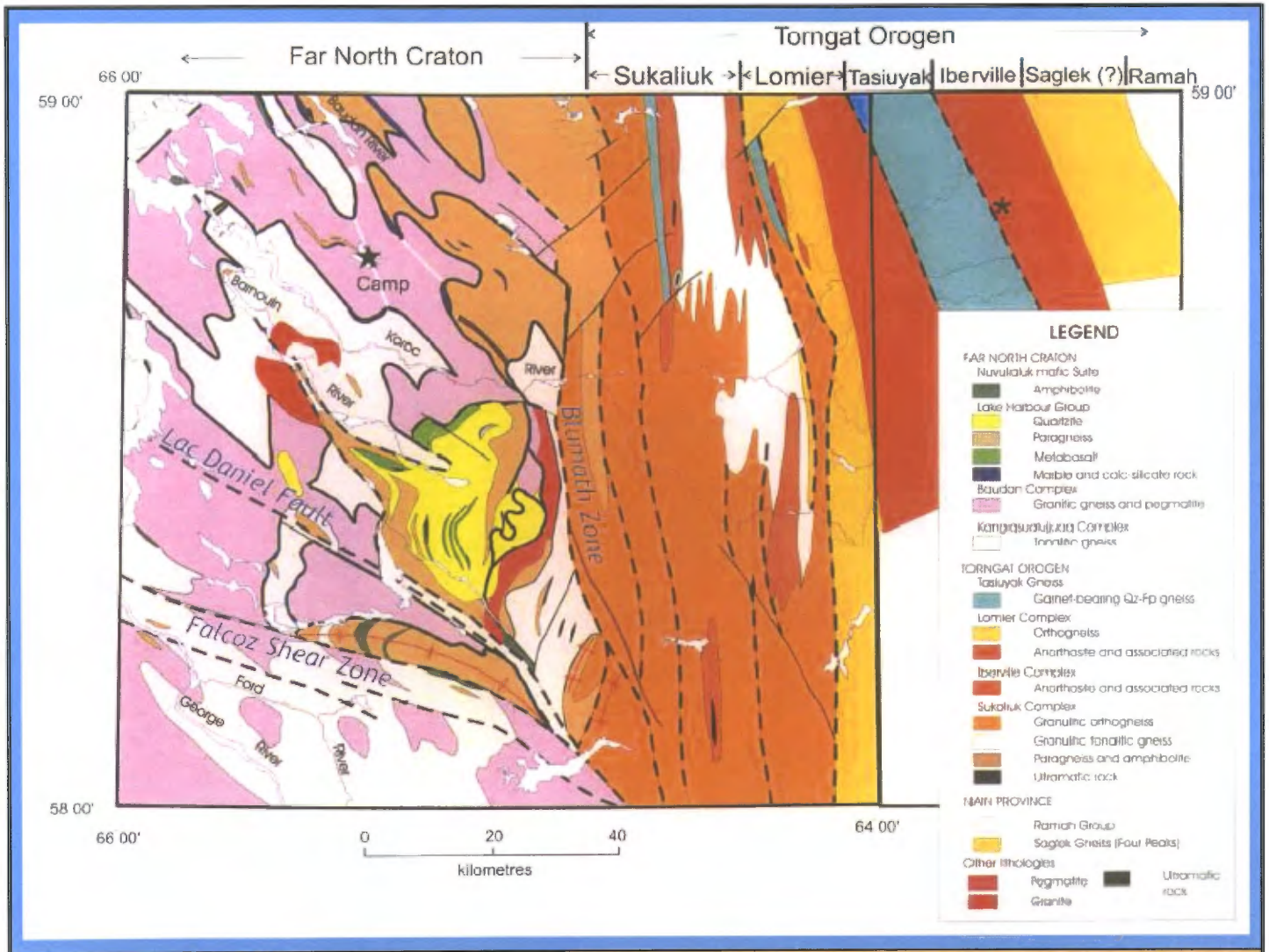


**Figure 3: Simplified geology of the Lac Daniel Project Area (map 241)**

# 3.0 PRESENTATION OF THE MAGNETIC METHOD

## 3.1 Fundamental

The magnetic method is one of the oldest geophysical methods in use today. The development of a fluxgate airborne system commenced in the thirties at the Gulf Research labs. Wartime saw intensified development of the unit for Magnetic Anomaly Detector use in submarine detection. The first aeromagnetic survey was flown in 1947, in northern Ontario, Canada by the company Gulf Co. This survey resulted in the discovery of the magnetite deposit in Boston Twp. Since this first discovery, the magnetic method contributed to the discovery of number of mines exploited around the world.

The main earth magnetic field could be compared to a magnetic magnet bar located at the earth centre and oriented in accordance with the magnetic pole axis (figure 4). This magnet generates a dipolar field, which act as an inductive field.

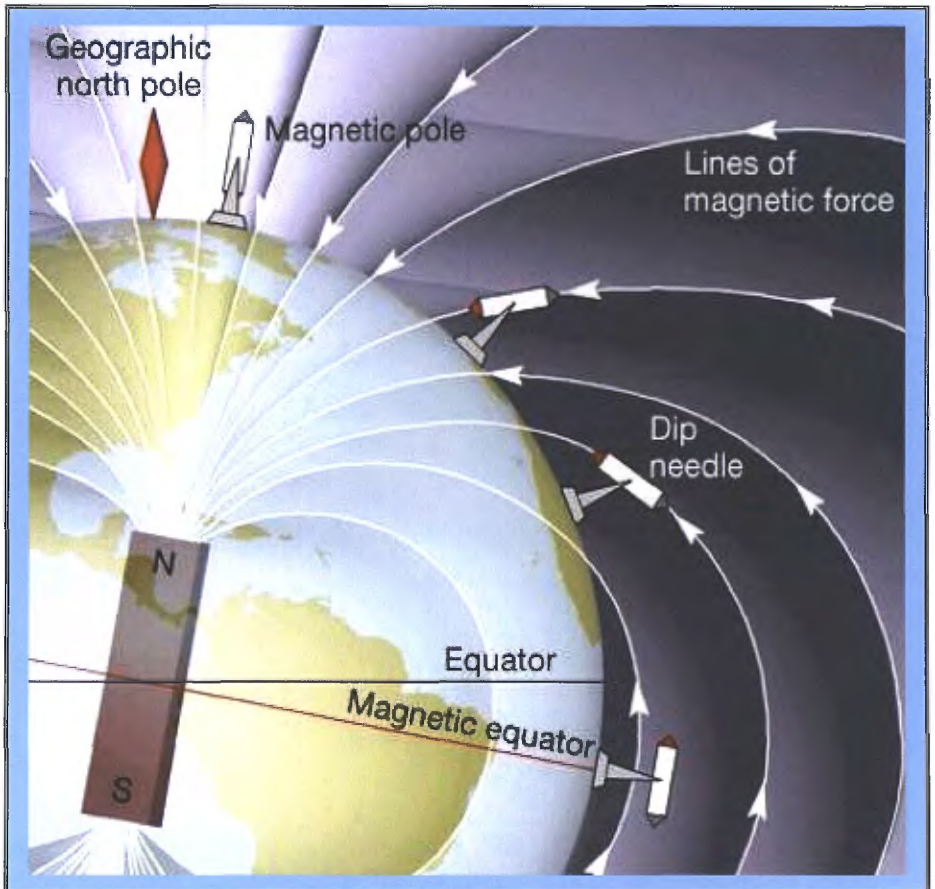


**Figure 4: The Earth Magnetic Field**

The earth field anomaly consists of that part of the field which is caused by irregularities in the distribution of magnetized material in the outer crust of the earth. The whole purpose of magnetic prospecting is to measure the anomaly field and to attempt to interpret the magnetic in-homogeneities indicated in terms of geologic detail relevant to the occurrence mining deposit or accumulation of petroleum.

Susceptibility is the fundamental rock parameter in magnetic prospecting. It is defined by the property of certain material to become magnetized in presence of a magnetic inductive field. The magnetic response of rocks and minerals is determined by the amounts and susceptibilities of magnetic materials in them.

Most minerals present null or very low magnetic susceptibilities, except magnetite (Fe3O4) and some other less abundant minerals (ilménite, hematite, pyrrhotite, franklinite, chromite, arsenopyrite, limonite, pyrite). Fortunately, magnetite is found in almost rocks in variable quantity and a fraction of 1% can be detected. Also, regionally, for the same geologic formation, magnetite grade tend to be approximately constant.

The raw field data collected in digital form during a magnetic survey are subsequently edited, corrected for diurnal, levelled, gridded and contoured. Observed variations on the corrected Total Field Magnetic map represent essentially the distribution of ferromagnetic minerals in the different geologic formations. At this stage, it is possible to make a qualitative (identification of geologic contacts, faults, folds) or quantitative data interpretation (calculation of depths, dips and other geometric parameters of isolated magnetic sources).

## 3.2 Enhancement of Magnetic Grids

From the corrected Total Field Magnetic grid, it is possible to calculate the First and Second Vertical Derivatives (1-VD and 2-VD), the Reduction to Pole (RTP) and the Analytic Signal maps. These filters are obtained by transforming the Total Field Magnetic grid into the frequency domain, applying a transform function, and then transforming it back into the spatial domain.

The First and Second Vertical Derivatives behave somewhat like high-pass filters. They accentuate subtle changes in the Total Magnetic Field Intensity map by suppressing long-wavelength regional components and reducing the effect of interference between adjacent anomalies. Contributions of magnetic components coming from deeper geological units are reduced and both surface cultural noise and intra-sedimentary anomalies are amplified. These maps are used in a qualitative manner to determine the location of source-body edges.

The RTP is a fundamental transformation required to interpret aeromagnetic data. The RTP operator converts Total Magnetic Field Intensity anomalies recorded in latitudes where the Earth's magnetic field is inclined to what they would be at the magnetic pole, where the field is vertical. This results in a more geometrically realistic portrayal of the data and generally facilitates a more precise interpretation of structures and contacts.

The Analytic Signal is obtained from both the horizontal and vertical derivatives of the Total Magnetic Field Intensity. Its amplitude is remarkable in that it allows one to obtain a signal that is independent of the source magnetization direction.

## 3.3 Qualitative Data Interpretation

Magnetic anomalies can be produced by a number of causative features such as lithology changes, variations in the thickness of magnetic units, faulting, folding, and topographic relief.

Generally, basic rocks contain more magnetite than acid rocks. Although there is no panacea to relate susceptibility to lithology, certain trends are evident. For example, sedimentary rocks have the lowest average susceptibility and basic igneous rocks have the highest; gabbros and ultrabasic rocks are generally more magnetic than granitic rocks. However, for a particular rock, the magnetic susceptibility is variable and it exist a wide overlap between different rock types. In every case, the susceptibility depends only on the amount of ferromagnetic minerals present, mainly magnetite, sometimes titano-magnetite or pyrrhotite.

For a particular body, the strike and dip of the body, and the inclination of the magnetic field, will change drastically the shape of the magnetic anomaly. The interpreter must have a mental image in order to relate magnetic anomalies to rock bodies. This observable fact incites the geophysicist to pole-reduce the data before beginning both qualitative and quantitative interpretation. Pole-reduced data are easier to interpret since the shape of anomalies can be more easily related to the underlying geology, the effect of overlapping anomalies is reduced and anomalies are centered over bodies with vertical sides.

Once pole reduced, the effect of the body dip can be easily illustrated because the anomaly is not much changed by strike. Figures 5 takes a particular body (the infinitely long thin sheet) and shows the anomaly shapes for different dips at magnetic inclination of $90^{\circ}$ (from Reford, 1964).

## 3.4 Quantitative Data Interpretation

### 3.4.1 Power Spectral Analysis

A grid of aeromagnetic data is a discrete representation of a continuous function. The frequency content of a data grid can be described in terms of spatial frequency in units of radian/sampling interval or as its wavenumber in units of cycles/sampling interval. From the fundamental sampling theorem (Hall, 1979), it can be shown that the highest resolvable wavenumber, called the Nyquist wavenumber, that can be expressed in a square grid is equal to one half of the grid spacing. The Nyquist wavenumber is important because any higher wavenumber in the measured field will be reflected, or aliased, back into the frequency spectrum as a lower wavenumber. The possible range of wavenumber on a grid is therefore from 0, for a non-oscillating or constant component, to 0.5 cycles/grid cell, the Nyquist wavenumber.

The grid of data can be transferred to the spatial frequency, or wavenumber domain, by the application of a 2-dimensional Fourier Transform to the data. All of the information in the original

grid is present in the transformed frequency domain grid but it is described in terms of its component frequencies instead of position. In practice the transform is done using faster algorithms called the fast Fourier Transform (FFT). The complex wavenumber spectrum F(u,v), which results from the application of a Fourier Transform, can be analyses more easily by calculating the energy spectrum:

$$E(u,v) = a^2 + b^2 \qquad (1)$$

where: a = real part of F(u,v) containing amplitude information
b = imaginary part of F(u,v) containing phase information

The energy spectrum E(u,v) shows the spectral energy distribution of the data in terms of its wavenumber composition.

The power spectrum of airborne magnetometer total field data can be used to determine average depth values of buried magnetic rocks located at different depths (Spector, 1967; Spector and Grant, 1970; Battacharya, 1966). These depths are established from the slopes of the log-power spectrum at the lower end of the total wavenumber, or spatial frequency band. The method is based on the assumption that the magnetic effect of the basement surface can be simulated by an uncorrelated distribution of blocks of varying depth, width, thickness, and magnetization. On the log-power spectrum plot, if a group of blocks has a similar depth, they will fall into a line of constant slope. Thus, if there are groups of blocks with the individual groups at widely different depths, such as shallow volcanic over a deep basement, the plot will be separable into parts with different slopes and the magnitude of the slope is a measure of depth.

The method has its application primarily to evaluation of general conditions over broad areas and to give relatively objective separation of the sharp and broad anomalies in such a way that multiple depth zones could be recognized. It is not applicable to determination of depths to individual anomalies, as used for mapping a basement surface, but gives an objective confirmation of the general depth of such a surface.

### 3.4.2 Euler Deconvolution Method

The Euler deconvolution method is based on Euler's homogeneous equation (Pilkington and al., 1991), which for data in map form is given by:

$$(x-x_o)\partial T/\partial x + (y-y_o)\,\partial T/\partial y + (z-z_o)\,\partial T/\partial z = N\,(B-T) \qquad (2)$$

where:

- $(x_o, y_o, z_o)$ is the position of a magnetic source whose total field effect T, is detected at (x, y, z)
- B is the regional field
- N is the degree of homogeneity or structural index (Thompson, 1982; Reid et al., 1990) which depends on source type
- $\partial T/\partial x$, $\partial T/\partial y$ and $\partial T/\partial z$ are two horizontal and one vertical gradients of the magnetic field which are easily calculated using frequency domain processing

If the total field T(x,y,z) has the general form of:

$$T(x,y,z) = G / r^N \qquad (3)$$

where:

- $r = (x^2 + y^2 + z^2)^{1/2}$
- $N = 1,2,3,...$
- G is not dependant on (x,y,z)

Then T satisfies Euler's equation.

Many simple magnetic sources types can be described in this way, with the value of the structural index, N, being indicative of the source geometry. From the equation (3), we see that N controls the rate of decay of the magnetic field with distance from the source. When N is large, the field falls off at a greater rate than for small N. Although the source geometry controls the value of N, the direction of the Earth's magnetic field also influences the rate of decay of the field, but we may consider this as a secondary effect. For a magnetic source such as a contact between two differently magnetized units, N is small.

Theoretically, since there are four unknowns in equation 3, the source location ($x_o$, $y_o$, $z_o$) and the background level B, we can use four observation points (where x, y, $\partial T/\partial x$, $\partial T/\partial y$, $\partial T/\partial z$ and T are known) and solve the resulting set of simultaneous equations. Since data are usually noisy and closely spaced anomalies can degrade the anomaly shape, it is common practice to use more than 4 points, usually 7, and solve a set of overdetermined equations using least-squares. A window of fixed length is moved along the profile at intervals equal to the data spacing and an estimate of the source location made for each window position. From the least-squares solution, an estimate of the error in the depth estimate can be made and used to reject solutions if their error is too great. As more solutions are rejected, the clustering of the depth estimates will improve and the clarity of individual structures is enhanced.

### 3.4.3 Depth Calculation, Peters's Technique

We assume a dipping dike with infinite longitudinal and depth extents and presenting the characteristics shown on figure below:

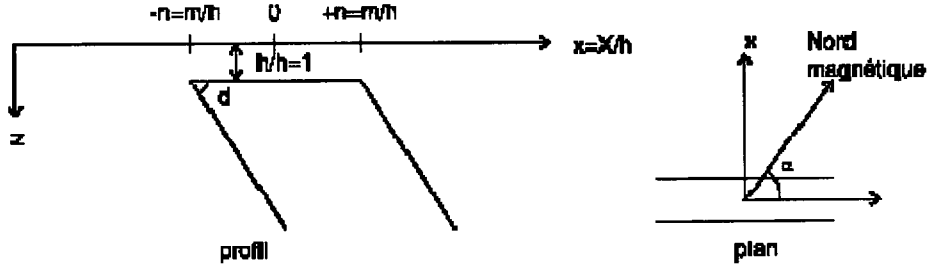

Where:

- m = dike half-width
- h = depth to the top of the dike
- *n = m/h*
- *x= X/h where X is distance relative to the dike centre*

This dike will produce a magnetic anomaly like the one presented below:

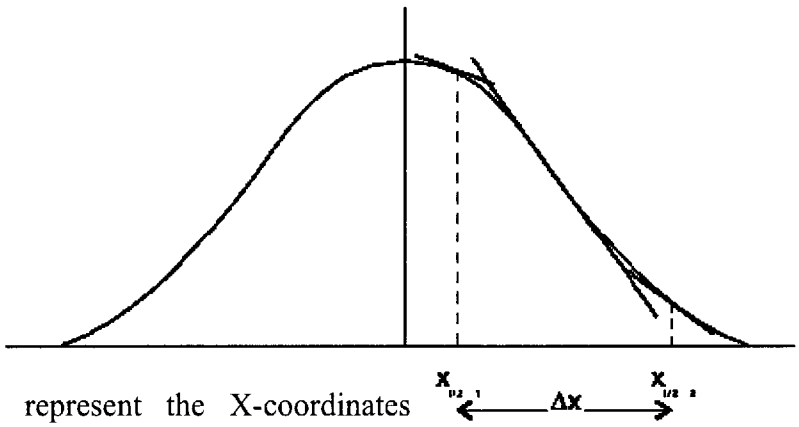


The $x_{i/2}$ points represent the X-coordinates where the slope of the curve is equal to half the maximum slope.

The maximum slope is obtained at the inflexion points, i.e. where the first derivative equal zero. It could be mathematically demonstrated (Peters, 1949) that the half-slope points are only a function of two geometric parameters: the dike half-width and the dike depth.

This function specifies that the dike depth can be obtained by the following expression:

$$\mathbf{h = (x_{½,1} - x_{½,2})/n} \qquad (4)$$

To estimate the parameter « n », we observe the shape of the anomaly curve:

- If the curve is acute and the inflexion points are located near the summit, **n = 1.2**
- If the curve is moderately acute and the inflexion points are located near the curve centre, **n = 1.6**

If the curve presents a clear flat summit, **n = 2.0**

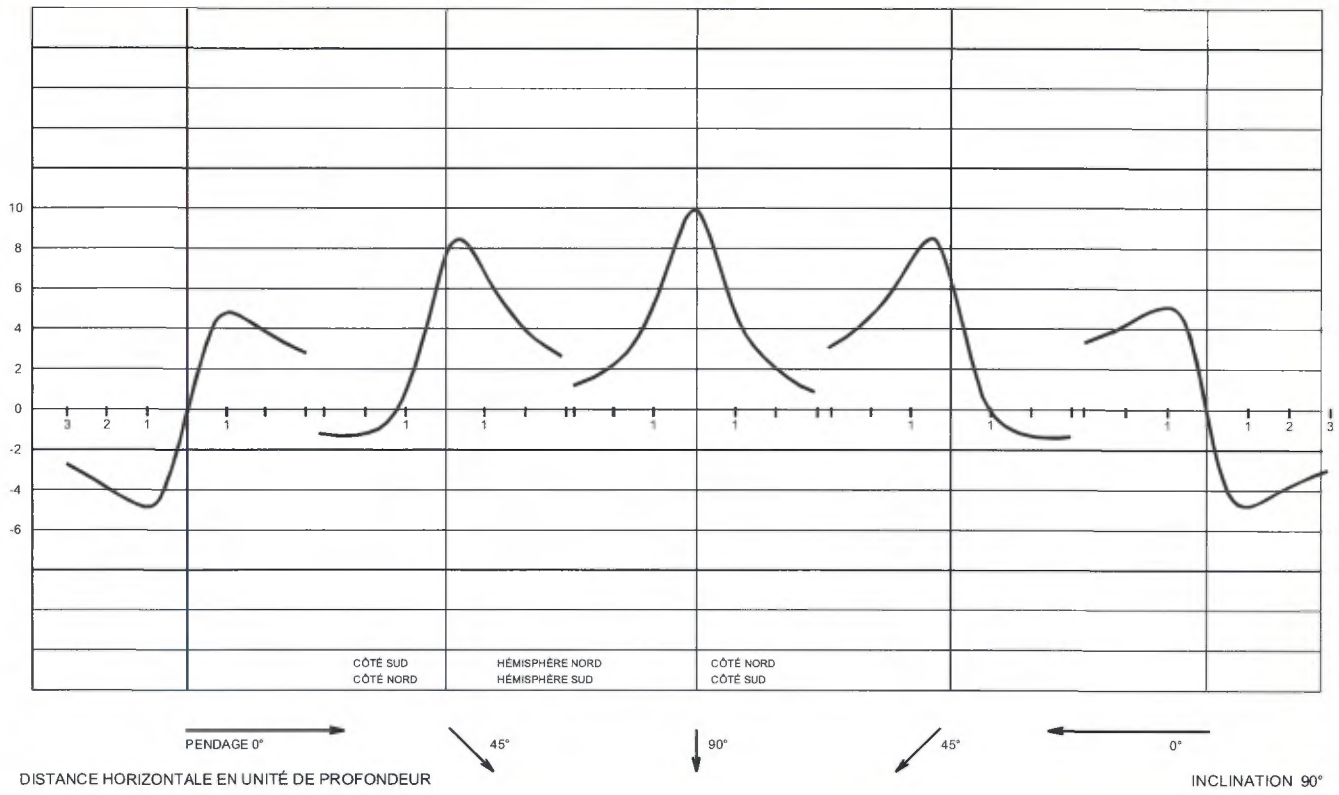


**Figure 5: Total Field Anomaly Shape (Field Inclination: 90°)**

# 4.0 PRESENTATION OF THE SPECTROMETRIC METHOD

*(Ref.: Mainly from IAEA 2003)*

## 4.1 Fundamental

Gamma ray spectrometry is widely used in geological mapping, soil surveying, mineral exploration, and regolith studies. The use of the method as a mapping tool requires an understanding of the geochemistry of the radio-elements in rocks and soils, and the processes that effect their distribution and mobility. Mineralogical and geochemical studies of rocks and soils play a fundamental role in corroborating the interpretation of gamma ray spectrometry surveys, as they provide insight in the mode of occurrence of the radio-elements and their petrogenetic or pedogenetic associations.

Gamma ray spectrometric mapping applications typically rely on an integrated approach. The gamma ray data are interpreted in combination with other airborne survey data such as magnetic and electromagnetic surveys, satellite images, and geological and soil maps.

Gamma-ray surveys are used to detect the abundance of potassium (K), thorium (Th) and uranium (U), which are the only naturally occurring radioisotopes with sufficient gamma-ray emission energies to be detected by scintillation counters at heights flown by aircrafts (Figure 6). The relative K abundance is measured directly using the decay of $^{40}K$, an unstable isotope of K that emits energies of 1.46eV. Relative U abundances are indirectly measured from the gamma-emitting daughter product of $^{214}Bi$, and for Th the gamma-emitting daughter product of $^{208}Tl$ (Grasty, 1975). Gamma ray emissions from surface and near-surface material can be measured for depths of up to about 30 cm for dry material with a density of $1.5 g/cm^3$. However, measured count rates decrease with increased distance between the source and the sensor, so will vary with changes in altitude of the aircraft (IAEA, 1991).

Gamma-ray surveys may be used to map the differences in rock type distribution, therefore enabling the production of geologic and structural maps. The gamma-ray spectral characteristics vary according to individual rock type, or geomorphological type. Where a certain geological unit is present across different groups some of their K, U and Th characteristics will be similar.

**Potassium**

Potassium is a volatile lithophile element and is monovalent under natural conditions. The abundance of potassium in the Earth's upper crust is 2.33 wt. % K. Most K occurs as alkalifeldspar and micas in felsic rocks, mainly granitoids, which contain 3.5 wt. % K on average. Mafic and ultramafic rocks contain much lower concentrations, with average K content ranging from 0.58 to 0.75 wt. %. The feldspar mineral series, the feldspathoids leucite and nepheline, and the micas biotite and muscovite, together contain virtually all the potassium in metamorphic and magmatic rocks. Some amphiboles contain up to 1 wt. % K.

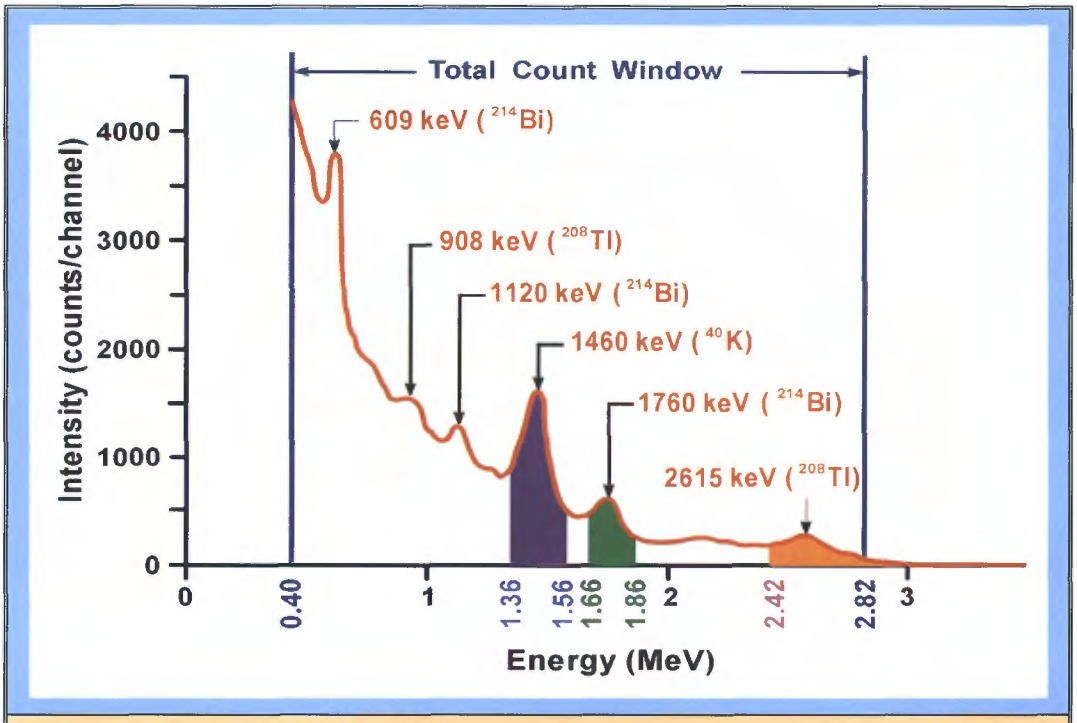


**Figure 6: A Typical Gamma-Ray Spectrum**

| Table 3: Windows Used in Spectrometric Surveys | | | |
|---|---|---|---|
| **Radioelement** | Daughter Element | Central Pick (KeV) | Window |
| **K** | $K^{40}$ | 1460 | 1360-1560 |
| **U** | $Bi^{214}$ | 1760 | 1660-1860 |
| **Th** | $Tl^{208}$ | 2615 | 2410-2610 |
| **Total Count** | | | 400-2820 |

**Thorium**

Thorium is an actinide element with a valence state of $Th^{4+}$ in solution with evidence for lower valence states in solid state. It forms with the anions fluoride, oxalate, iodate and phosphate insoluble precipitate. Th can be dissolved in acid solutions and its solubility is enhanced by humic acids. The abundance of Th in the Earth's crust is low, typically in the range of ppb to ppm with an average of about 12 ppm. Th is a constituent of the accessory minerals zircon, monazite, allanite and xenotime, apatite and sphene. Th is the parent of a decay series of which the highest energetic gamma rays (2.62 MeV) are emitted by the daughter isotope $^{208}Tl$. In general, about 60 years is required to establish radioactive equilibrium in the Th series, and gamma ray activity is thus a good measure of Th concentration. Chemical fractionation among the members of the U and Th series occurs during magmatic processes. This results in radioactive disequilibrium between $^{238}U$ and $^{230}Th$, and $^{230}Th$ and $^{226}Ra$ in the $^{238}U$ decay series in volcanic rocks.

**Uranium**

Uranium is a reactive metal with an average abundance of about 3 ppm in the Earth's crust. U appears in the valence state $U^{4+}$ in igneous rocks with crystallochemical properties close to $Th^{4+}$ and the Light Rare Earth Elements (LREE), which explains the coherent geochemistry of U, Th and LREE in igneous rocks. This coherence is lost in hydrothermal and supergene conditions, where uranium is partially or totally oxidized to $U^{6+}$, which forms soluble complexes with the anions: $CO_3^{2-}$, $SO_4^{2-}$ and $PO^{3-}$.

Uraninite is common as minute inclusions in the rock forming minerals in granites or as large grains in mineralized granites and pegmatites. Uraninite also occurs in hydrothermal veins and sedimentary rocks. The accessory minerals zircon, monazite, apatite, allanite and sphene are common in igneous and metamorphic rocks, of which zircon and monazite are the most resistant to weathering. As U becomes mobile under supergene conditions, a large variety of $U^{6+}$ minerals may form. This explains the variety of minerals found in uranium deposits, including silicates, phosphates, carbonates, sulphates, vanadates, molybdates, niobates, tantalates and titanates.

## 4.2 Distribution of the radio-elements in rocks and soils

The radioelement concentrations show an increase in average radioelement concentration with an increase of $SiO_2$. For thorium and uranium this is due to the high charge and radius of the $Th^{4+}$ and $U^{4+}$ ions, which excludes them in the substitutions of major ions in the crystallization of early rock forming minerals. They are therefore accommodated in accessory minerals, such as zircon, allanite and monazite. Potassium is also highly incompatible during crystallization of magma. The tendency for the radio-element concentrations to increase with increasing Si content in igneous rocks breaks down at high concentrations of Si (> 70 wt. % $SiO_2$), particularly for U.

## 4.3 Geological Mapping

Gamma ray spectrometric data have been applied with variable degrees of success to the mapping of lithological units. The degree to which bedrock units can be delineated depends on many factors. The most important factors are:

1. the contrasts in radio-element content between lithological assemblages;
2. the extent of bedrock exposure and soil cover;
3. the relative distribution of transported and in-situ soils;
4. the nature and type of weathering;
5. the soil moisture content; and
6. the vegetation cover.

Unlike U, the average K and Th content of soils reflect the average K and Th content of the rocks from which they are derived. But the differences in soil radio-element concentrations are relatively small. In general, a useful strategy for geological mapping is to first outline the major lithological units and then enhance the radio-element patterns within the individual units.

Enhanced products of gamma ray spectrometry data have often assisted in detailed mapping or further subdivision of lithological units. In some cases units with distinct radioelement signatures (mostly volcanic in origin) were identified that could be used as lithological markers in unravelling the geological map pattern in complex areas. Integrated interpretation with aerial photograph, satellite imagery and other airborne geophysical data sets allows exploiting the complementary geological information and enables the radioelement distributions to be studied in a structural geologic and geomorphologic context.

Gamma ray spectrometric data have shown to be uniquely applicable for mapping subtle compositional variations within igneous suites, particularly granitoid plutons and batholiths. Zonation patterns in granites have been commonly recognized in gamma ray spectrometry surveys, many of which were not recognized by conventional field mapping. This is because the bulk of the radio-elements in igneous rocks occur within accessory minerals, such as monazite, xenotime, zircon, allanite, sphene and apatite. Subtle (but diagnostic) variations in the concentrations of these accessory phases are difficult to recognize in bedrock exposures. Also, late-stage magmatic and hydrothermal processes may control regional radioelement distributions in granitoids, particularly U.

Normal zoning in granitoid plutons formed by fractional crystallization, show a gradual increase in K and Th (and Th/U) from the margin to the centre. Along this path the $SiO_2$ content gradually increases and the mafic index decreases with the lithological composition ranging from quartz diorite through granodiorite to granite.

## 4.4 Direct Detection of Mineralization

The most direct application of gamma ray spectrometry surveys is the search for U and Th deposits. U and Th anomalies may be identified on profile and grid presentations of the data. Ratioing and statistical image processing techniques can enhance subtle anomalies. Anomalies can be followed up on the ground using portable gamma ray spectrometers. The character of radiometric anomalies associated with subsurface and outcropping U mineralization depends on the forms of U mineralization, the host rock, and the geological setting. Typical features of U mineralization detected at the earth's surface are:

1. elliptical dispersion halos with dimensions from 70 × 80 m up to 80 × 350 m;
2. anomalous U concentrations in the range 4-20 ppm eU;
3. associated Th anomalies in the range 5-40 ppm eTh;
4. ratios between the radioelement of Th/U<1, U/K>5-10, Th/K in the range 4-5; and
5. increasing gamma radiation with depth.

Due to relatively low penetration of gamma rays through rock and soil, the probability of discovery of uranium mineralization is dependent on the U concentration in the source, its surface dimensions, and the positions of the measured profiles. A small outcrop of high-grade U mineralization is a more difficult target for U exploration than low-grade mineralization with extensive surface outcrop.

The effects of hydrothermal processes, alteration and weathering on radio-element distribution do not only have implications for the direct detection of U and Th from gamma ray spectrometry surveys, but also for detecting a number of metal deposits. These include granophile deposits of Sn, W and Mo, porphyry Cu-Au mineralization, gold mineralization and stratabound polymetallic mineralization. The relationships between radioelement distribution and each of these deposit types are varied and complex. A thorough understanding of the effects of silicification, K-alteration, weathering processes and local lithological variations is required to evaluate the mineralization potential associated with radioelement anomalies.

The detection of K-alteration by gamma ray spectrometry surveys has received particular attention, as it has resulted in several mineral discoveries. K alteration halos can be repeatedly distinguished from normal K variations by their characteristic low Th/K ratios. The following example shows the importance of K alteration.

A high-resolution magnetic/radiometric survey, undertaken by the Geological Survey of Canada in 1994, delineated a large hydrothermal system in the Lou Lake area, Northwest Territories, Canada. The hydrothermal system is characterized by enrichment of potassium and magnetite within a volcano-plutonic magmatic zone. The potassium enrichment was evident as a potassium high, and confirmed by a low in the ratio of Th/K (i.e. preferential enrichment of potassium relative to thorium). The magnetite enrichment produced a significant magnetic anomaly. The Sue-Dianne polymetallic (Au-Co-Cu-Bi-W-As) deposit is located 20 km north of this hydrothermal system. It was originally discovered by exploring for the source of a uranium and U/Th ratio anomaly measured during a regional survey in 1974. A uranium halo around the

edges of the hydrothermal system (high values in the ratio of U/Th) correlated with several veins of pitchblende. The geophysical responses to the alteration and uranium mineralization were clearly seen in profile form (The hydrothermal system is evident in the high potassium and magnetic responses, and the coincident low in Th/K. The high responses in U/Th reflect uranium mineralization). Mapping the alteration system leads directly to the polymetallic deposits (Increasing potassium within a lithologic unit reflects the hydrothermal potassium enrichment). Ground truth studies showed that the effects of hydrothermal potassium enrichment within each lithologic unit were easily measured using gamma ray spectrometry.

More than thirty Canadian examples of geological mapping and mineral deposit characterization are provided in Shives et al. (1995), using airborne gamma ray spectrometry and systematic ground truthing. The deposit types covered include:

1. volcanic-hosted massive sulphides with associated potassium enrichment;
2. volcanic-hosted epithermal base and precious metals with associated potassium enrichment;
3. granite-hosted gold associated with illite alteration (potassium enrichment);
4. metavolcanic/metasediment-hosted gold with hydrothermal alteration (potassium enrichment);
5. metasediment-hosted skarn mineralization (Au-U-W-Mo-Co);
6. porphyry-hosted gold-uranium and copper–gold (molybdenum) with hydrothermal alteration (potassium enrichment);
7. metasediment-hosted polymetallic (Bi-Cu-Co-Au-As) with hydrothermal alteration (potassium enrichment);
8. carbonatite-hosted rare earth elements;
9. syenite-hosted rare metal/rare earth elements associated uranium enrichment;
10. dolomite-hosted epigenetic uranium-copper;
11. limestone-hosted uranium;
12. uraniferous pegmatites; and
13. metasediment-hosted pitchblende.

The Ashanti Belt in Ghana is a prolific producer of gold, and a high-resolution magnetic/radiometric survey has been flown over the area. The mineralization is hosted in two settings: Birimian metavolcanics and Tarkwaian conglomerate. The Birimian deposits are associated with sericite alteration, with a potassium enrichment signature. The Tarkwaian conglomerate can be mapped through its association with a potassium-rich phyllite marker horizon.

The physical properties of diamondiferous kimberlite sills in the Guaniamo area of Venezuela were studied and compared to neighbouring igneous rocks, which include granite, gabbro and volcanics. The magnetic susceptibilities range widely and there is a significant overlap between rock types. The degree and depth of weathering makes geological mapping difficult and minimizes the effectiveness of electromagnetic surveys. Measurement of the radioelement concentrations from fresh rock samples and drill core clearly showed that the kimberlite could be distinguished from most other igneous rocks (altered and foliated granites, granodiorites, gabbros, rhyolites, lamprophyre dykes, altered mafic dykes) and metasediments through

anomalously high levels of K, U and Th. The unaltered granites show similar levels of these radio-elements, but the kimberlite is differentiated through higher Th/K and lower U/K ratios.

Gold mineralization within the La Libertad region, Nicaragua, is dispersed in epithermal quartz veins within Tertiary basaltic lavas. There are five alteration zones (I-V) characterized by secondary mineral assemblages. A regional, 30 km long, portable gamma ray spectrometer profile of the region showed an increase in K concentration and of the Th/K and KU/Th ratios toward the Au mineralized veins.

An airborne gamma ray spectrometry potassium anomaly (5% K in a background level of 1.5-2%) with an associated Th/K ratio anomaly (Th/K=1 in a 4-6 background level) led to the discovery of Zn-sulphidic mineralization in a belt of Devonian and Lower Carboniferous volcanites and sediments in Northern Moravia, Czech Republic. The distribution of natural radio-nuclides in an alteration zone was used to site drill holes that intersected the Zn mineralization.

A study of radiometric data over the Mount Isa Inlier, Australia was presented in 1997. The area is host to more than eighty base and precious metal deposits. Over 700,000 line-km of airborne gamma ray spectrometric data were acquired in the province. The data provided critical contributions to mapping both lithology and regolith. GIS techniques were used to localize zones of radioelement enrichment or depletion, and correlated well with various types of base and precious metal deposits. The radiometric signatures in these areas were used to explore for similar deposits in the region.

## 4.5 Enhancement of Gamma-Ray Spectrometric grids

There are few enhancements which may be successfully applied to airborne Gamma-Ray Spectrometric grids. Usually, only simple division of one radiometric grid value by another (ratio) and false sun illumination are used. Ratios of the relevant radio-elements help to determine relative radio-element abundance which may be indicative of particular forms of mineralization. Ratio-ed grids can enhance the evidence of subtle changes between two gamma-ray responses that occur due to variations in the mineral chemistry of the host rock that may not be evident in single images. They may also serve to reduce variations in count rates due to effects such as variable soil moisture content and distance from source. Ratios are constructed by dividing the response in one band by that in another, e.g. K/ Th. Ratio results are usually shown as plain pseudo-colour images.

# 5.0 SURVEY DATA INTERPRETATION

For each block, the following maps were obtained from the Residual Magnetic Total Field Intensity data set:

- First Vertical Derivative (1-VD)
- Reduction to the Pole (RTP)
- Analytic Signal

On the other hand, the U/Th, U/K and Th/K ratios were calculated from the U, Th and K radio-element maps.

All these maps, with the Total Count map, were then used during the interpretation phase to create a final interpretation map, which integrate all the useful information.

## 5.1 Block ABE

### 5.1.1 Magnetic Data

The Total Magnetic Intensity Reduced to Pole map, the First Vertical Derivative map and the Analytic Signal map are presented on figure 7, 8 and 9. The Interpretation map is presented on figure 17.

The magnetic survey allowed mapping two fault networks striking approximately North-West and North-South. The Lac Daniel fault, oriented North-West, cross the ABE block from end to end.

Two magnetic highs were also mapped. These highs, noted as M1 and M2 on the Interpretation Map, are located in the centre part of the block and both are very close to a North-South oriented fault. These magnetic highs should correspond to small intrusive mafic bodies.

One magnetic profile was digitalized over each of these magnetic highs (profiles A and B on figure 7). Figure 18 shows the resulting profiles where many anomalous picks are observed. Peters's technique was then applied to obtain depths of each magnetic body. An average of 150 metres was obtained on each profile. Using figure 5, it is clear that the anomaly shapes indicate that the dip of each body is approximately vertical.

A geologic fold, located in the centre-west part of the ABE block, was clearly mapped. The fold is crossed by three major faults oriented approximately North-South.

Finally, many linear magnetic anomalies are observed almost everywhere over the block. All these elongated magnetic highs could represent significant dikes of pegmatite. We will see, in the next section, that some of them are located close or in relation with spectrometric anomalies.

### 5.1.2 Spectrometric Data

The following maps were used for the interpretation of gamma-ray spectrometric data acquired on block ABE:

- Total Count: figure 10
- %K: figure 11
- eqU: figure 12
- eqTh: figure 13
- eqU/eqTh: figure 14
- eqU/%K: figure 15
- eqTh/%K: figure 16

All the gamma-ray spectrometric interpretation results were added to the magnetic data interpretation results of figure 17.

Significant uranium anomaly areas are observed on figure 12. However, the U/Th ratio map shows that only a limited number should be retained: anomalies noted as R1 to R7 on figure 17. All these anomalies, located in the centre-west part of the block, are characterized by a preferential enrichment of uranium relative to thorium. The maximum values of the U/Th ratios over these anomalies are approximately 3 times the background level.

On the other hand, the U/K and Th/K ratios maps do not show evidence of potassium enrichment over these anomalies. This result could indicate that there is no real or limited hydrothermal alteration associated with these uranium highs.

Table 4 presents, by order of priority, a description of each anomalous area with proposed UTM co-ordinates (NAD27, zone 20N) for a ground follow up.

**Table 4: Block AEM, Gamma-Ray Spectrometric Anomalous Targets**

| Anomaly | Proposed Co-ordinates | | Comments |
|---|---|---|---|
| | X (m) | Y (m) | |
| **R1** | 348 205 | 6 486 695 | Located near a geological contact, a N-S fault and a magnetic high. Good U/Th ratio. |
| **R7** | 348 650 | 6 468 130 | Seems to be related to the fold. Good U/Th ratio. |
| **R5** | 351 865 | 6 475 355 | Located along the Lac Daniel fault and crossed by a N-S fault. |
| **R4** | 348 725<br>348 082 | 6 475 530<br>6 476 797 | Long elongated anomaly with good U/Th ratio. |
| **R2** | 345 070 | 6 482 405 | Very large anomaly. Could be related to a granitic massif. |
| **R6** | 349 030 | 6 470 340 | Good U/Th ratio located along a N-N-W fault. |
| **R3** | 345 625 | 6 478 015 | Good U/Th ratio related to a magnetic high. |

In addition to the selected targets of table 4, many long linear U/Th anomalies were mapped. These anomalies are located in 5 different zones noted as D1 to D5 on the interpretation map. In each zone, one or more linear anomalies could be present. All these linear anomalies should be related to either faulted zones or dike of pegmatite.

Table 5 presents a description of each anomalous area with proposed UTM co-ordinates (NAD27, zone 20N) for a ground follow up. Note that due to their lower U/Th ratios (compared to the targets of table 4), each of these linear anomalies should be considered as second priority targets.

**Table 5: Block AEM, Gamma-Ray Spectrometric Linear Anomalies**

| Anomaly | Proposed Co-ordinates | | Comments |
|---|---|---|---|
| | X (m) | Y (m) | |
| **D1** | 339 200<br>340 510 | 6 481 660<br>6 483 125 | 3 short linear anomalies with a fourth one located along the Lac Daniel Fault. |
| **D2** | 359 670 | 6 481 845 | 2 linear anomalies with poor U/Th ratios. |
| **D3** | 365 035 | 6 466 305 | A single linear anomaly with a medium U/Th ratio. |
| **D4** | 370 090<br>371 575 | 6 465 825<br>6 464 620 | 3 short linear anomalies along a geological contact. |
| **D5** | 377 725<br>371 205 | 6 468 690<br>6 459 175 | Many linear anomalies located near a geological contact, a fault and over a magnetic high. |

### 5.1.3 Conclusions

On the ABE block, the magnetic survey allowed to map:

- Two fault networks striking approximately North-West and North-South
- Two magnetic highs. These magnetic highs should be related to small intrusive mafic bodies at depth.
- A geologic fold, located in the centre-west part of the block.
- Many linear magnetic anomalies observed almost everywhere over the block

On the other hand, the gamma-ray spectrometric survey allowed mapping seven first priority targets and 5 second priority targets.

Ground follow up is recommended, as a first step, on each target (localization with a portable spectrometer, rock sampling if possible and, if needed, rock stripping or drill hole).

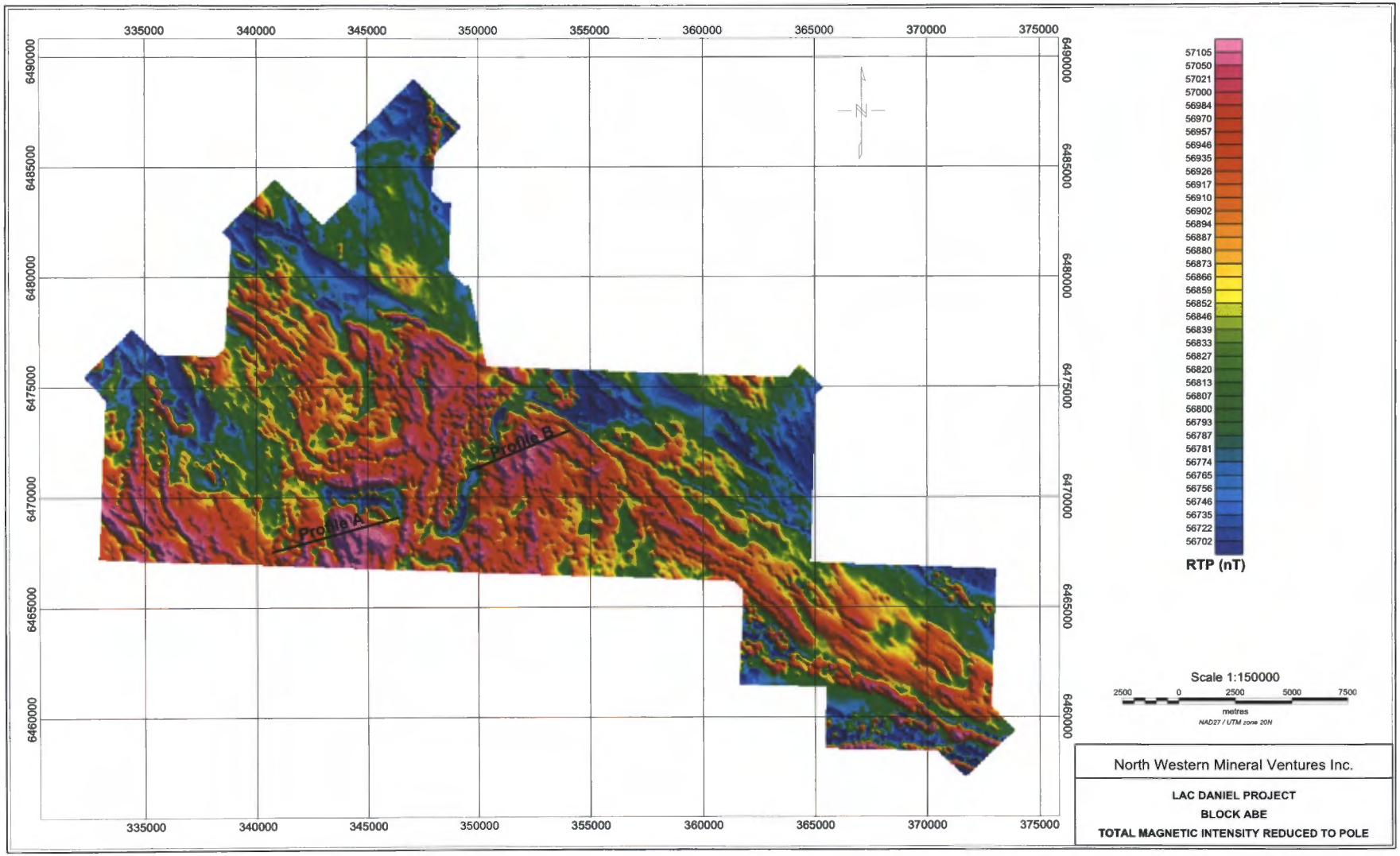


**Figure 7: Total Magnetic Intensity Reduced to Pole(Bloc ABE)**

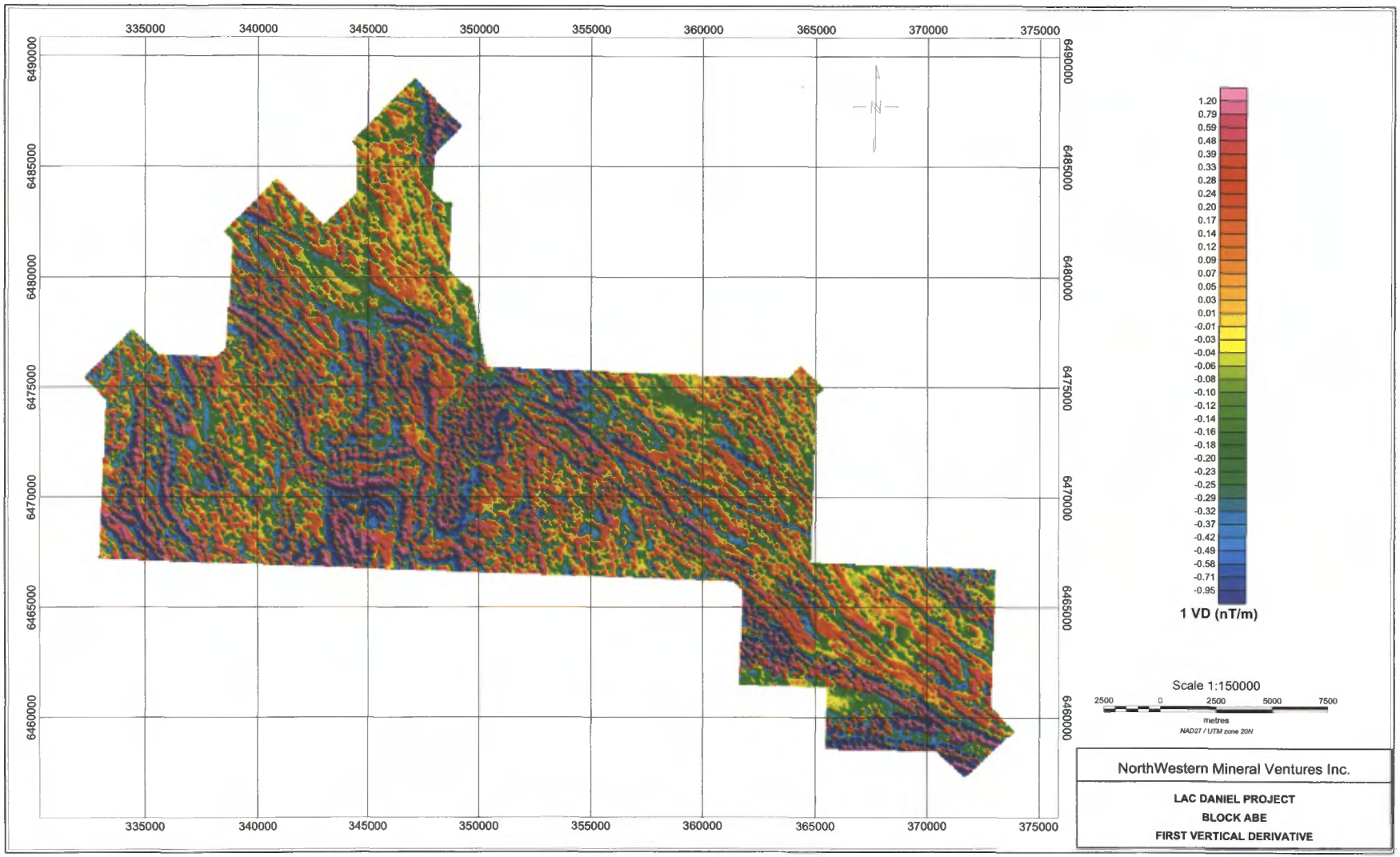


**Figure 8: First Vertical Derivative (Block ABE)**

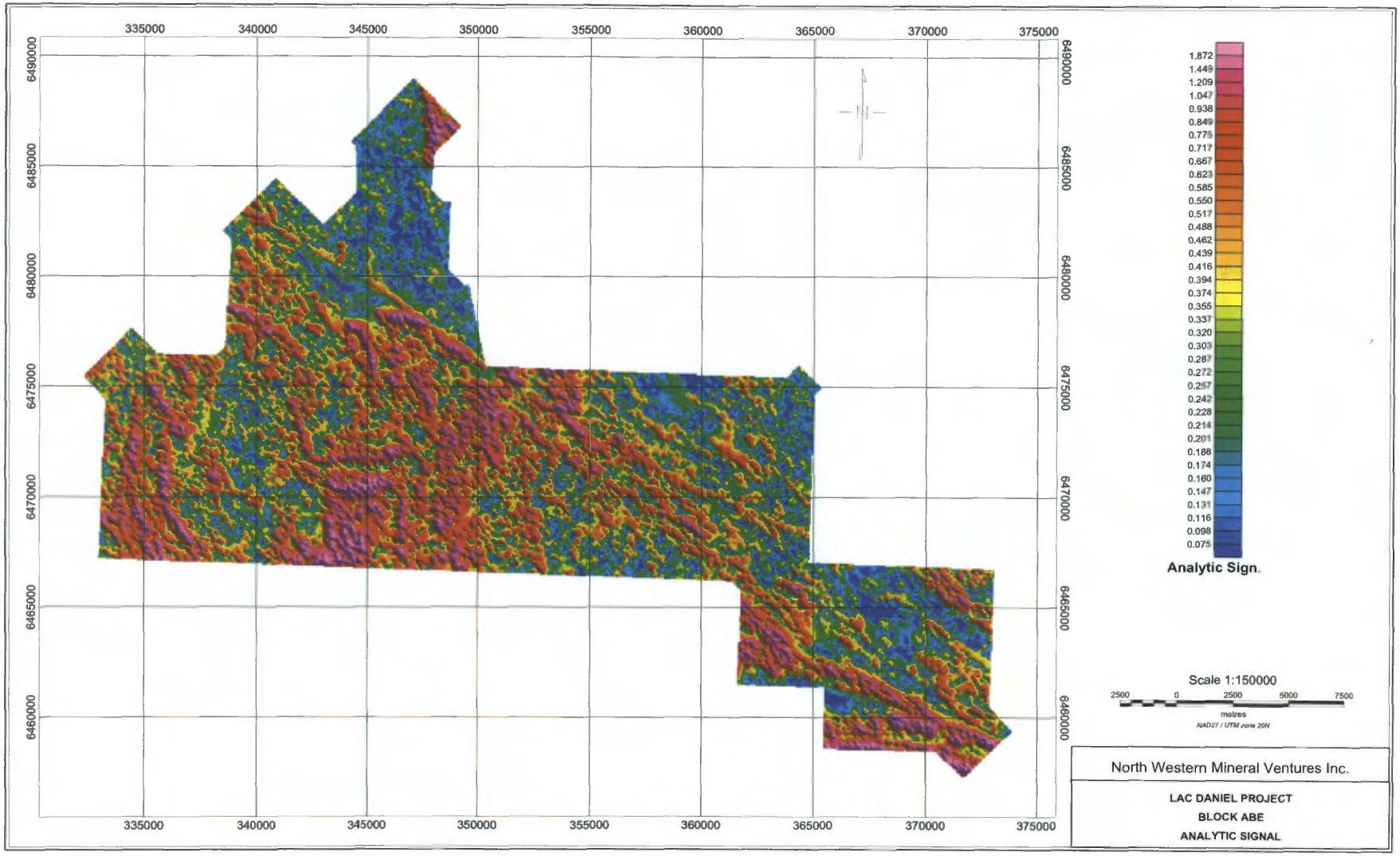


**Figure 9: Analytic Signal (Block ABE)**

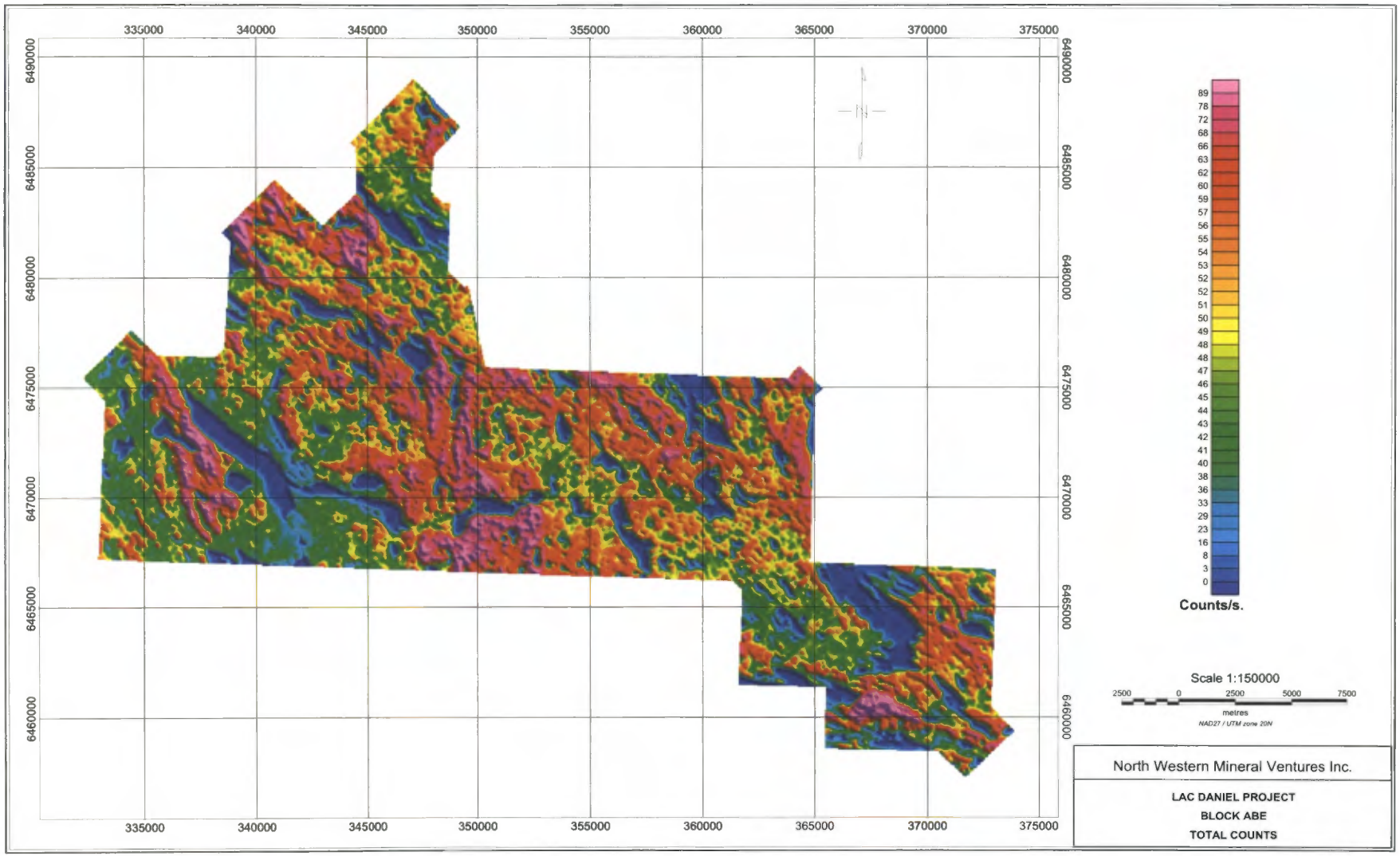


**Figure 10: Total Counts (Block ABE)**

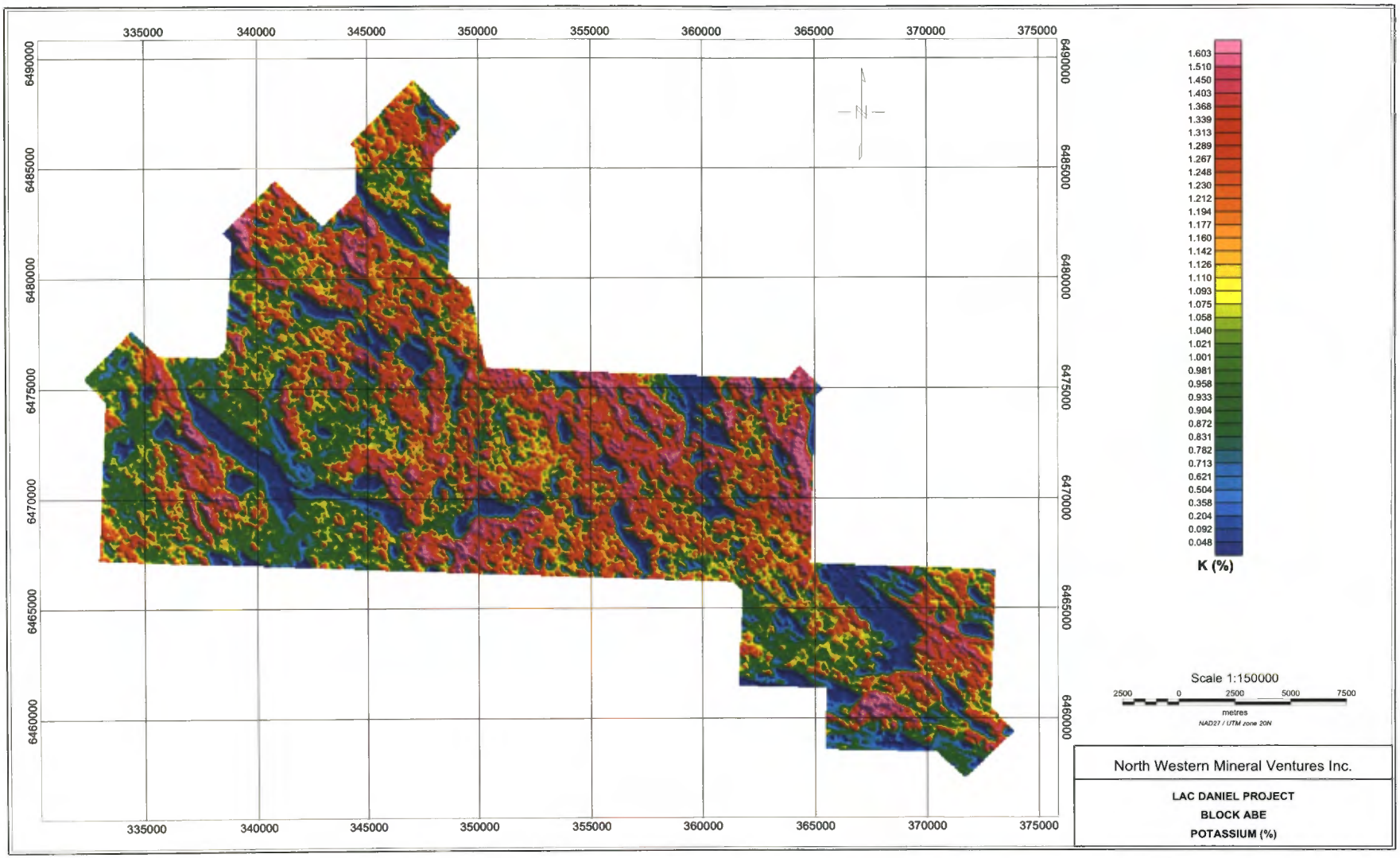


**Figure 11: Potassium (%) (Block ABE)**

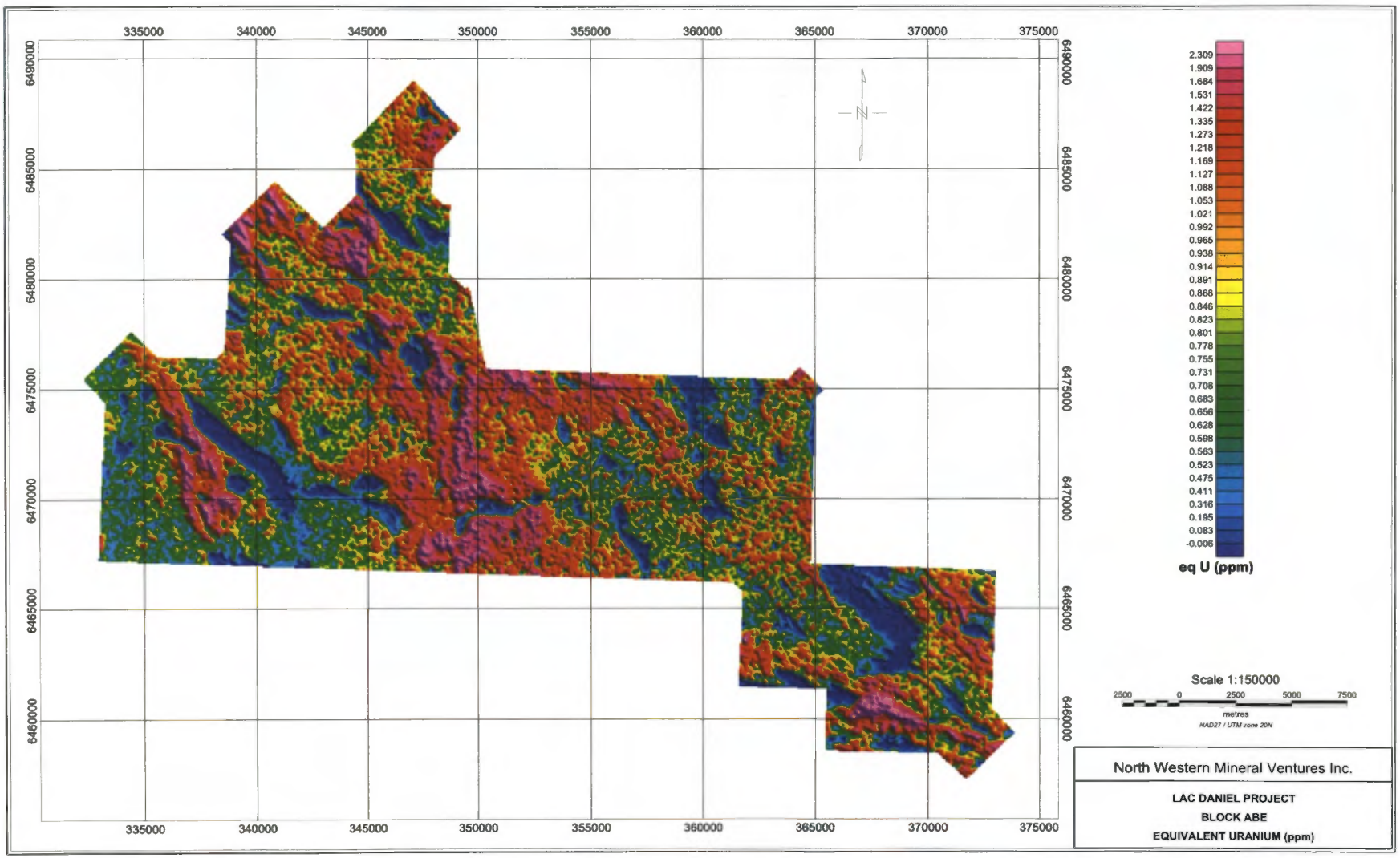


**Figure 12: Equivalent Uranium (ppm) (Block ABE)**

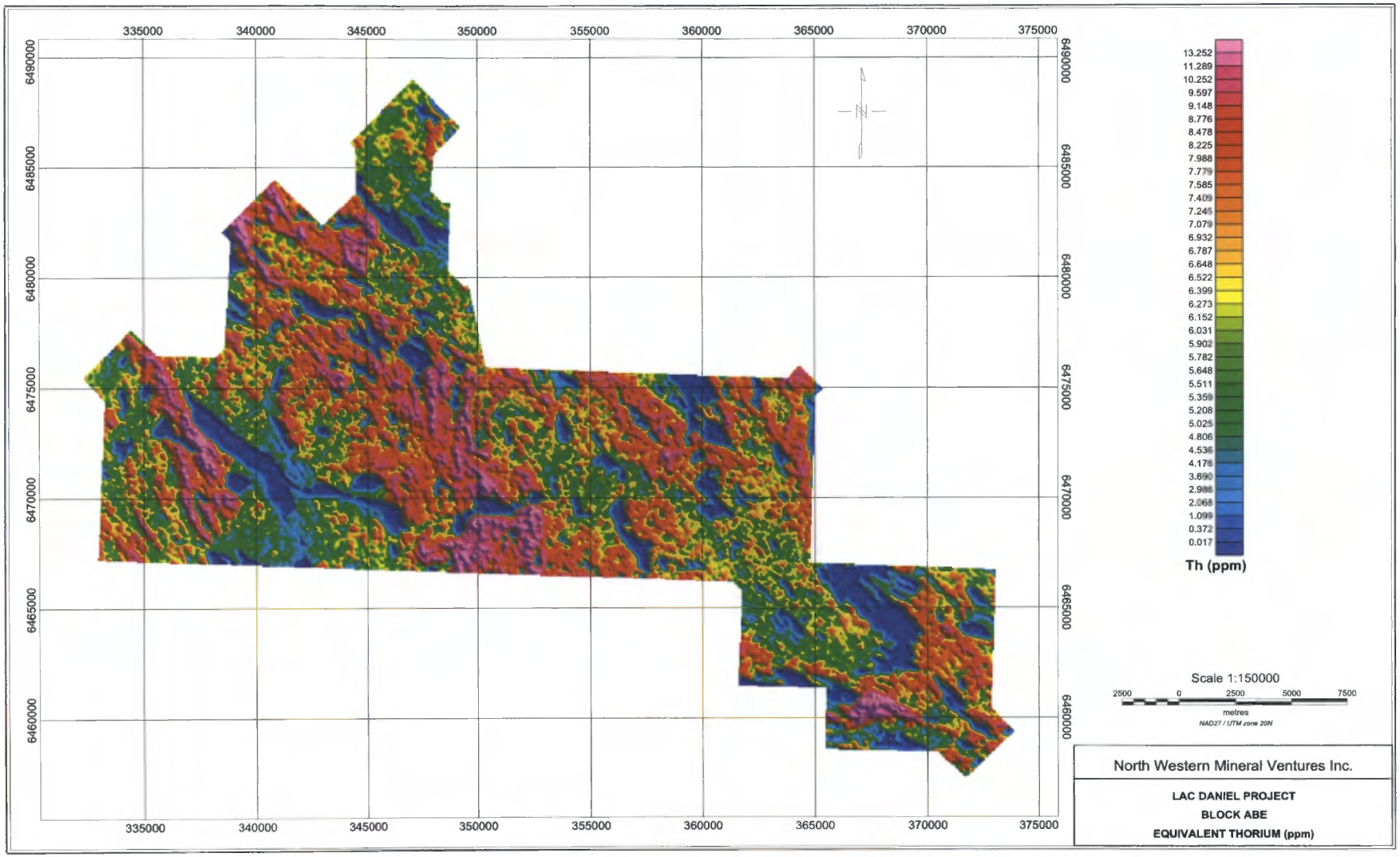


**Figure 13: Equivalent Thorium (ppm) (Block ABE)**

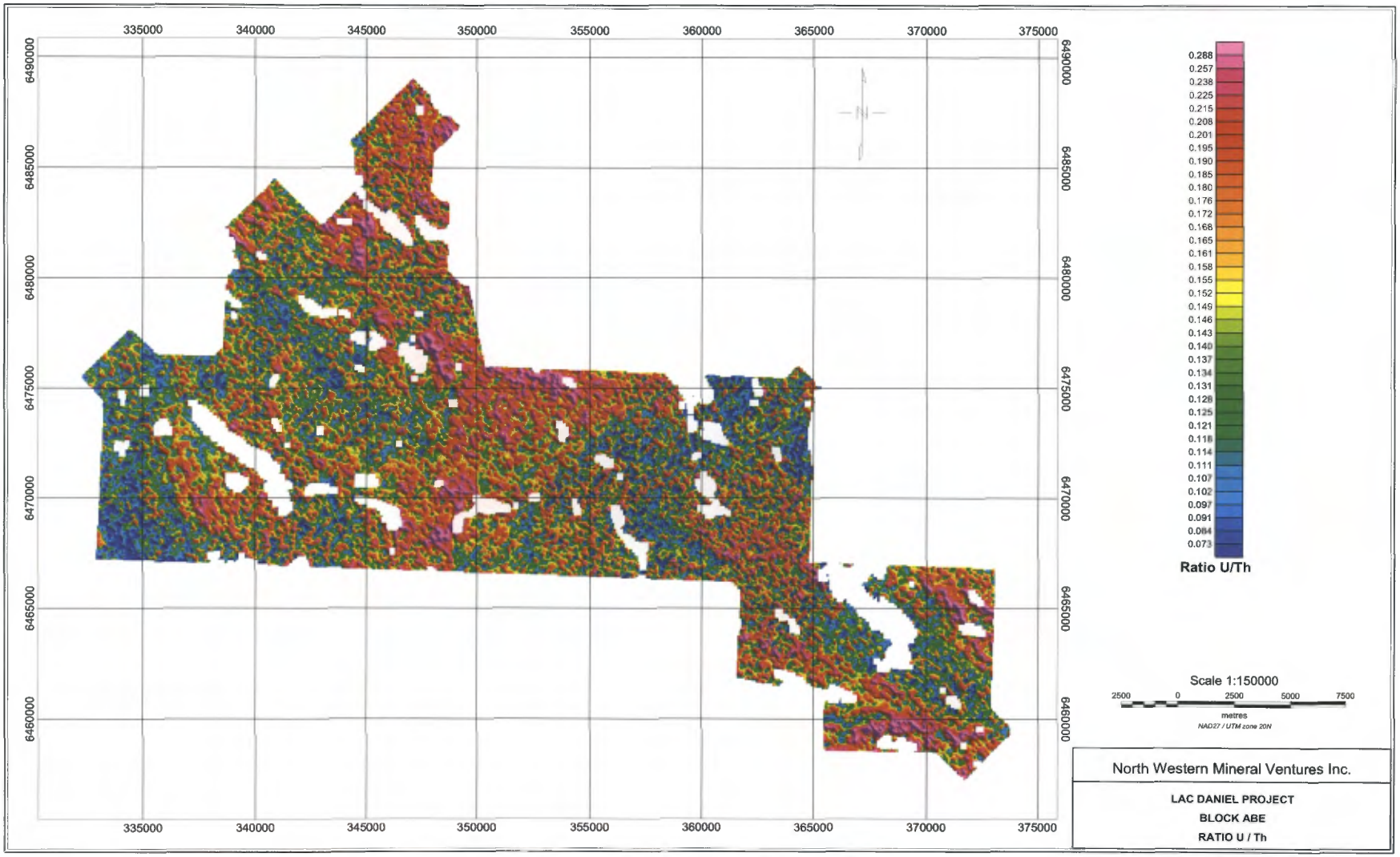


**Figure 14: Ratio U/Th (Block ABE)**

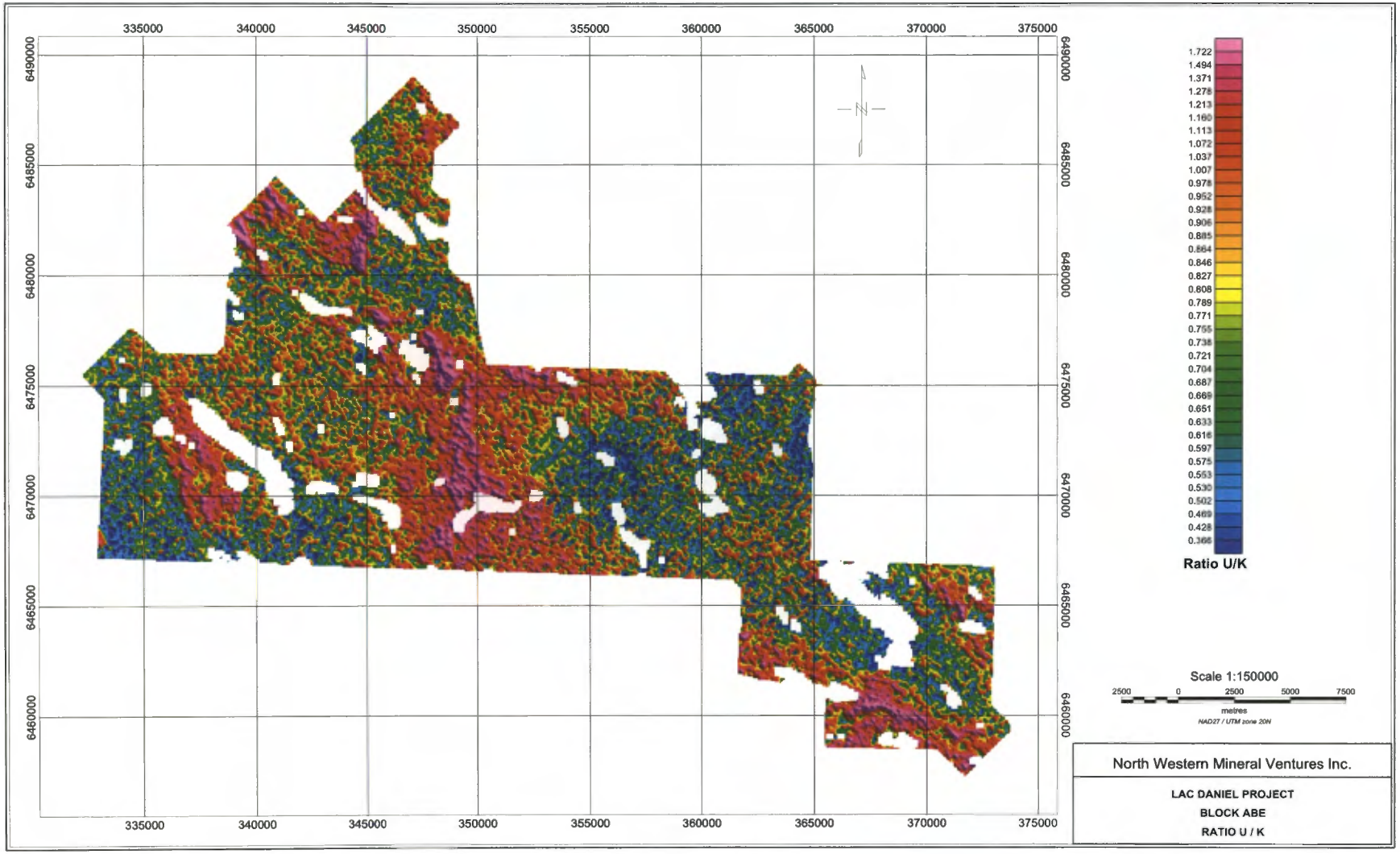


**Figure 15: Ratio U/K (Block ABE)**

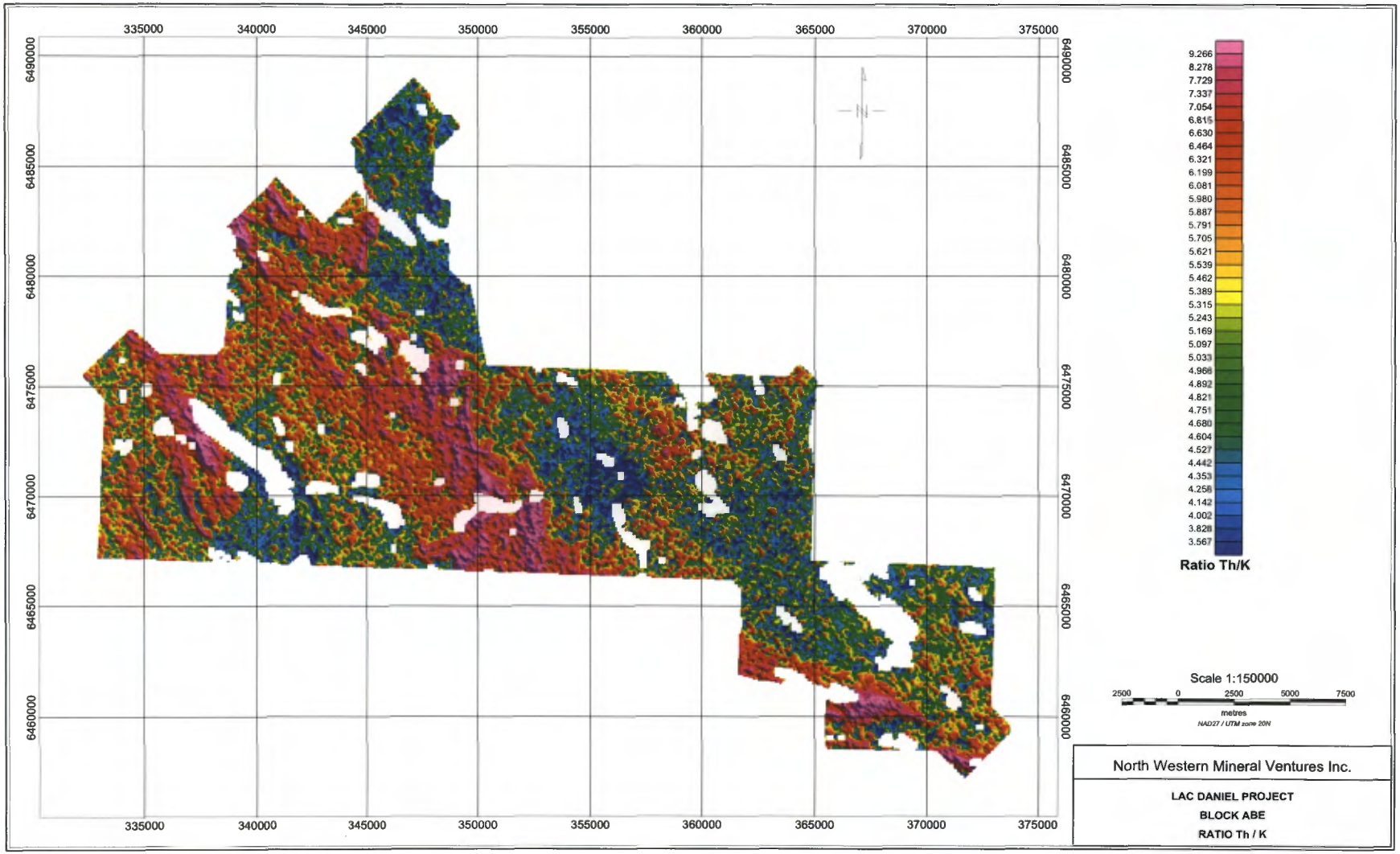


**Figure 16: Ratio Th/K (Block ABE)**

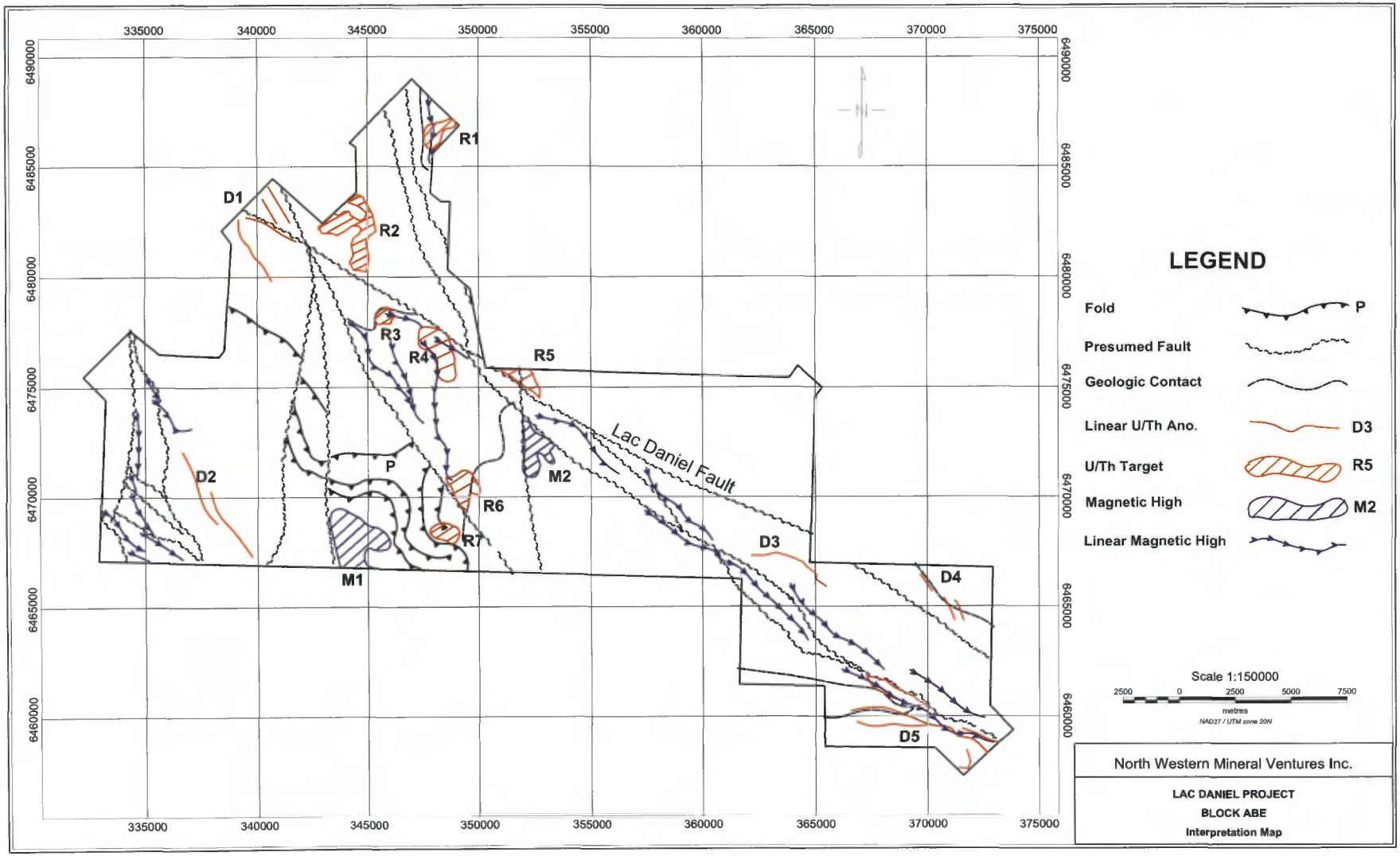


**Figure 17: Interpretation Map (Block ABE)**

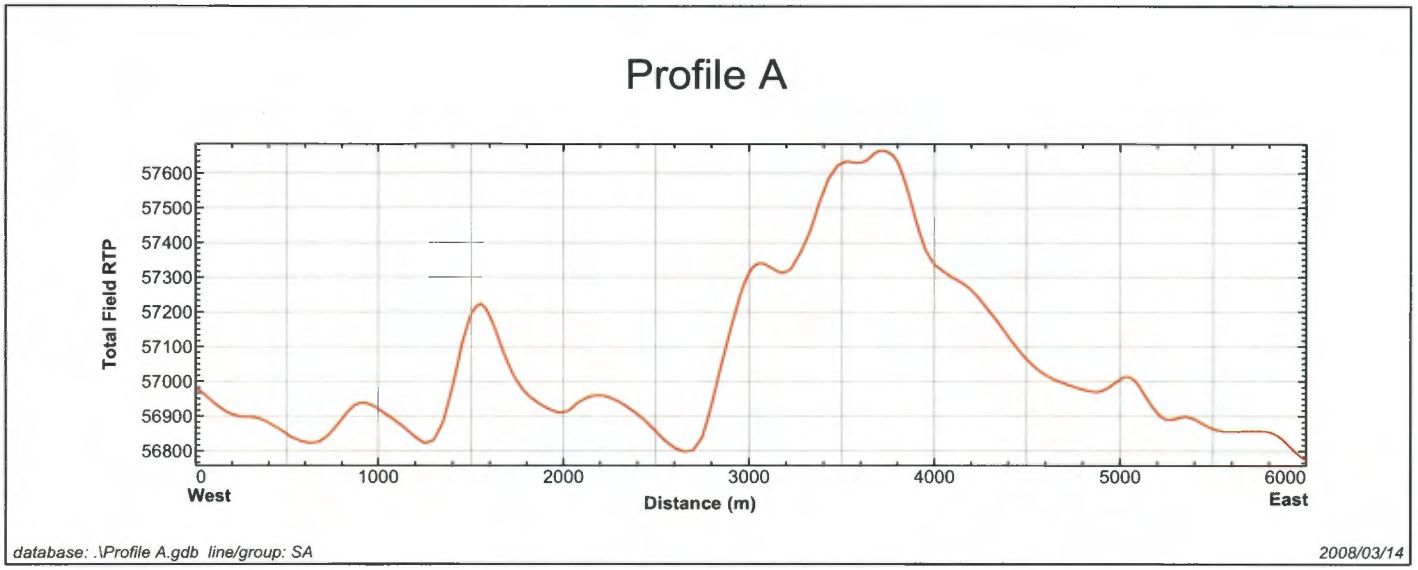


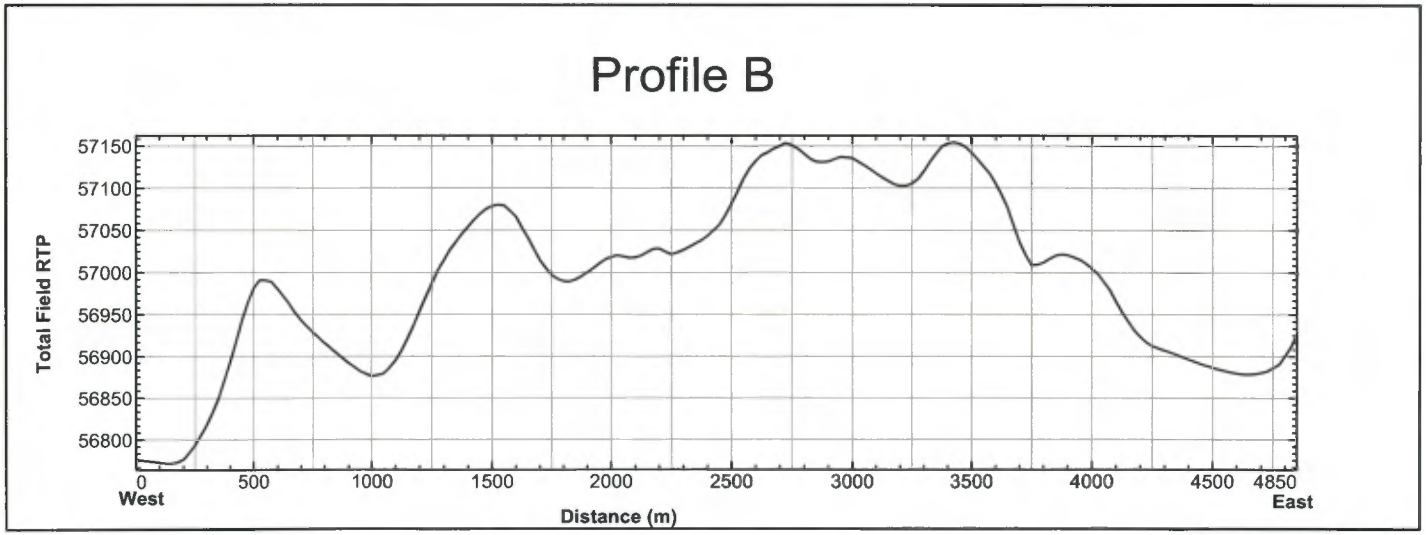


**Figure 18: Magnetic Profiles A and B**

## 5.2 Block C

### 5.2.1 Magnetic Data

For block C, the Total Magnetic Intensity Reduced to Pole map, the First Vertical Derivative map and the Analytic Signal map are presented on figure 19, 20 and 21. The Interpretation map is presented on figure 29.

The magnetic survey allowed mapping four major faults striking approximately West-North-West. Also, many linear magnetic highs were mapped in the northern part of the survey area. These highs could represent important dikes of pegmatite.

### 5.2.2 Spectrometric Data

The following maps were used for the interpretation of gamma-ray spectrometric data acquired on block C:

| | | | |
|---|---|---|---|
| - Total Count: | figure 22 | - %K: | figure 23 |
| - eqU: | figure 24 | - eqTh: | figure 25 |
| - eqU/eqTh: | figure 26 | - eqU/%K: | figure 27 |
| - eqTh/%K: | figure 28 | | |

All the gamma-ray spectrometric interpretation results were added to the magnetic data interpretation results of figure 29.

On block C, many weak uranium anomalies were mapped in the northern part of the survey area. The intensities of these anomalies are lower than 2 times the background level and most of them disappear completely on the U/Th ratio. This low response in U/Th could means that there is no major enrichment in uranium mineralization. Only one single linear U/Th anomaly (T1) remains in the centre north area of the block. This anomaly can be considered as a first priority target and ground follow up is recommended, as a first step, at the co-ordinates X= 386 250, Y= 6 481 350.

### 5.2.3 Conclusions

On block C, the magnetic survey allowed to map:

- Four major faults striking approximately West-North-West.
- Many linear magnetic highs located mainly in the northern part of the block.

On the other hand, the gamma-ray spectrometric survey provided only one first priority exploration target (T1), which should be verified with ground geologic and spectrometric works.

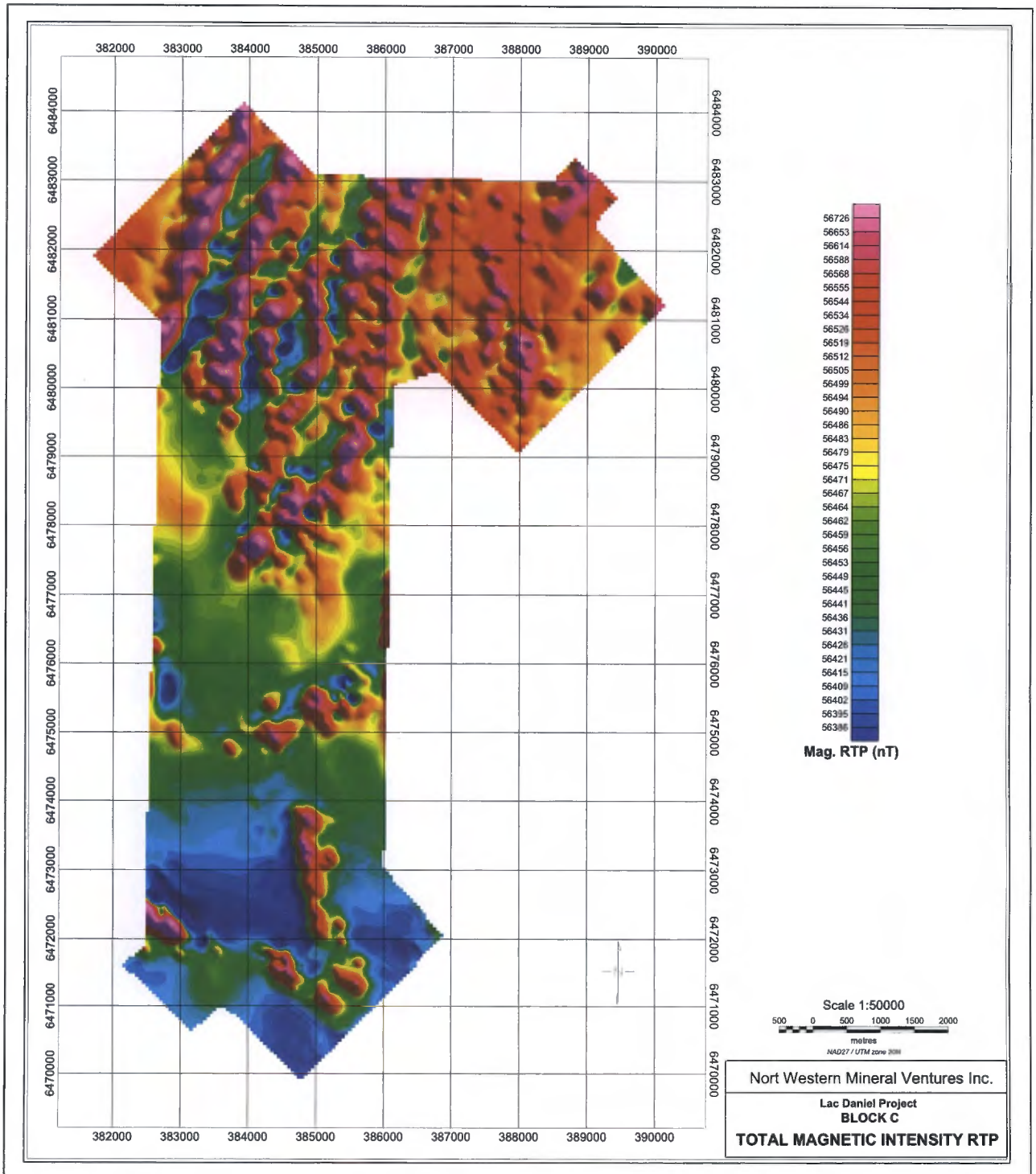


**Figure 19: Total Magnetic Intensity Reduced to Pole (Bloc C)**

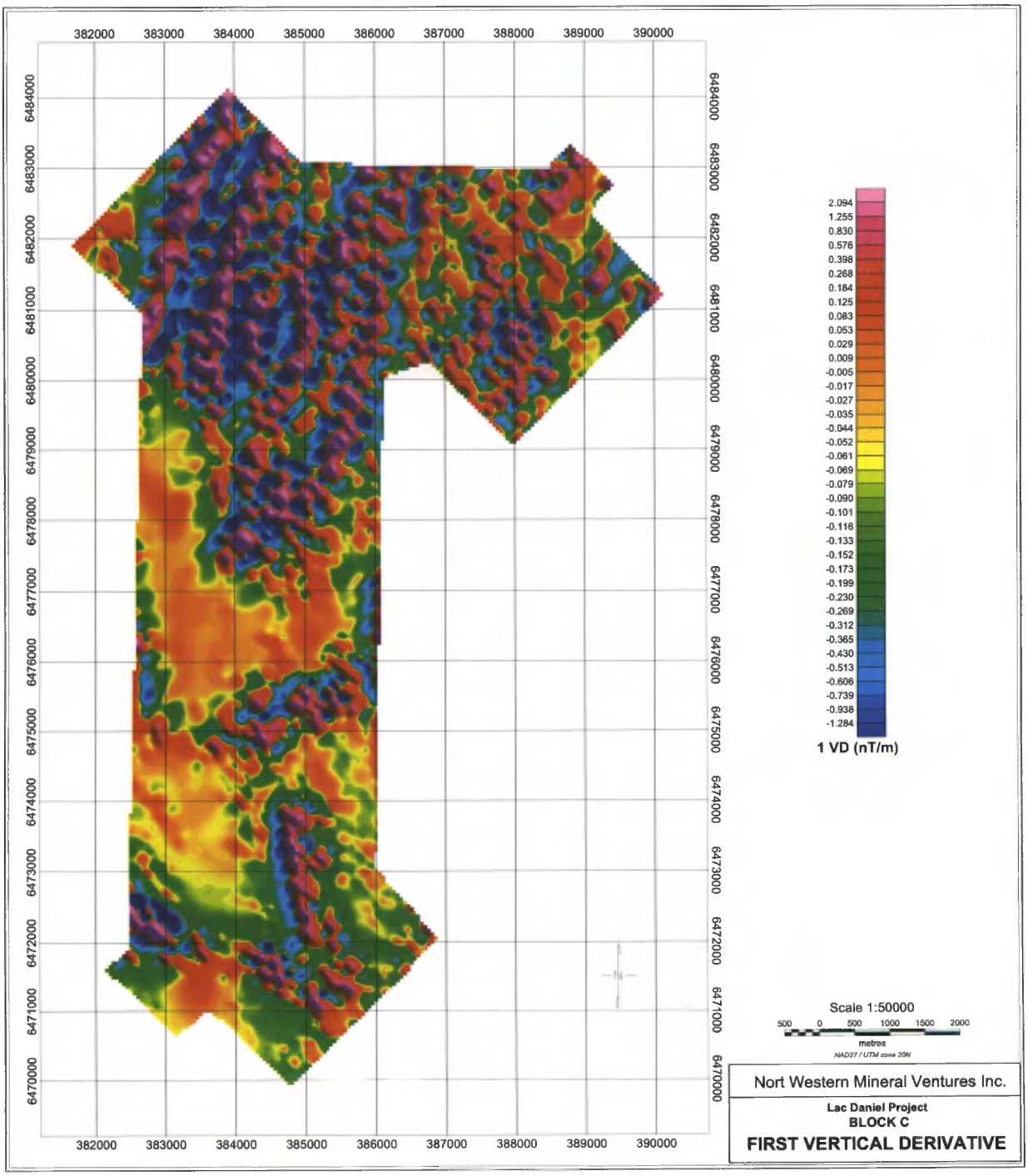


**Figure 20: First Vertical Derivative (Block C)**

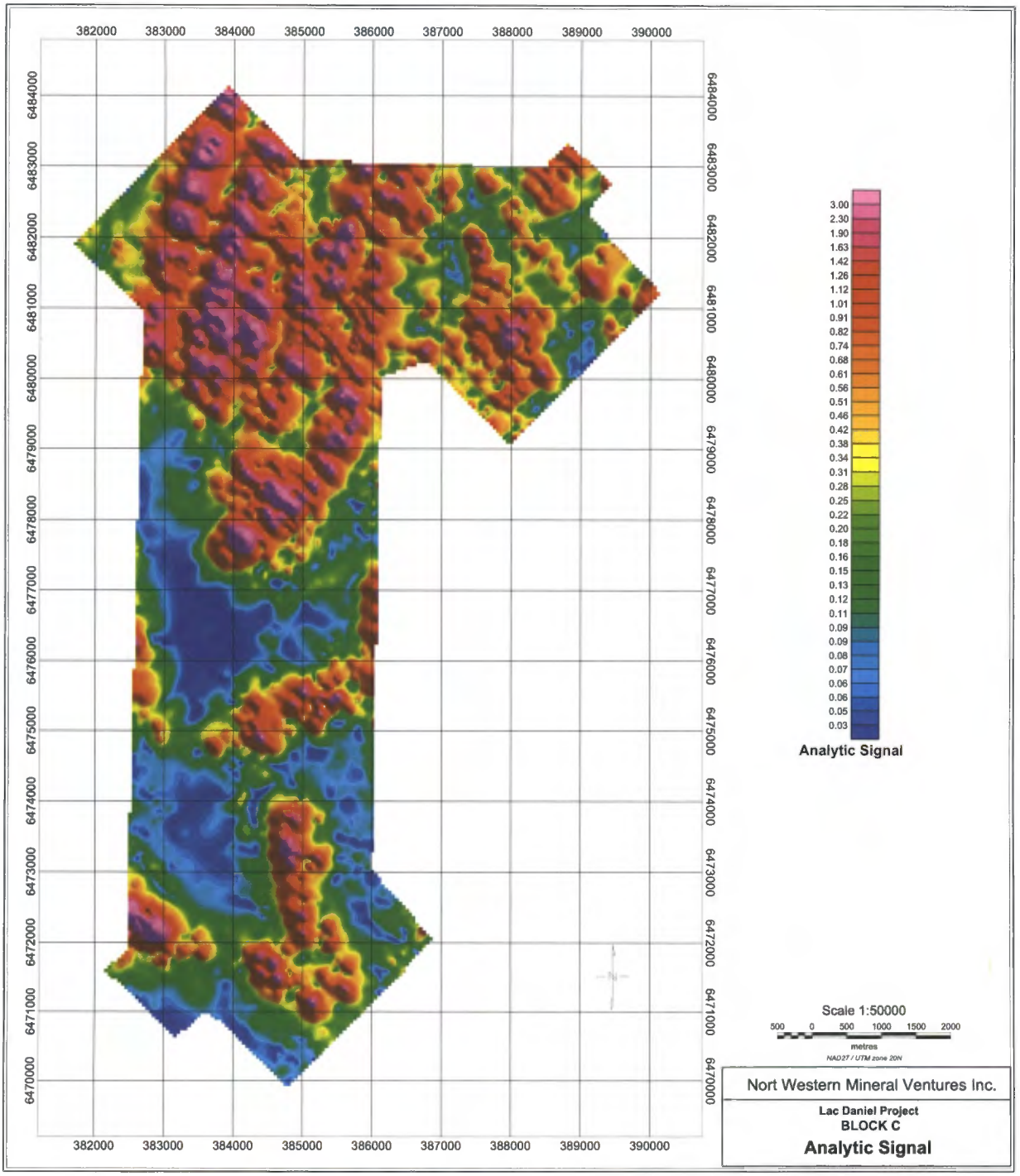


**Figure 21: Analytic Signal (Block C)**

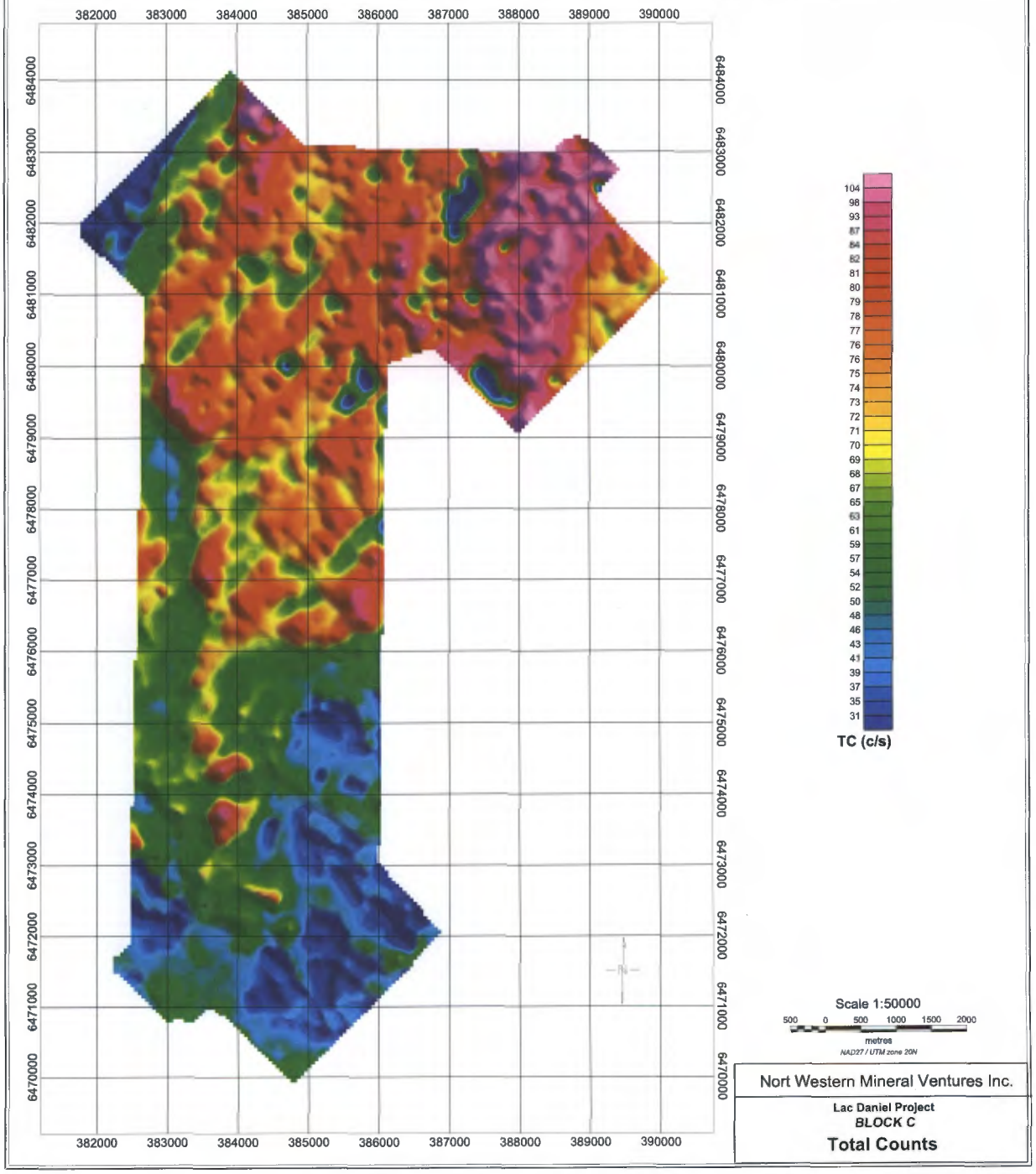


**Figure 22: Total Counts (Block C)**

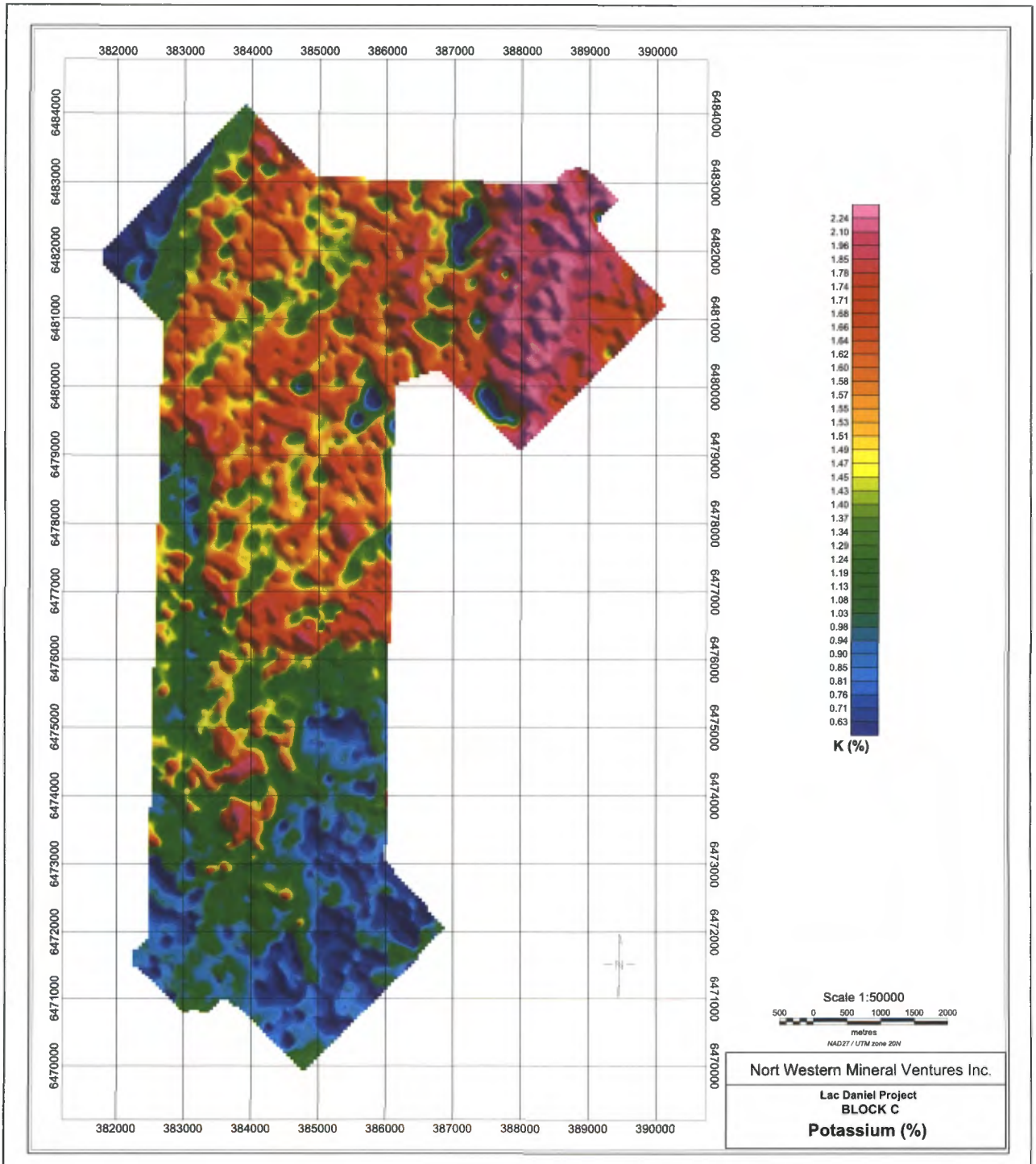


**Figure 23: Potassium (%) (Block C)**

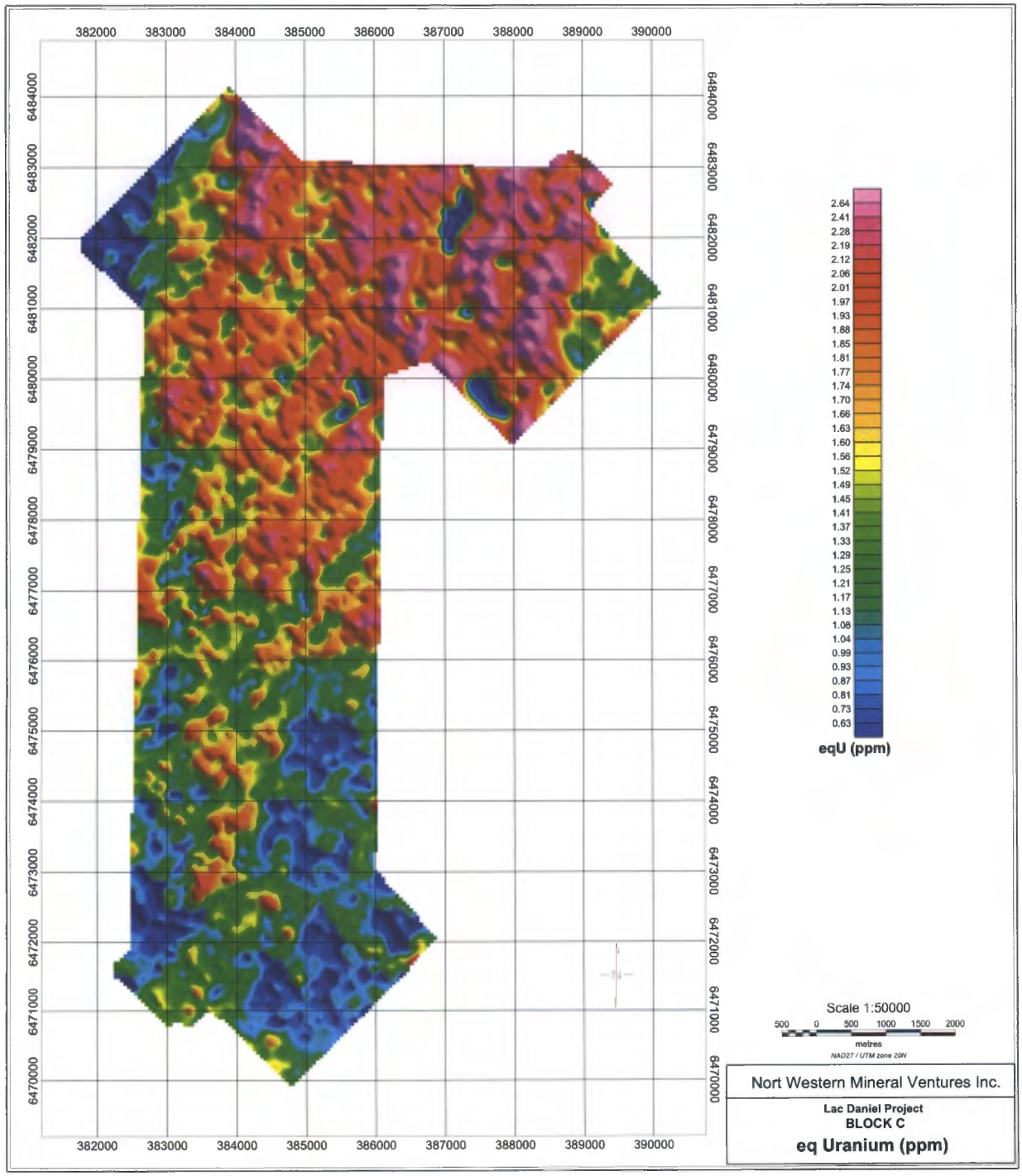


**Figure 24: Equivalent Uranium (ppm) (Block C)**

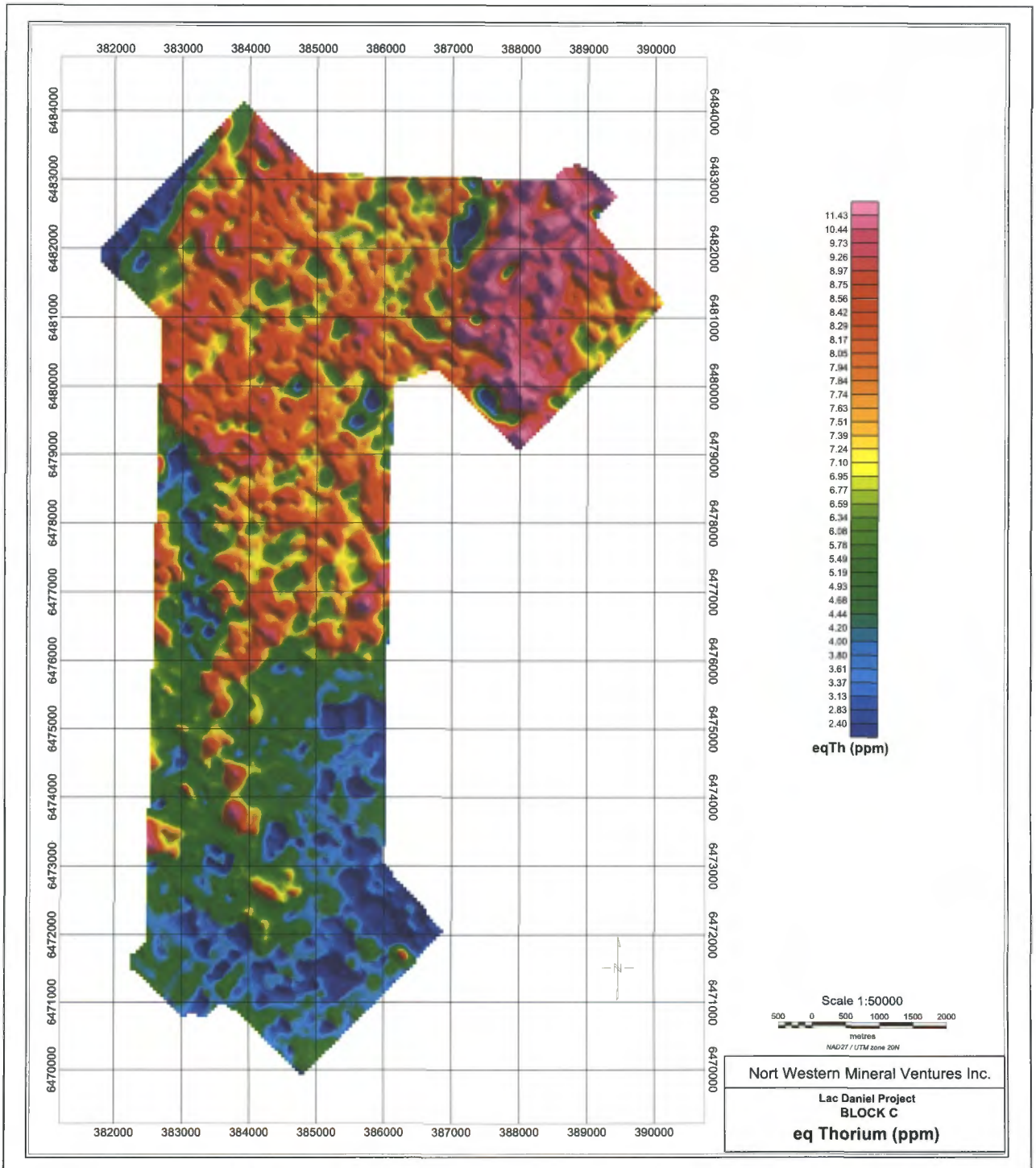


**Figure 25: Equivalent Thorium (ppm) (Block C)**

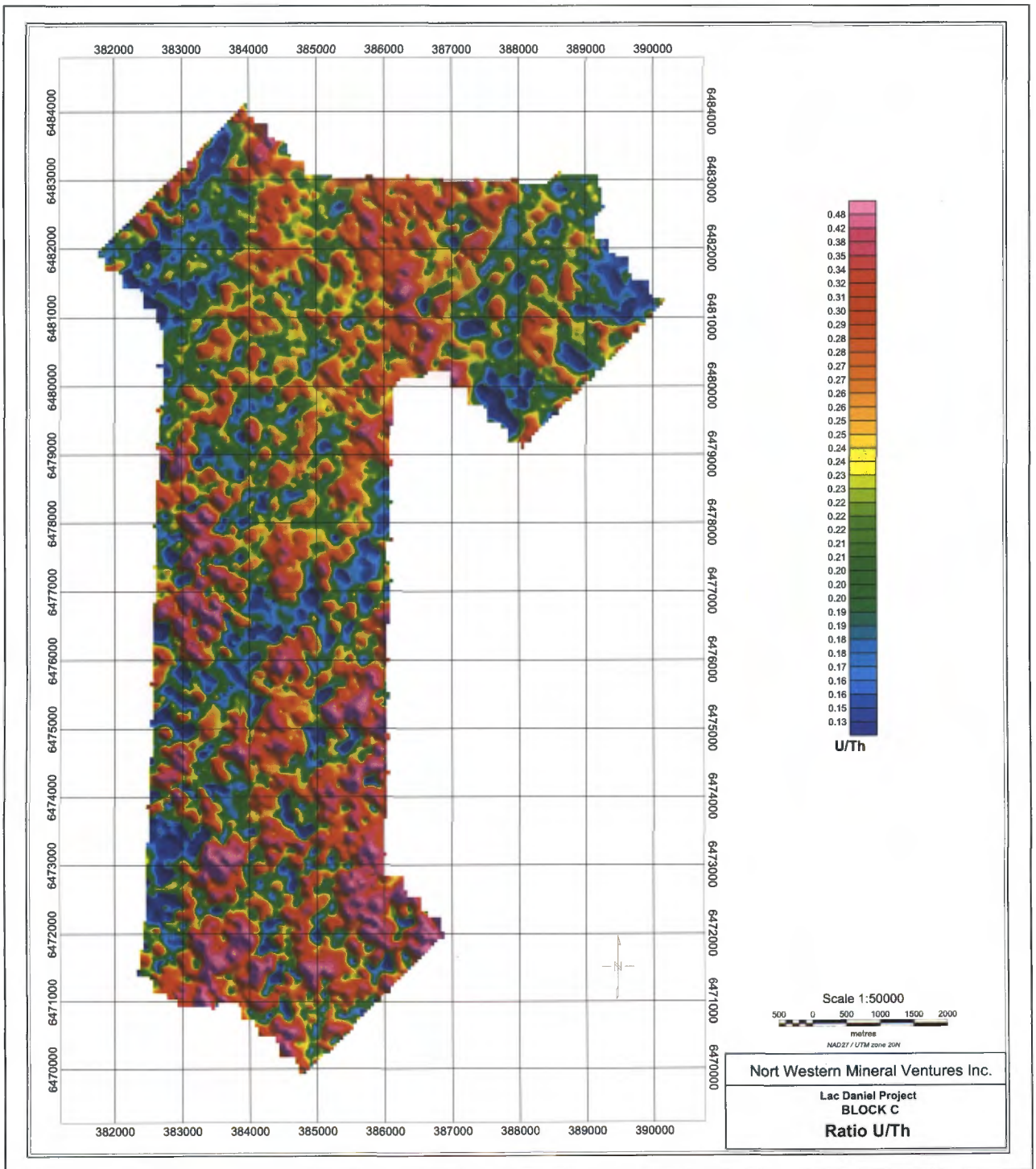


**Figure 26: Ratio U/Th (Block C)**

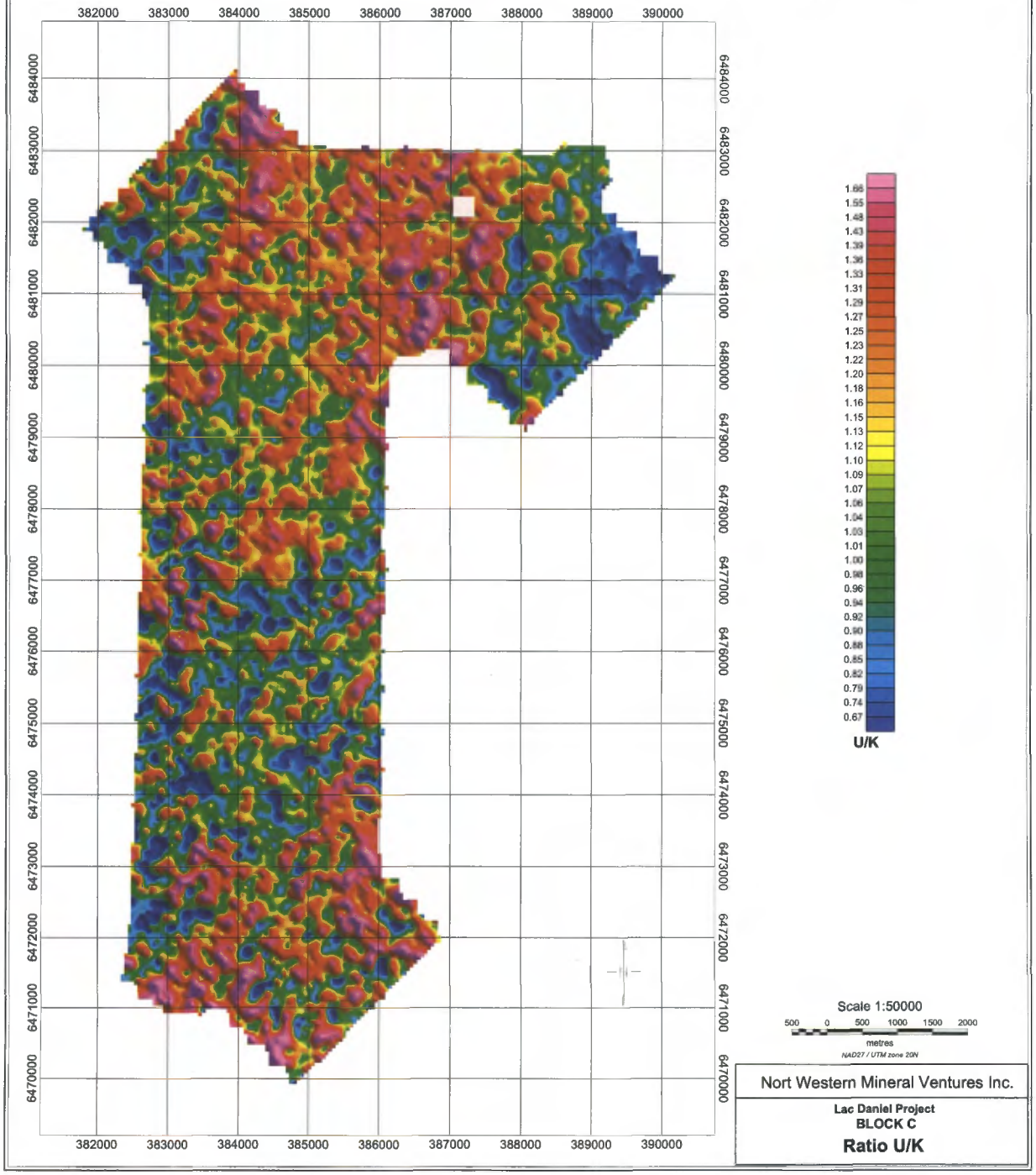


**Figure 27: Ratio U/K (Block C)**

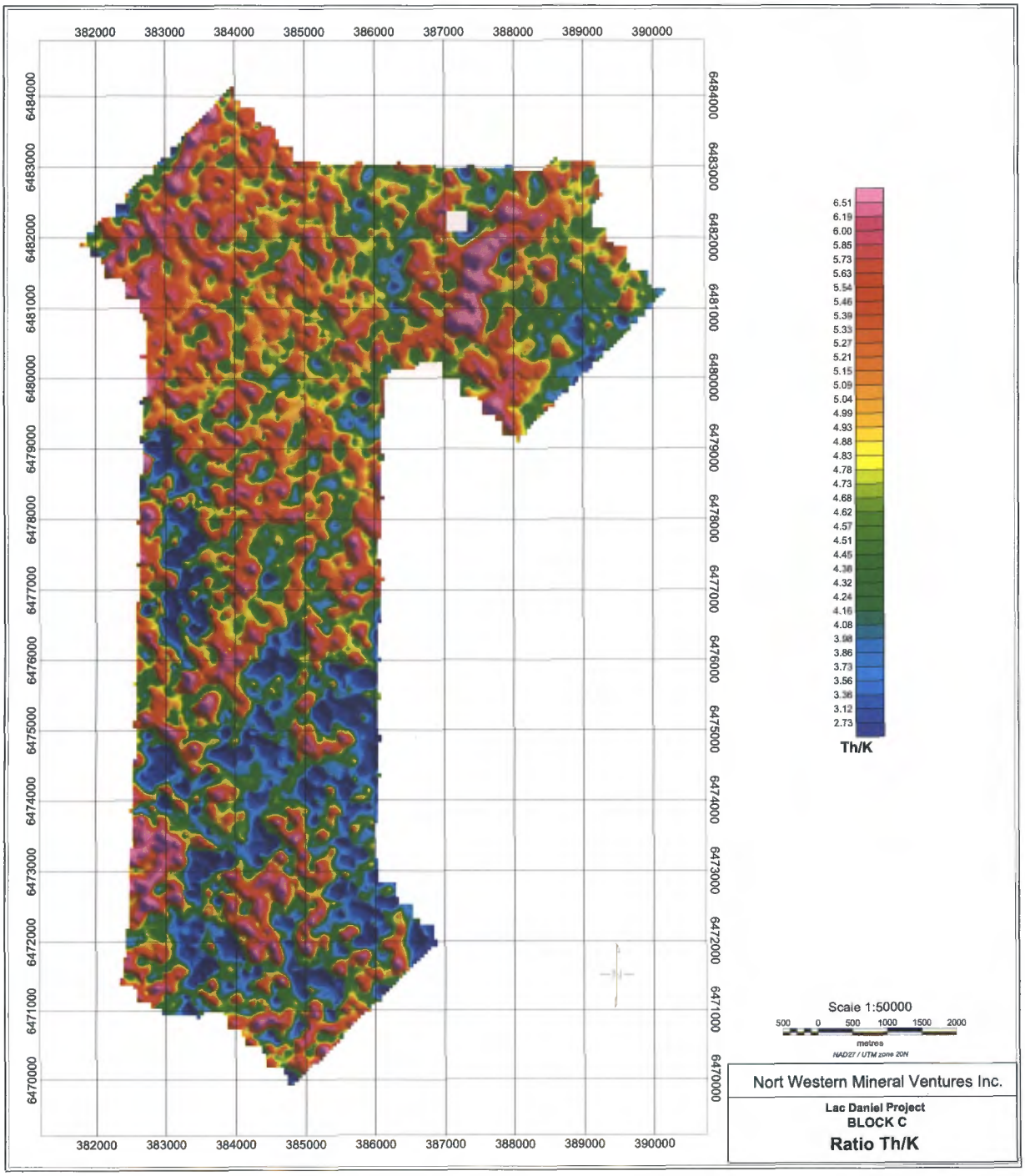


**Figure 28: Ratio Th/K (Block C)**

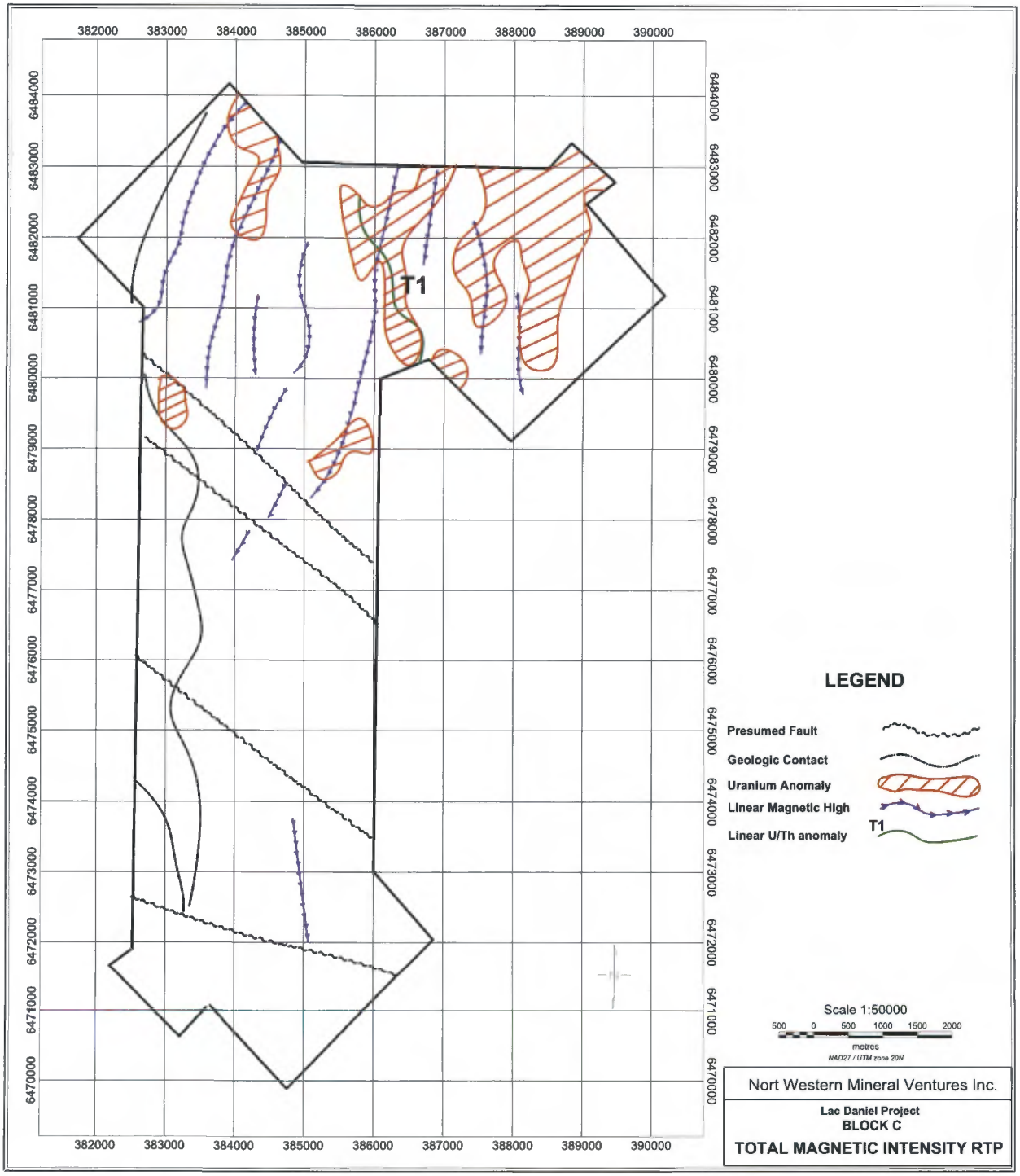


**Figure 29: Interpretation Map (Block C)**

## 5.3 Block F

### 5.3.1 Magnetic Data

For block F, the Total Magnetic Intensity Reduced to Pole map, the First Vertical Derivative map and the Analytic Signal map are presented on figure 30, 31 and 32. The Interpretation map is presented on figure 40.

The magnetic survey allowed mapping many major faults striking mainly North-North-West. Another network of three faults is oriented West-North-West.

Two magnetic highs are observed in the centre-West part of the survey area (M1 and M2). These anomalies should be related to more mafic rocks. Many linear magnetic highs take place inside the two fault networks. These highs could represent important dikes of pegmatite.

### 5.3.2 Spectrometric Data

The following maps were used for the interpretation of gamma-ray spectrometric data acquired on block F:

| | | | |
|---|---|---|---|
| - Total Count: | figure 33 | - %K: | figure 34 |
| - eqU: | figure 35 | - eqTh: | figure 36 |
| - eqU/eqTh: | figure 37 | - eqU/%K: | figure 38 |
| - eqTh/%K: | figure 39 | | |

All the gamma-ray spectrometric interpretation results were added to the magnetic data interpretation results of figure 40.

On block F, many weak uranium anomalies were mapped, mainly in the southern half part of the block (figure 35). The intensities of these anomalies are lower than 2 times the background level and most of them disappear completely on the U/Th ratio (figure 37).

On the other hand, the U/Th map shows three sprawled U/Th anomalies (R1, R2 and R4) and one long linear anomaly (R3).

Unfortunately, the largest R1 U/Th anomaly, located in the northern part of the block, is not a true U/Th anomaly. In fact, no significant uranium values were detected over it. The U/Th anomaly is essentially due to very low Th values measured in the area and making the ratio U/Th wrongly high. The same situation is observed over the long linear U/Th anomaly R3.

However, the R2 and R4 U/Th anomalies represent significant exploration targets. Their signal to noise ratios is more than 2 and both should be considered as first priority targets. Ground follow up is recommended, as a first step, at the following UTM co-ordinates:

- Anomaly R2: X= 327 500, Y= 6 478 480
- Anomaly R4: X= 327 800, Y= 6 476 380

High values of the U/K ratio are observed over the anomalies R2 and R4 showing that there is no preferential enrichment of potassium relative to uranium.

### 5.3.3 Conclusions

On block F, the magnetic survey allowed to map:

- Two fault networks striking approximately West-North-West and North-North-West;
- Two magnetic highs located in the centre West part of the survey area;
- Many linear magnetic highs taking place inside the two fault networks.

The gamma-ray spectrometric survey provided two significant exploration targets, which should be considered as first priority.

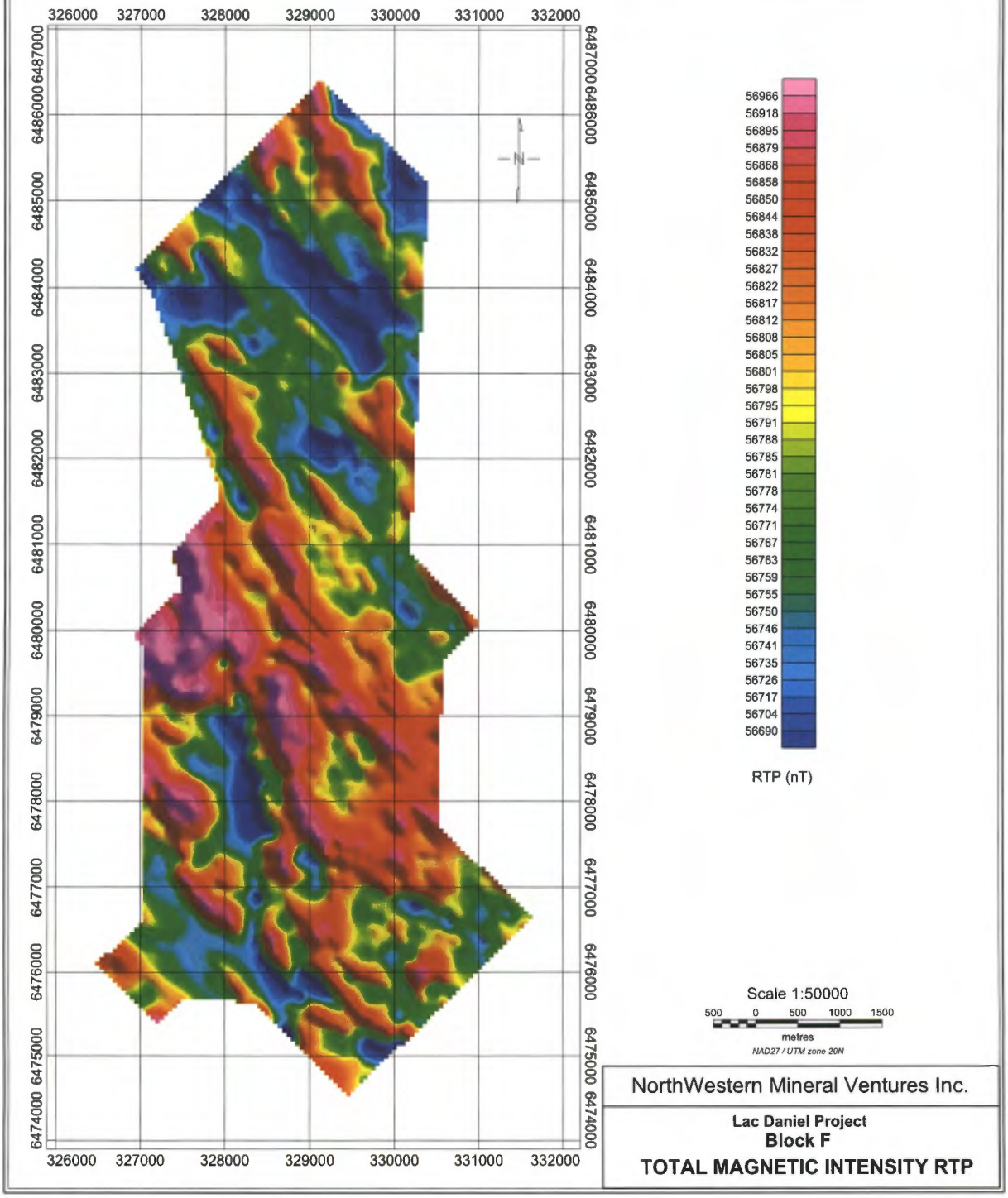


**Figure 30: Total Magnetic Intensity Reduced to Pole (Bloc F)**

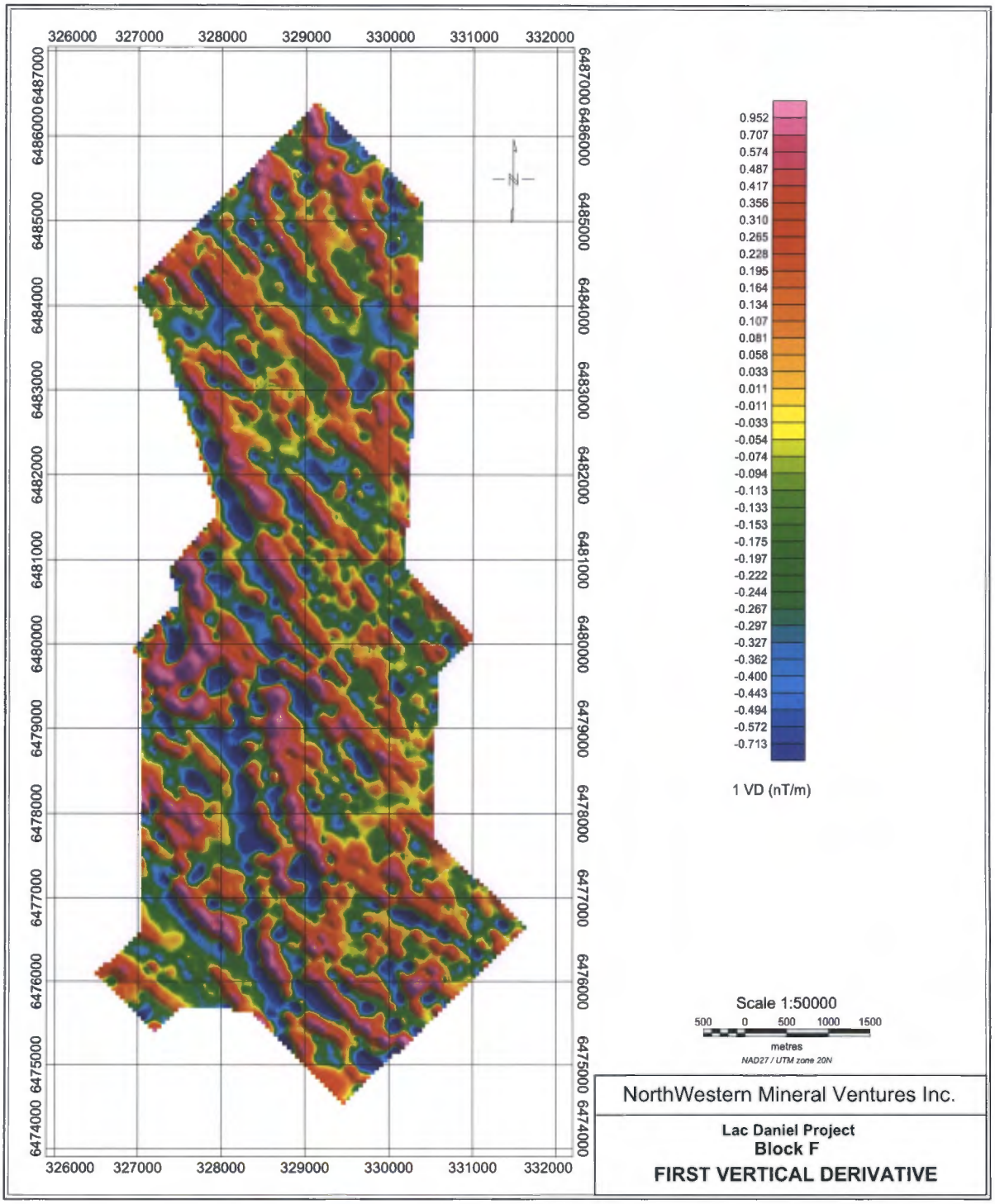


**Figure 31: First Vertical Derivative (Block F)**

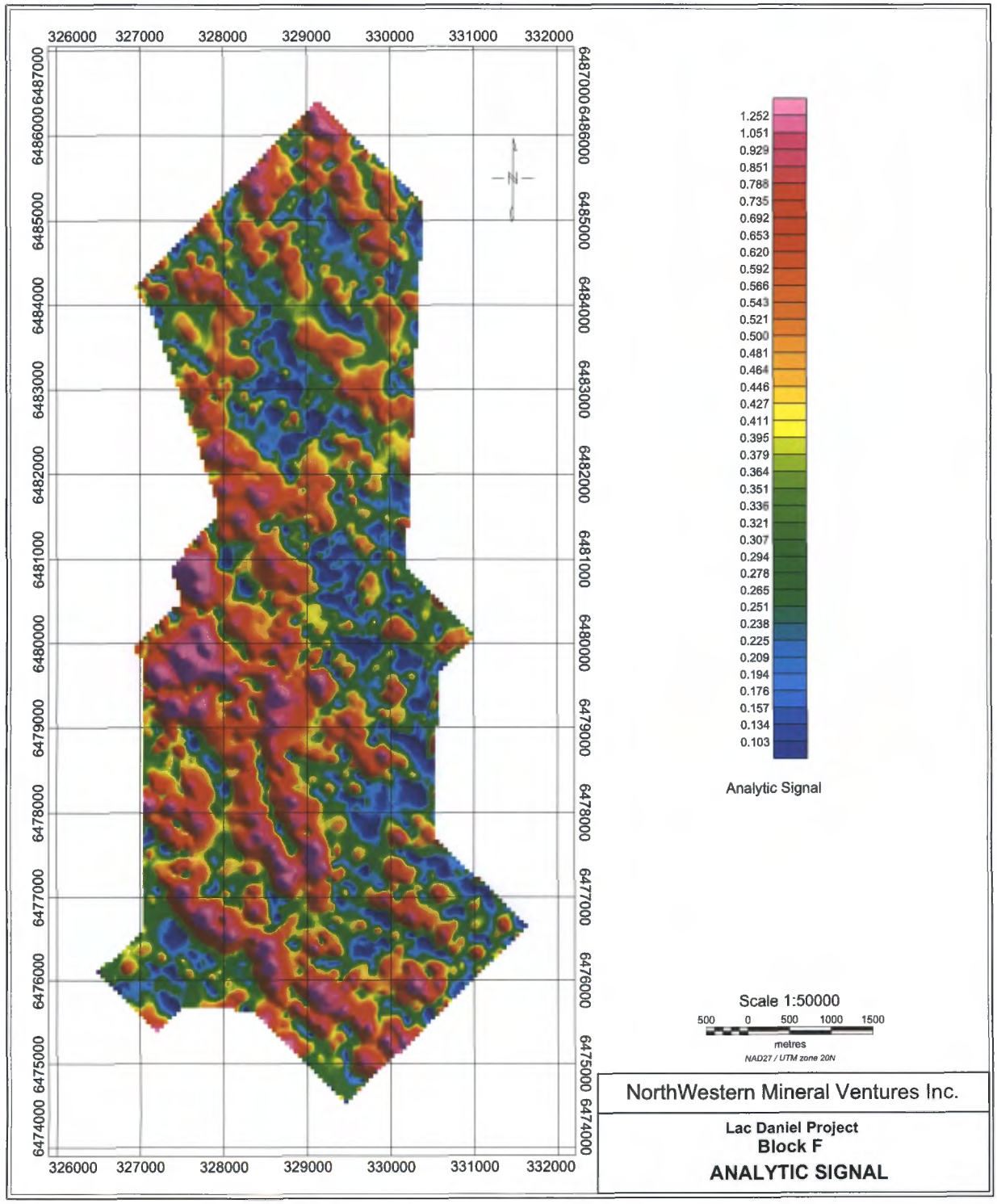


**Figure 32: Analytic Signal (Block F)**

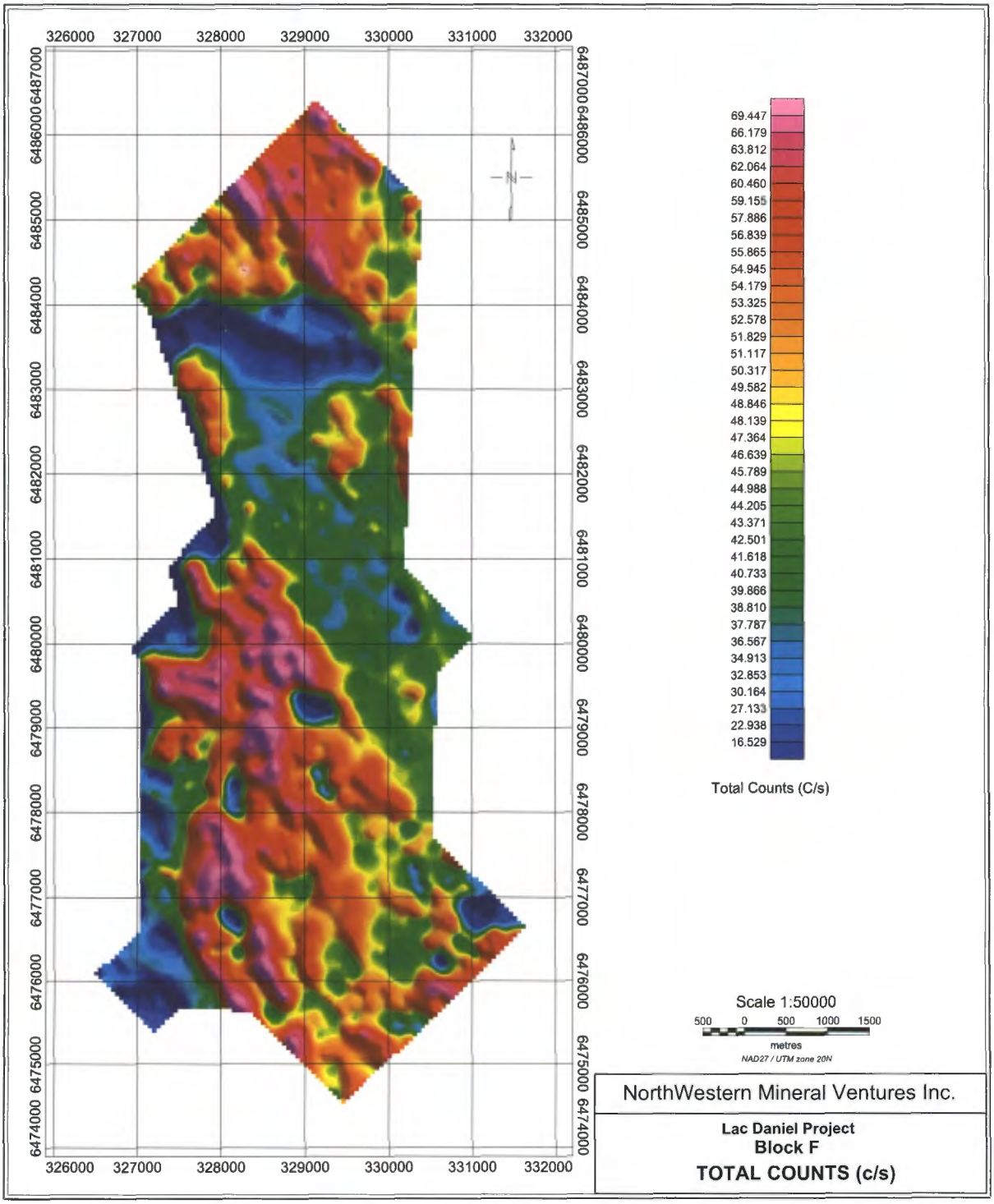


**Figure 33: Total Counts (Block F)**

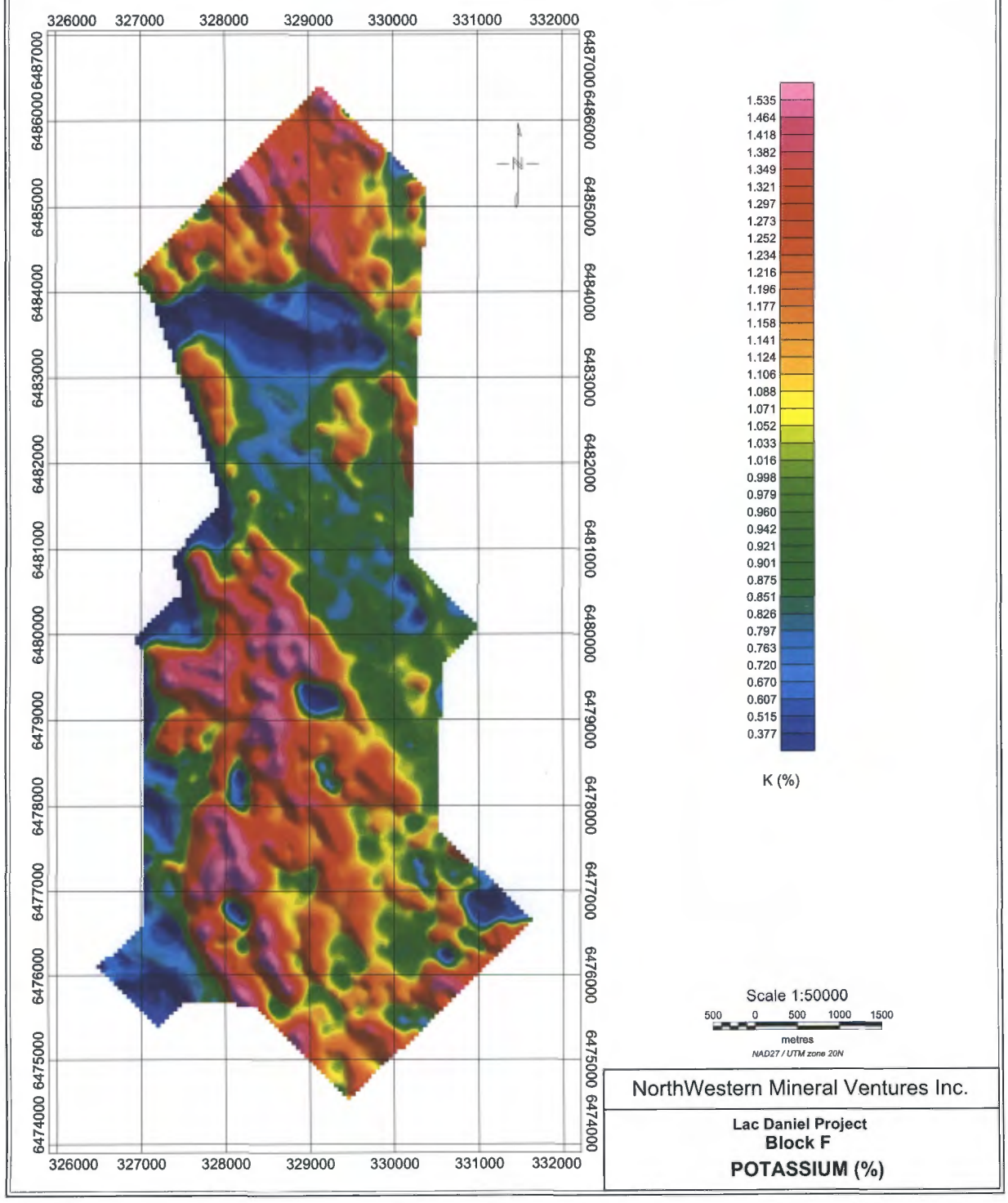


**Figure 34: Potassium (%) (Block F)**

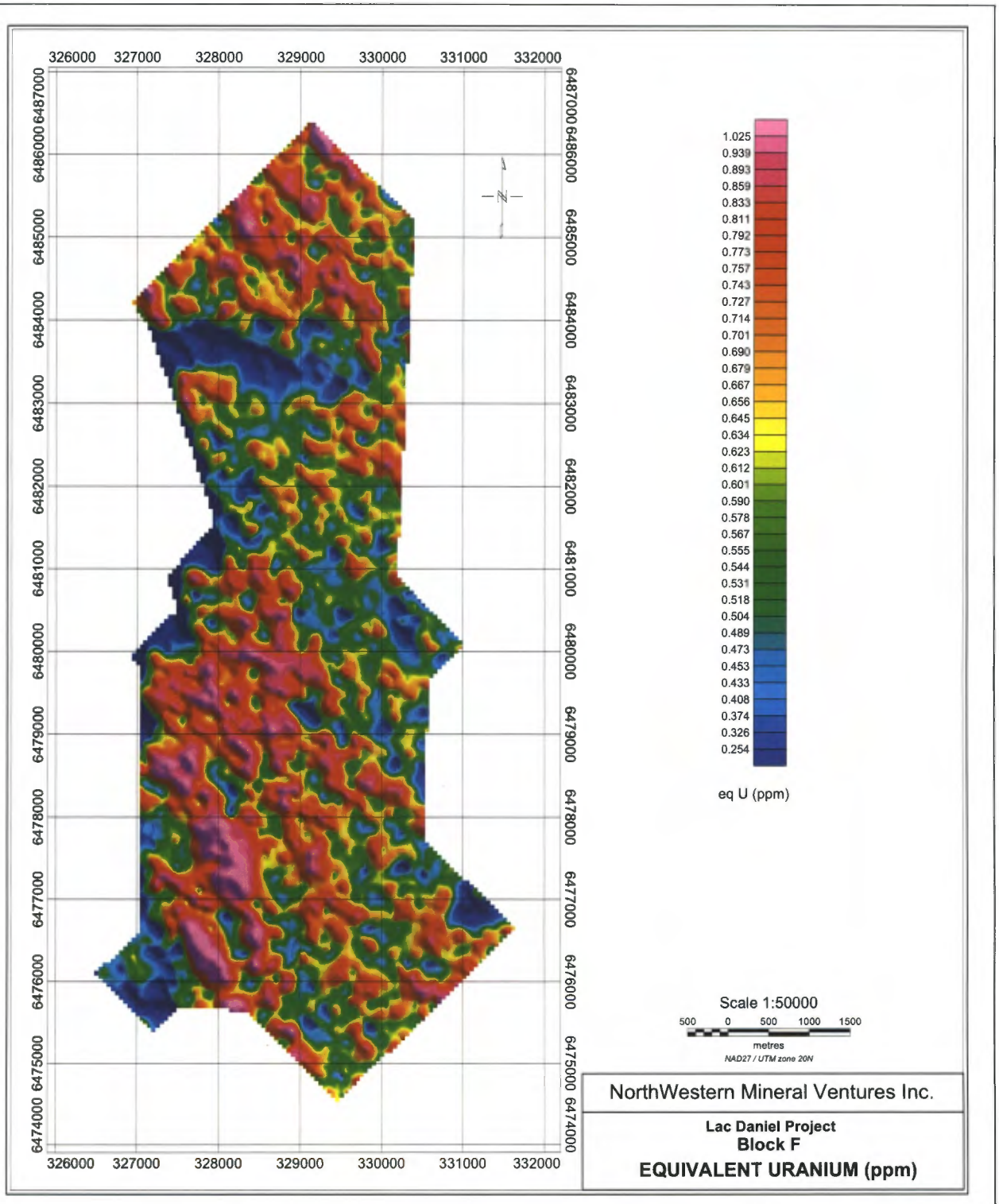


**Figure 35: Equivalent Uranium (ppm) (Block F)**

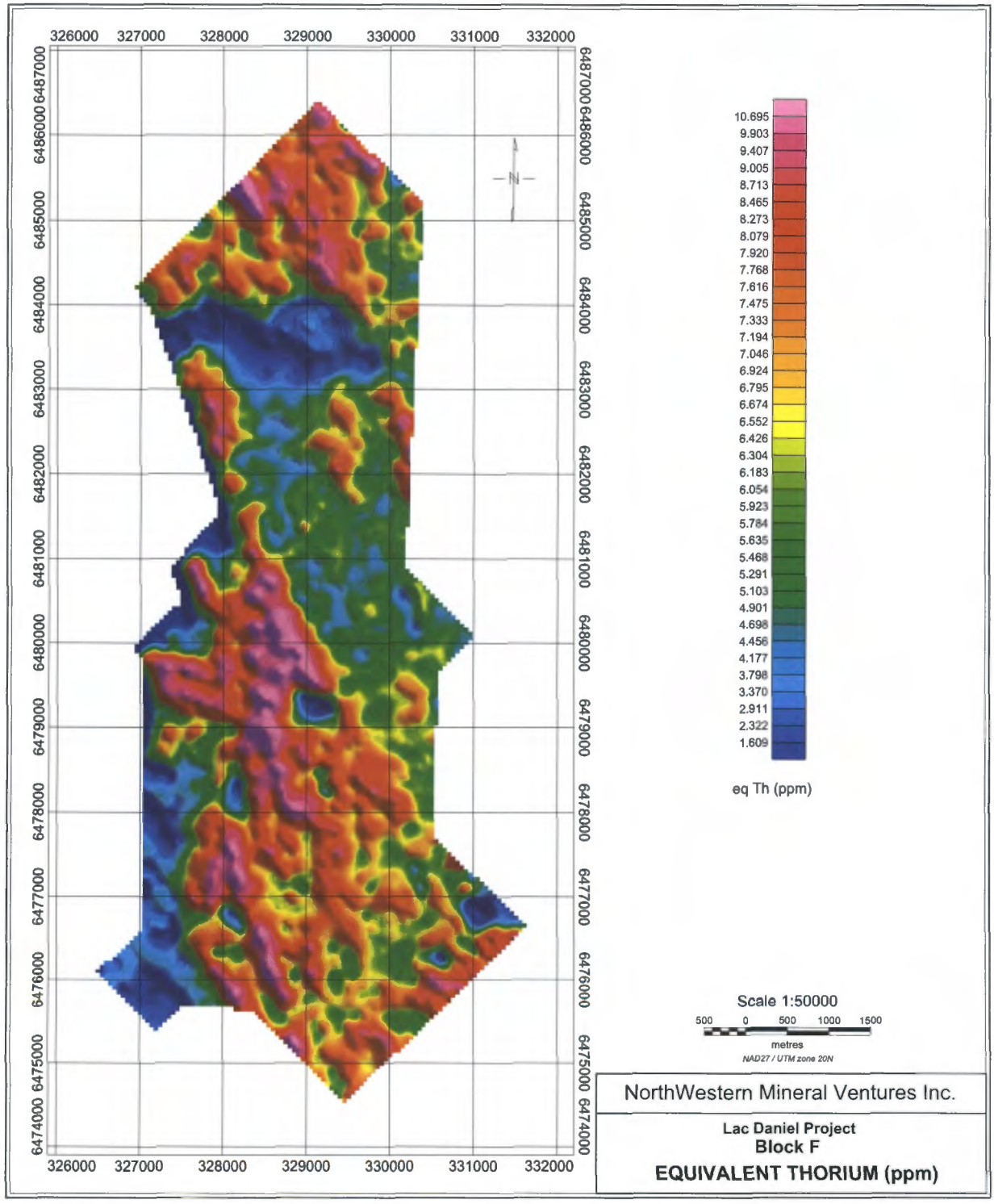


**Figure 36: Equivalent Thorium (ppm) (Block F)**

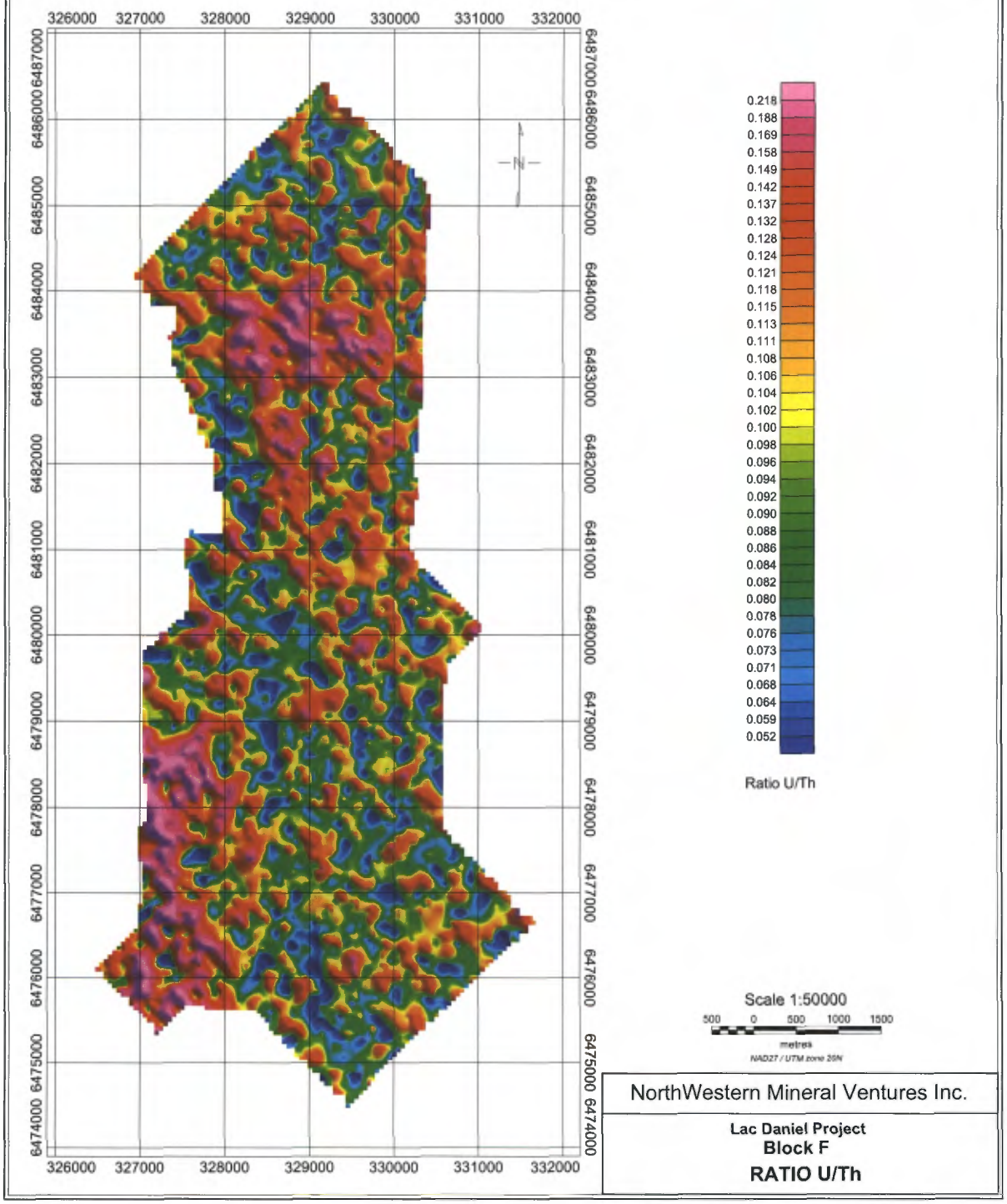


**Figure 37: Ratio U/Th (Block F)**

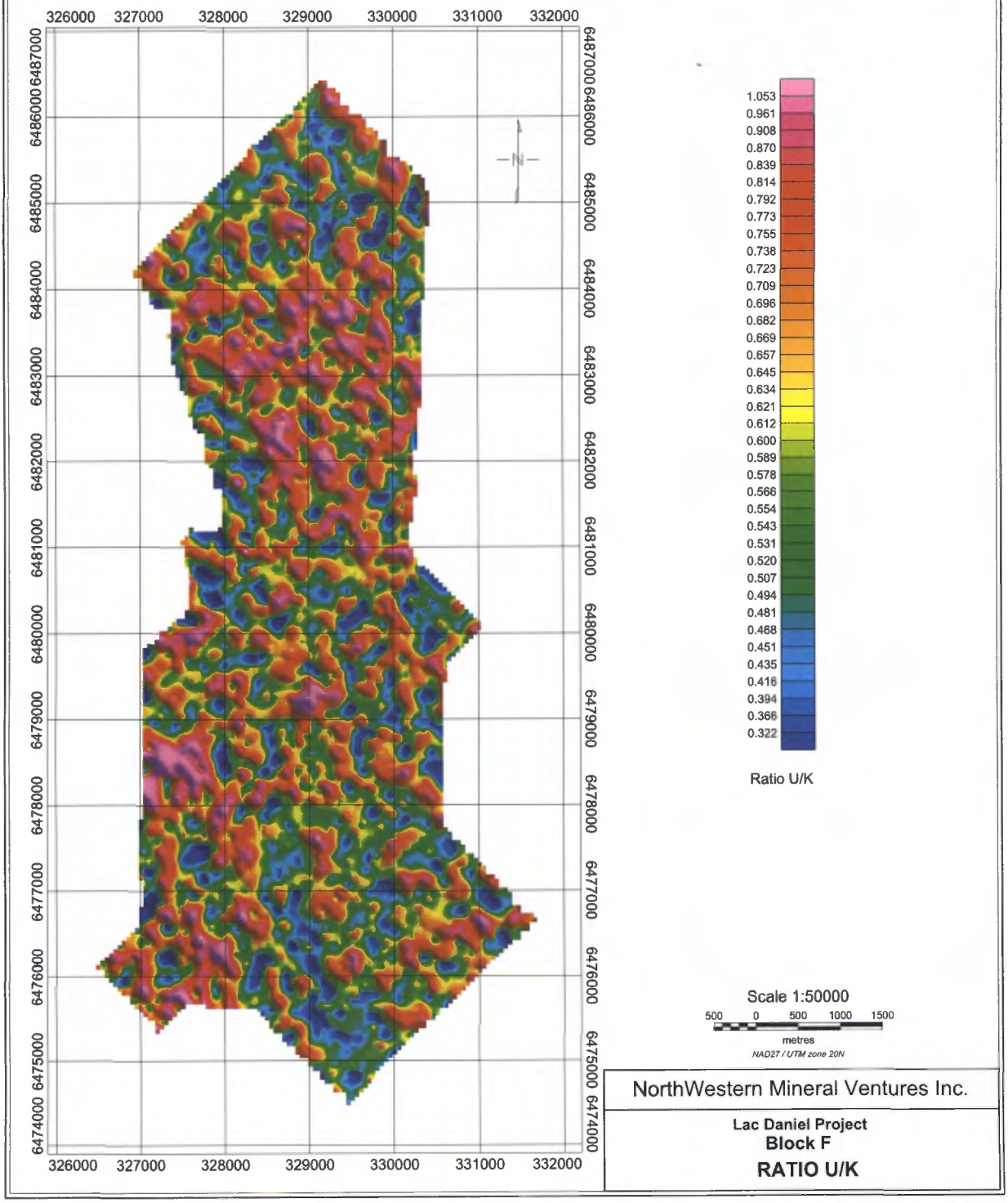


**Figure 38: Ratio U/K (Block F)**

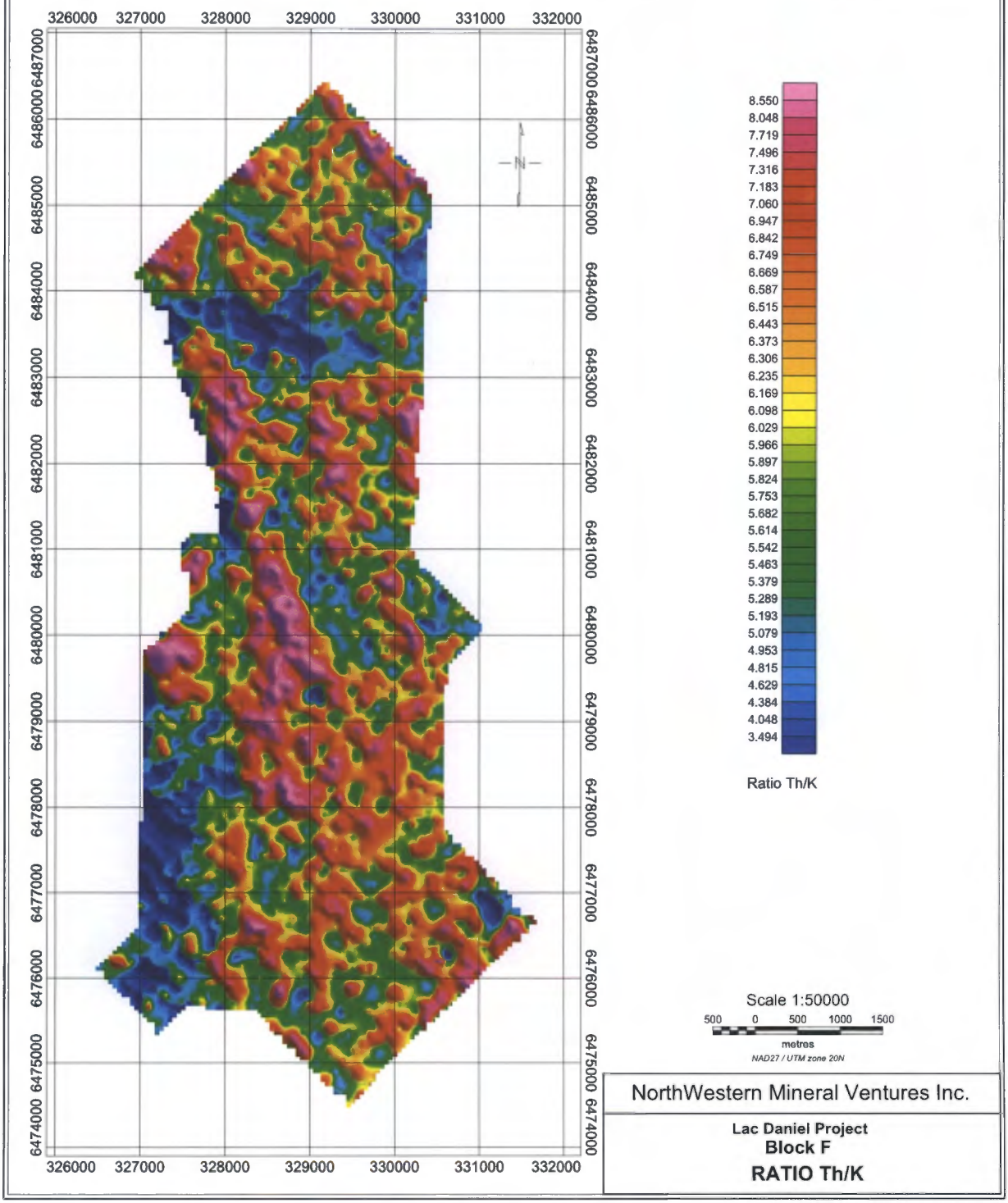


**Figure 39: Ratio Th/K (Block F)**

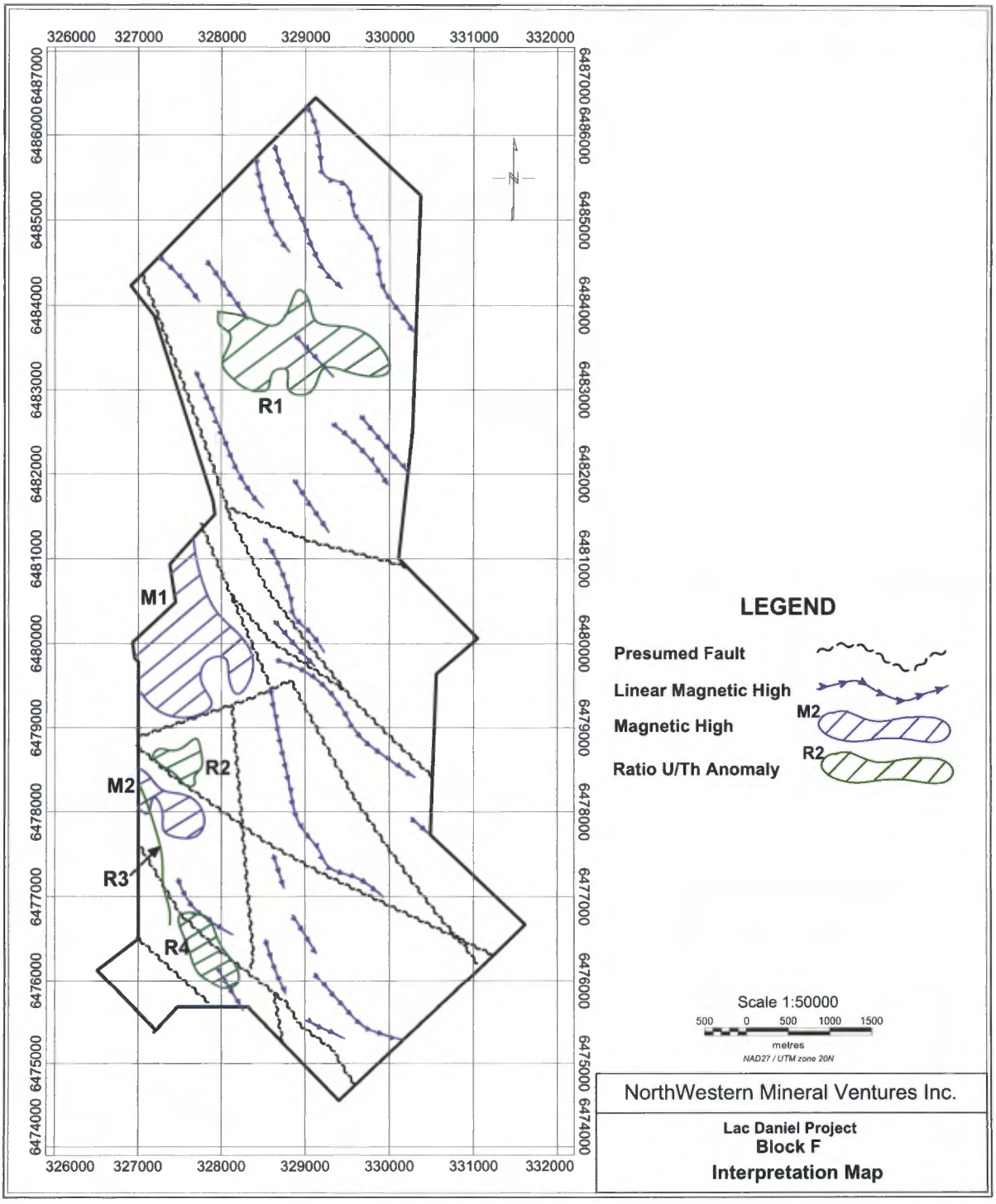


**Figure 40: Interpretation Map (Block F)**

## 5.4 Block G

### 5.4.1 Magnetic Data

The Total Magnetic Intensity Reduced to Pole map, the First Vertical Derivative map and the Analytic Signal map are presented on figure 41, 42 and 43. The Interpretation map is presented on figure 51.

The magnetic survey allowed mapping four parallel faults striking approximately North-North-West. A fifth fault oriented North-West was also interpreted. This fault network cross two geologic folds located in the centre part of the block.

Three small magnetic highs were also mapped in the northern part of the survey area. These highs, noted as M1, M2 and M3, should correspond to small intrusive mafic bodies located at depth.

Finally, some linear magnetic anomalies are observed in the southern part of the area. These elongated magnetic highs could represent significant dikes of pegmatite.

### 5.4.2 Spectrometric Data

The following maps were used for the interpretation of gamma-ray spectrometric data acquired on block G:

- Total Count: figure 44
- %K: figure 45
- eqU: figure 46
- eqTh: figure 47
- eqU/eqTh: figure 48
- eqU/%K: figure 49
- eqTh/%K: figure 50

All the gamma-ray spectrometric interpretation results were added to the magnetic data interpretation results of figure 51.

On block G, three weak linear uranium anomalies (D1, D2 and D3) and one weak potato-shaped uranium anomaly (R1) were mapped. The three linear uranium anomalies draw a semicircle interrupted by the fault network. The potato-shaped uranium anomaly is located in the centre of this semicircle and at the intersection of two faults. The intensities of all these uranium anomalies are lower than two times the background level and all disappear completely on the U/Th ratio map. This low response in U/Th could means that there is no major enrichment in uranium mineralization.

However, on the U/Th map, two new U/Th anomalies (T1 and T2) were observed where no uranium anomaly was detected. These anomalies represent false anomalies caused by very low Thorium counts, making the U/Th ratio higher than it should be. Some holes, with no data, are also observed on the U/Th grid. These holes correspond to dummy values applied when Thorium counts are lower than a certain threshold (avoiding a division by zero).

### 5.4.3 Conclusions

On block G, the magnetic survey allowed to map:

- Four parallel faults striking approximately North-North-West and one fault oriented North-West.
- A double geologic fold, located in the centre-west part of the block.
- Two linear magnetic anomalies located in the southern part of the block.
- Three magnetic highs located in the northern part of the survey area.

On the other hand, the gamma-ray spectrometric survey failed to map interesting exploration target.

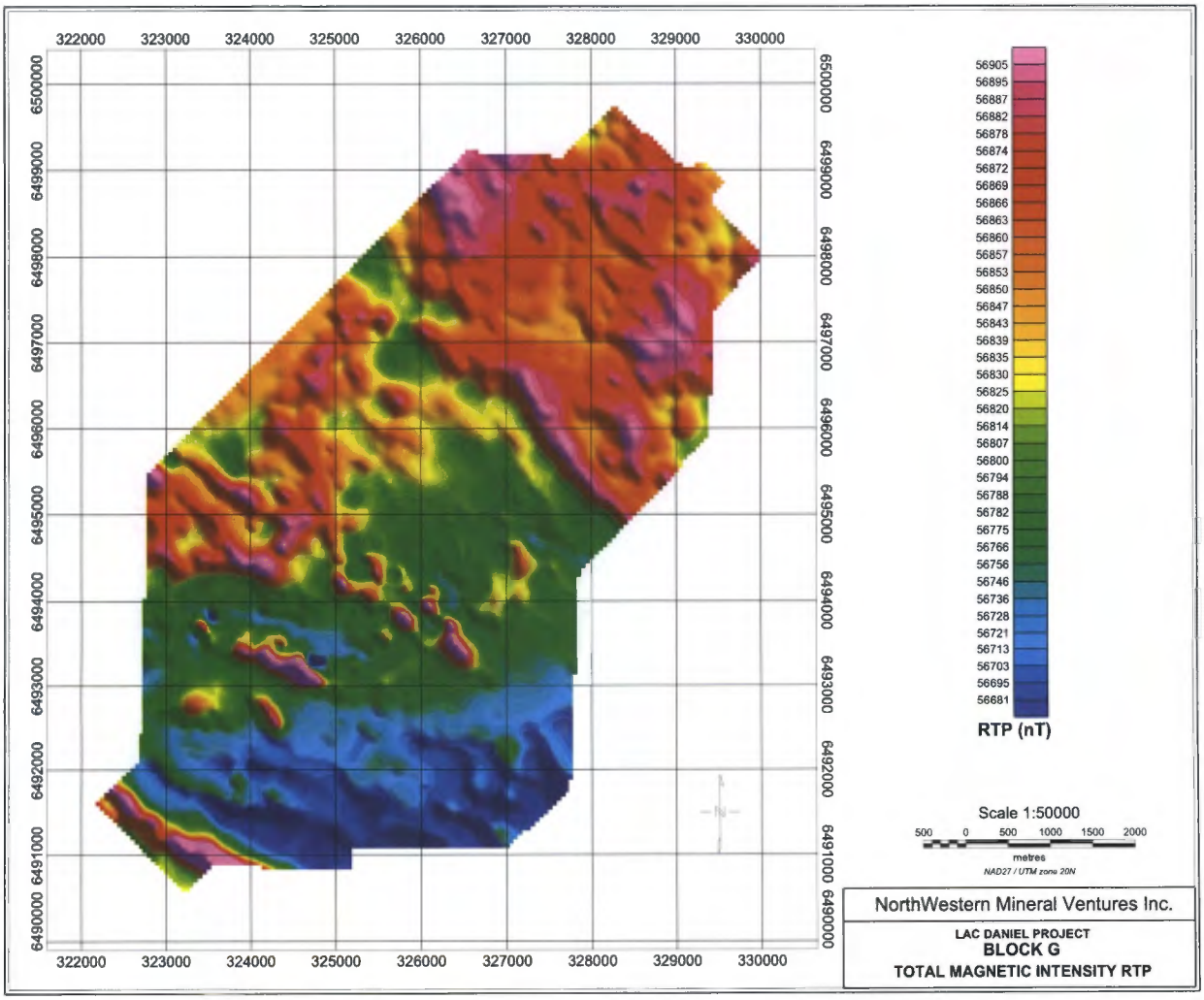


**Figure 41: Total Magnetic Intensity Reduced to Pole (Bloc G)**

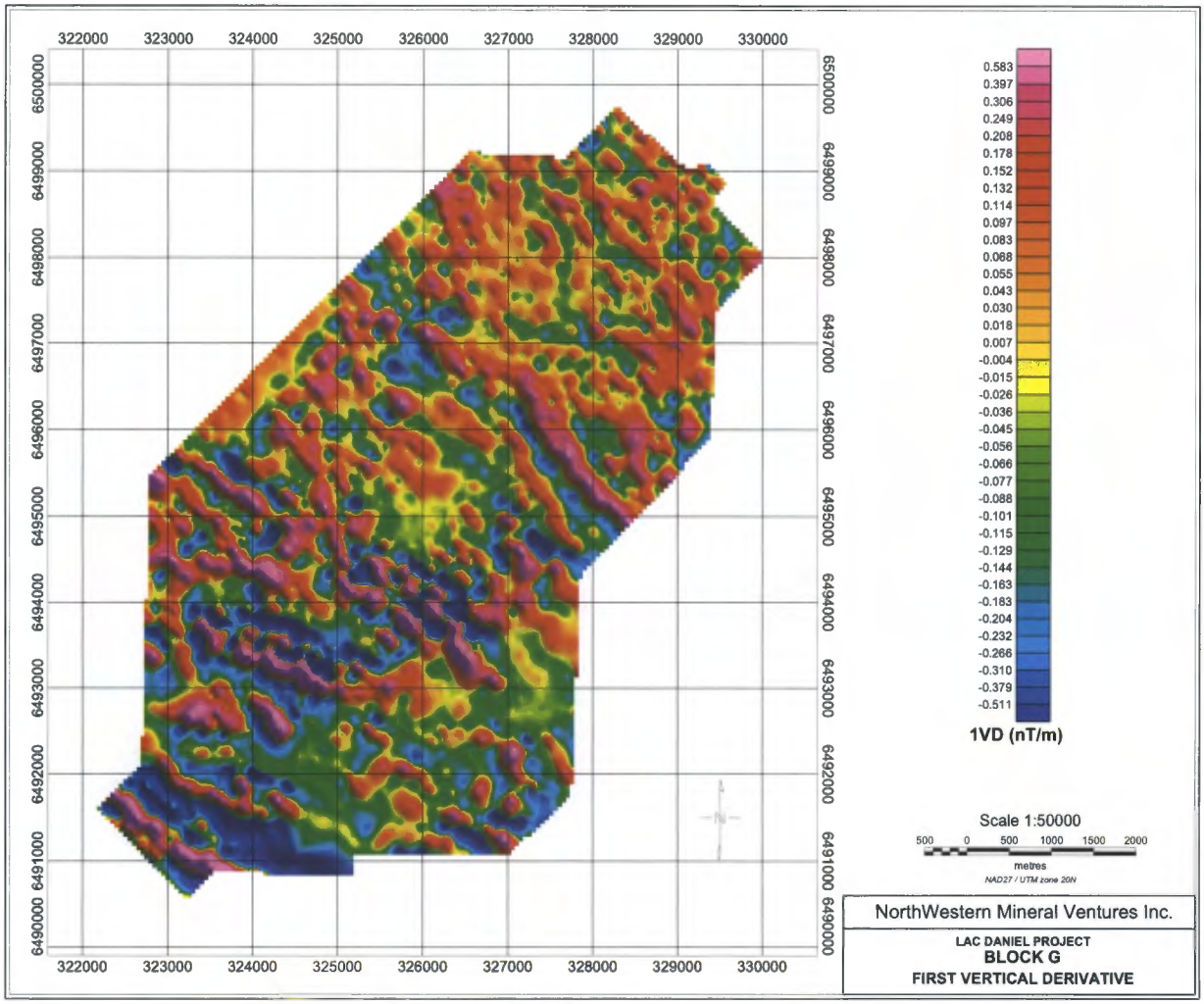


**Figure 42: First Vertical Derivative (Block G)**

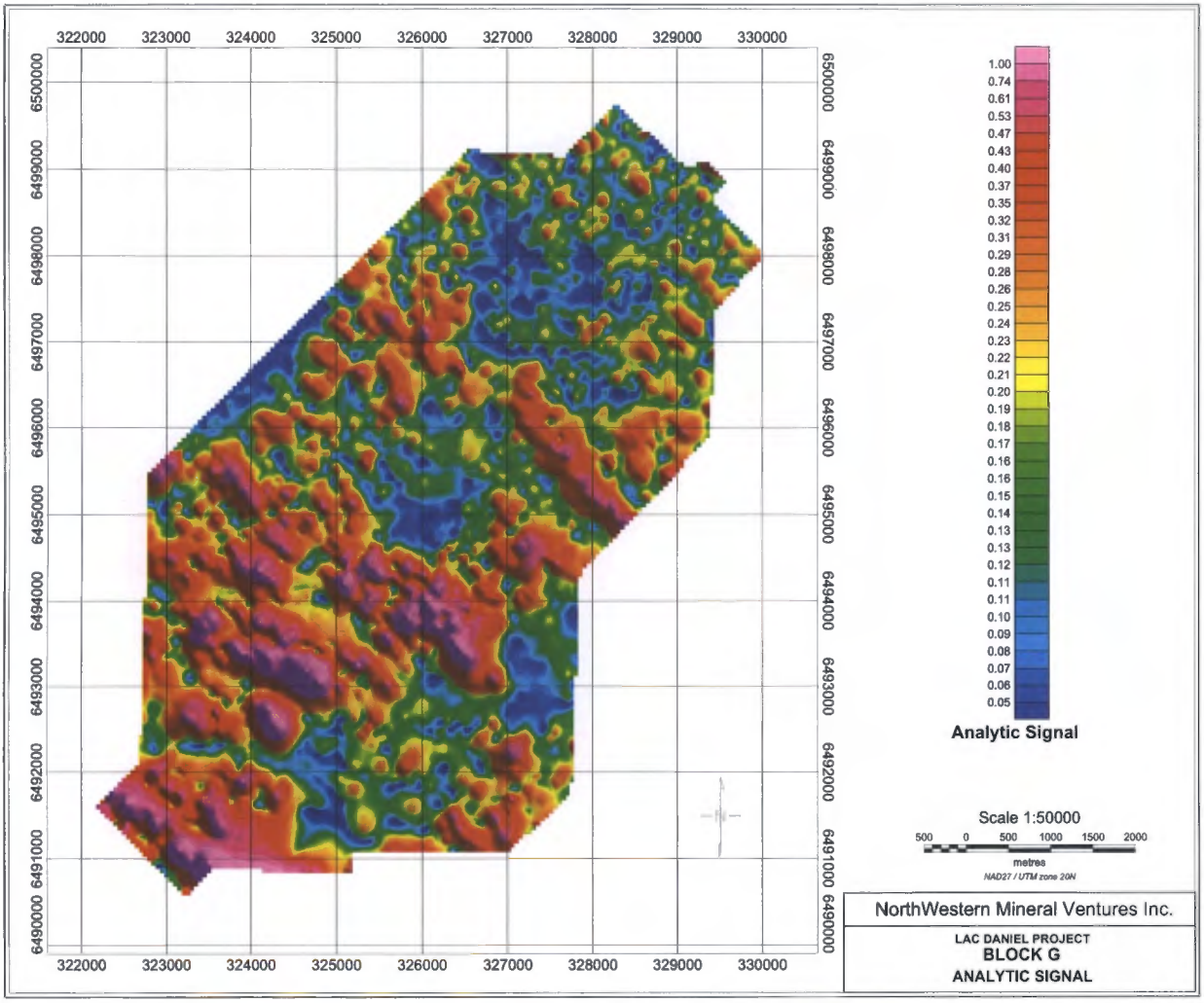


**Figure 43: Analytic Signal (Block G)**

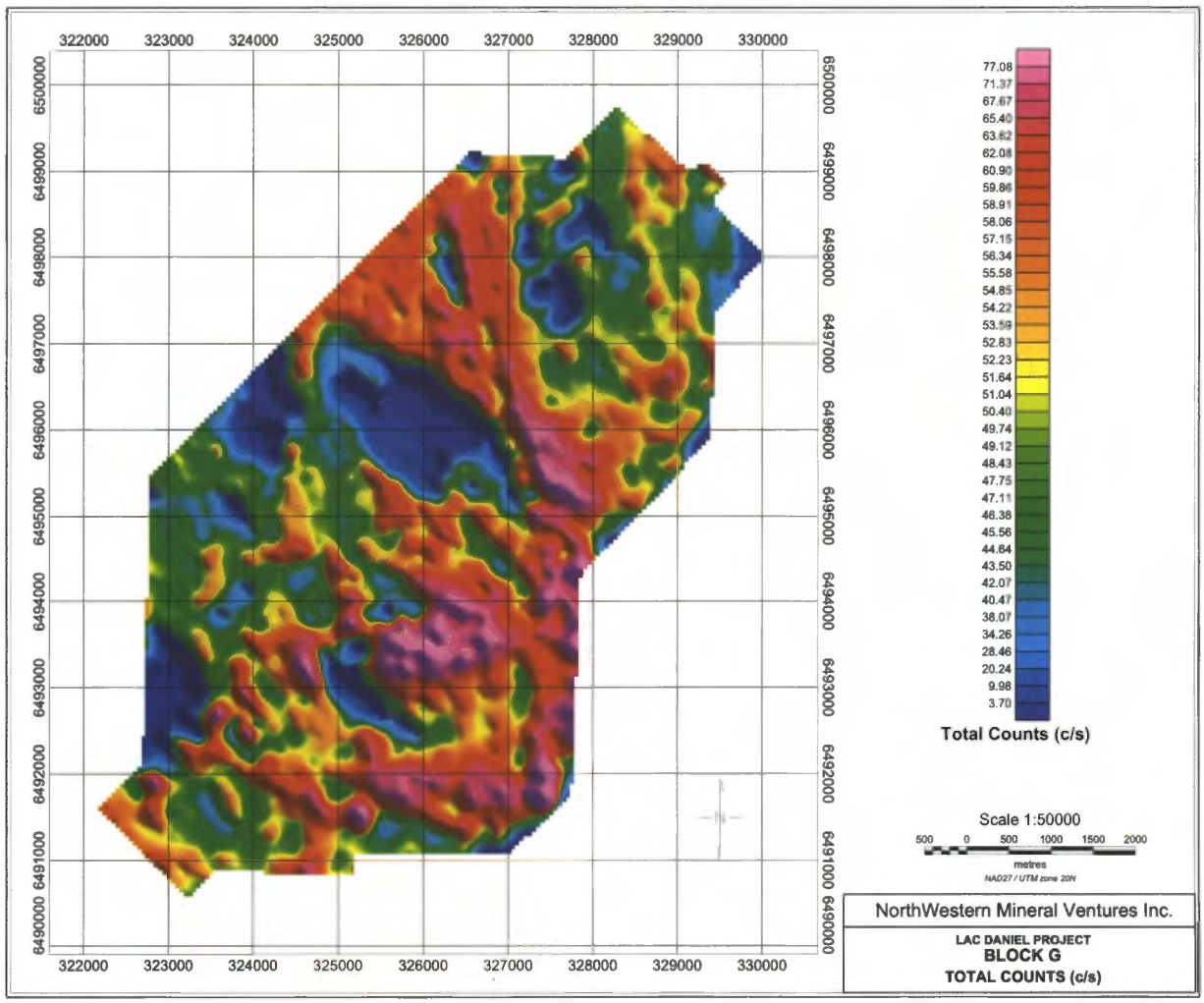


**Figure 44: Total Counts (Block G)**

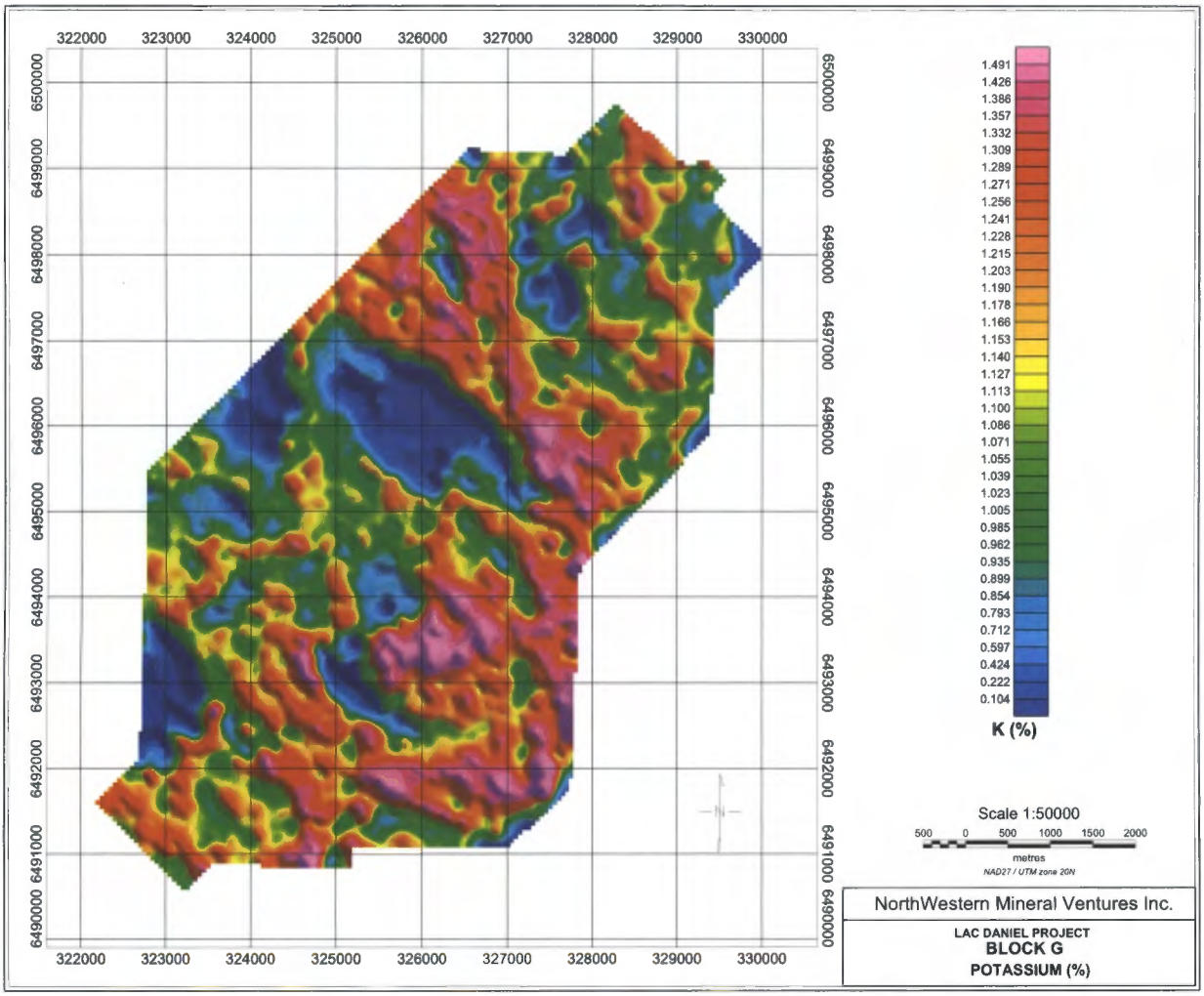


**Figure 45: Potassium (%) (Block G)**

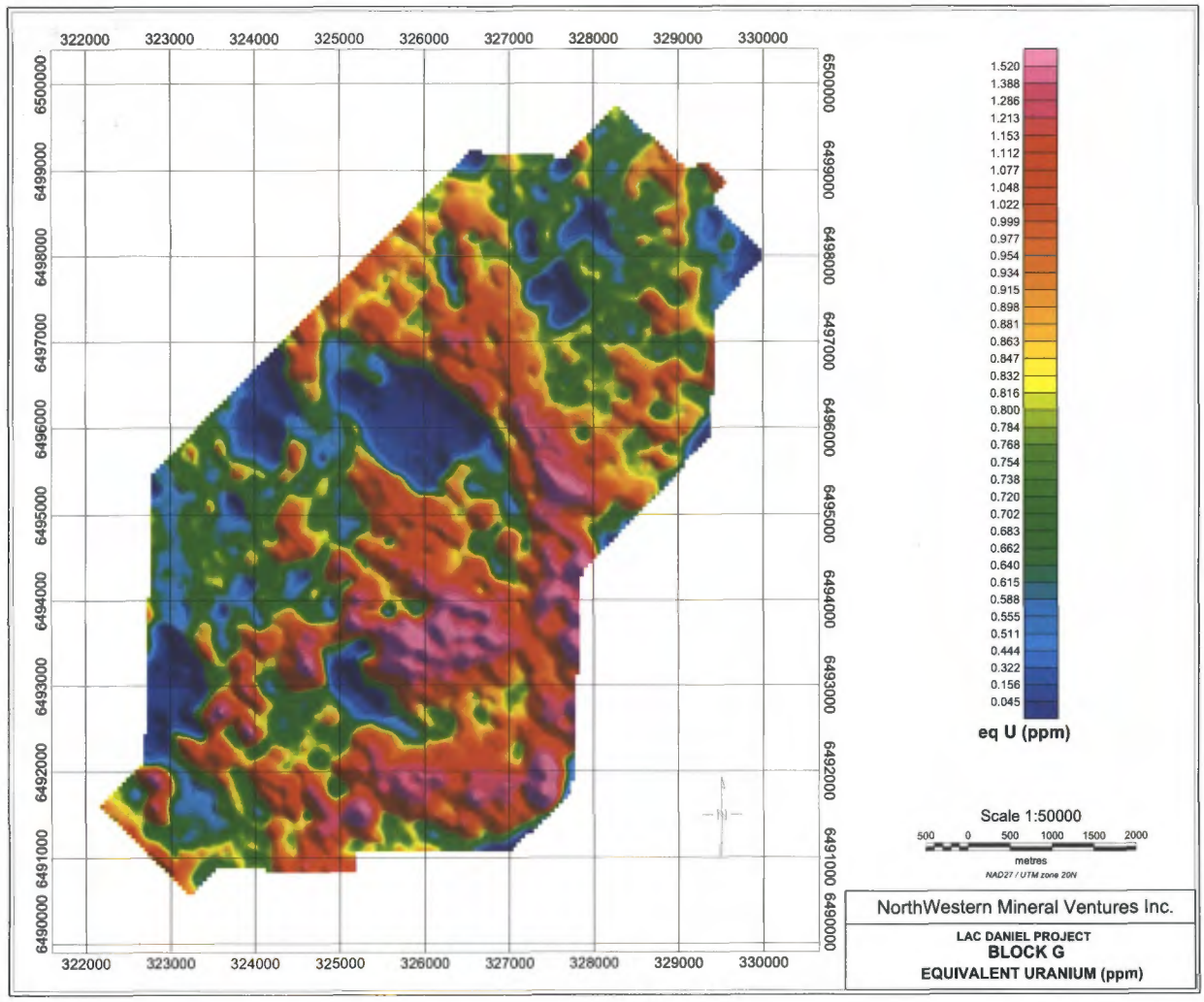


**Figure 46: Equivalent Uranium (ppm) (Block G)**

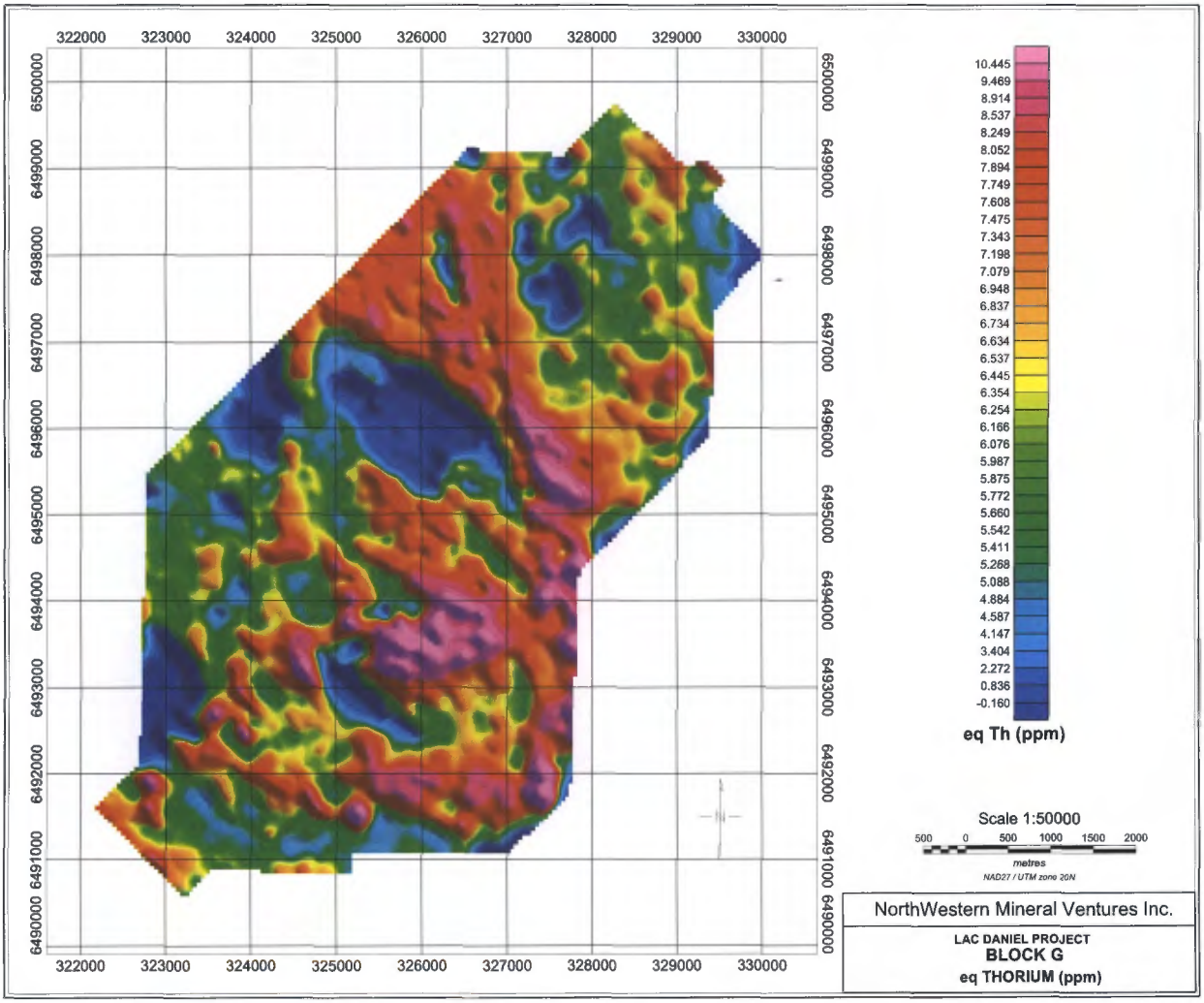


**Figure 47: Equivalent Thorium (ppm) (Block G)**

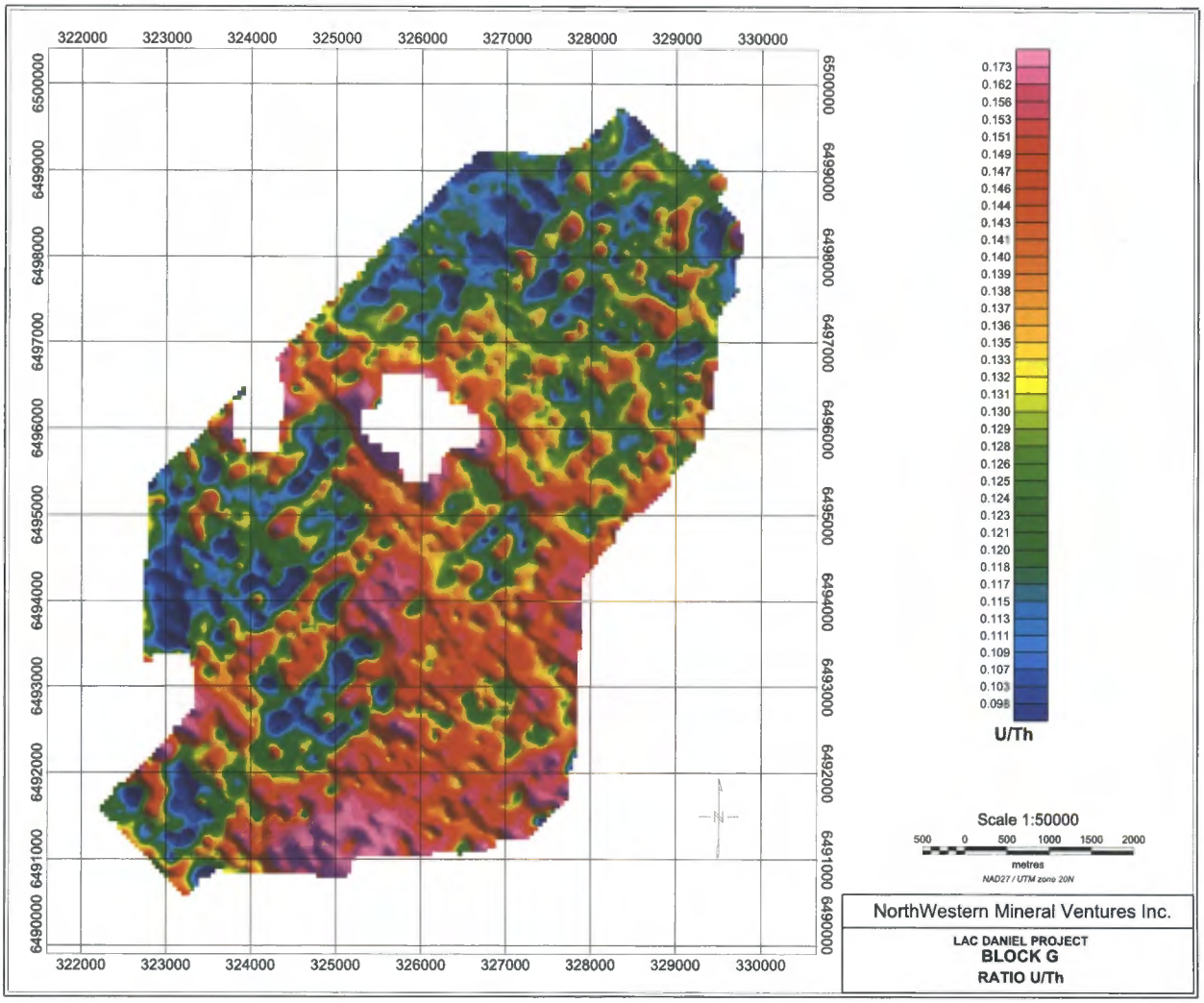


**Figure 48: Ratio U/Th (Block G)**

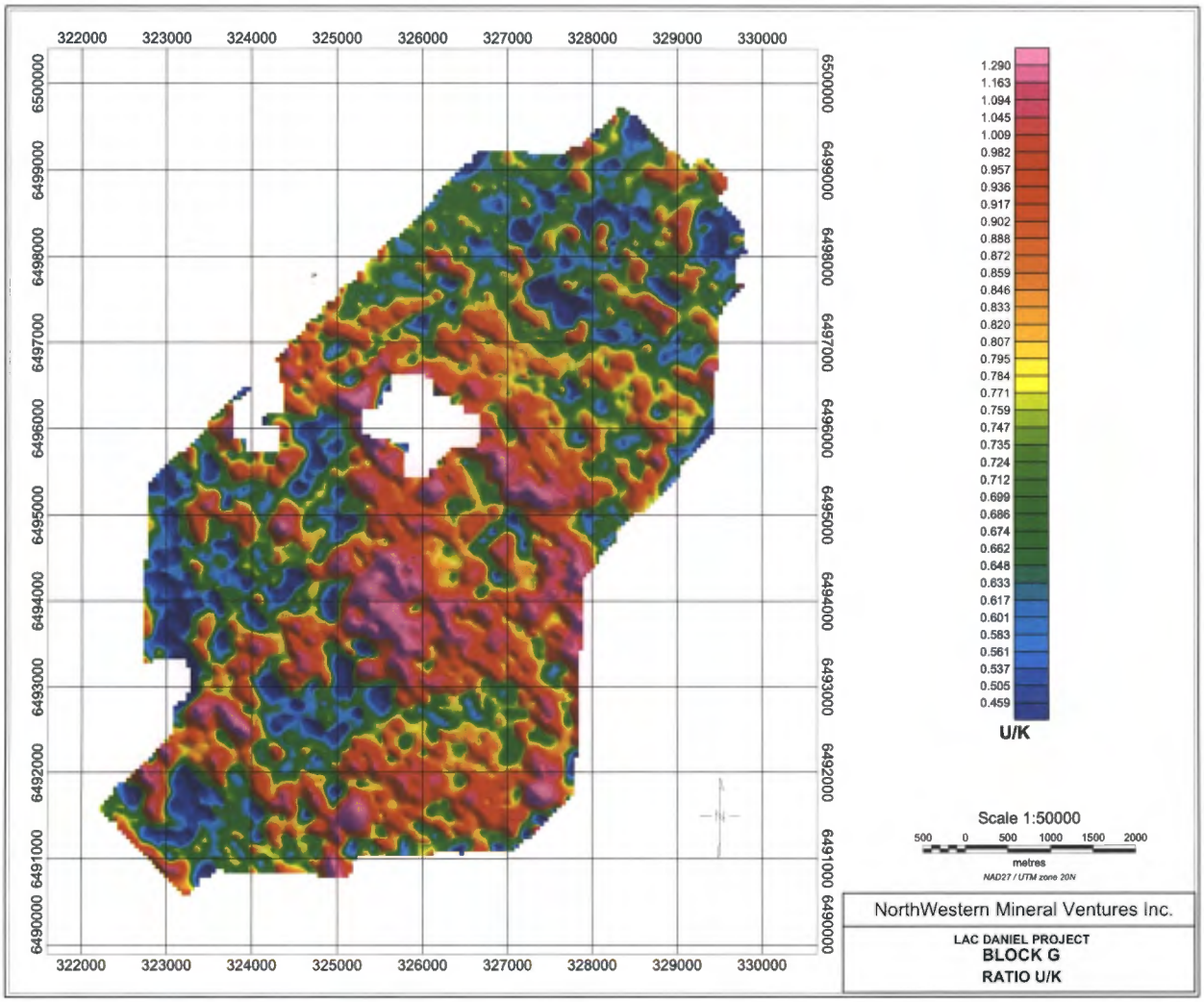


**Figure 49: Ratio U/K (Block G)**

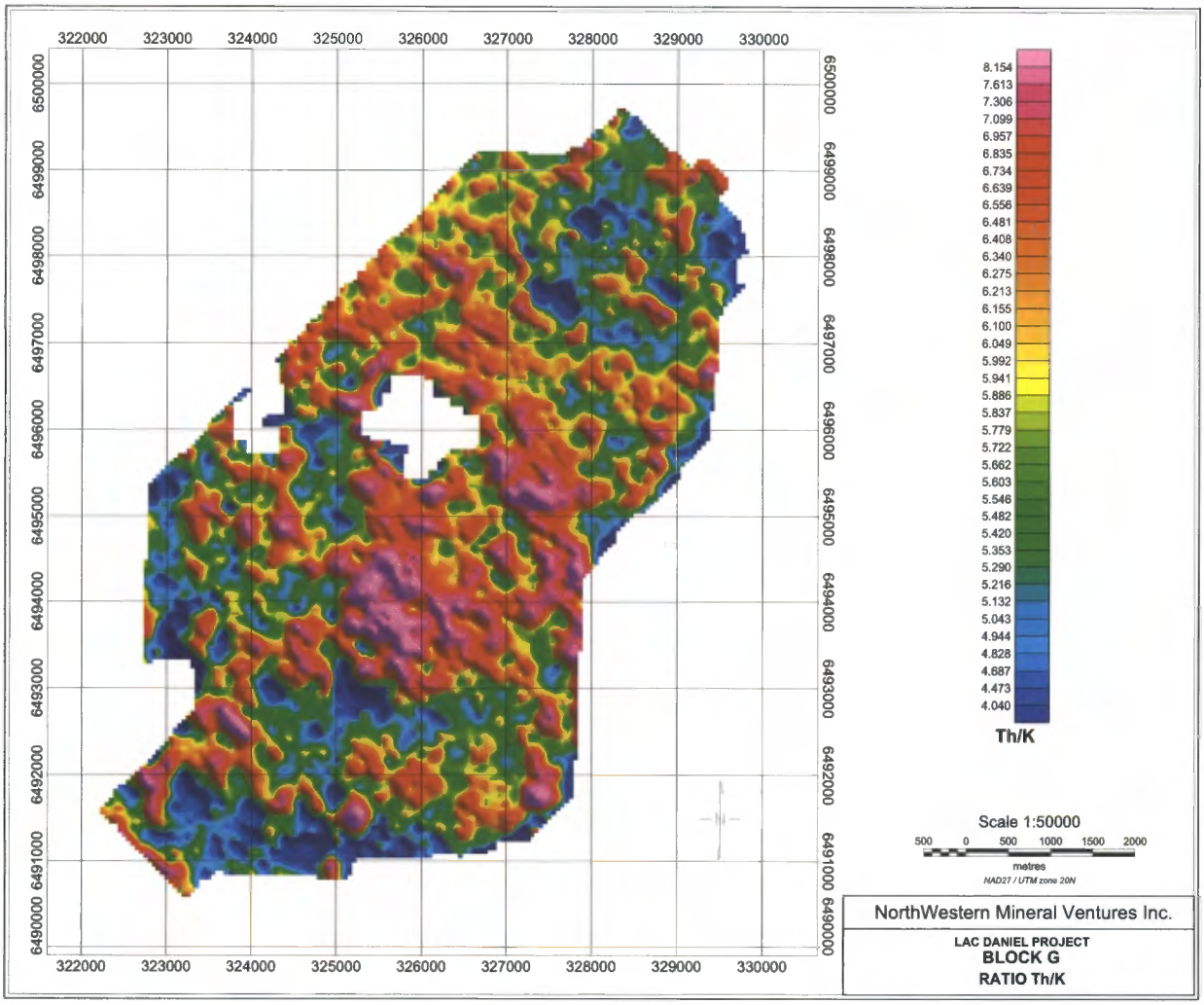


**Figure 50: Ratio Th/K (Block G)**

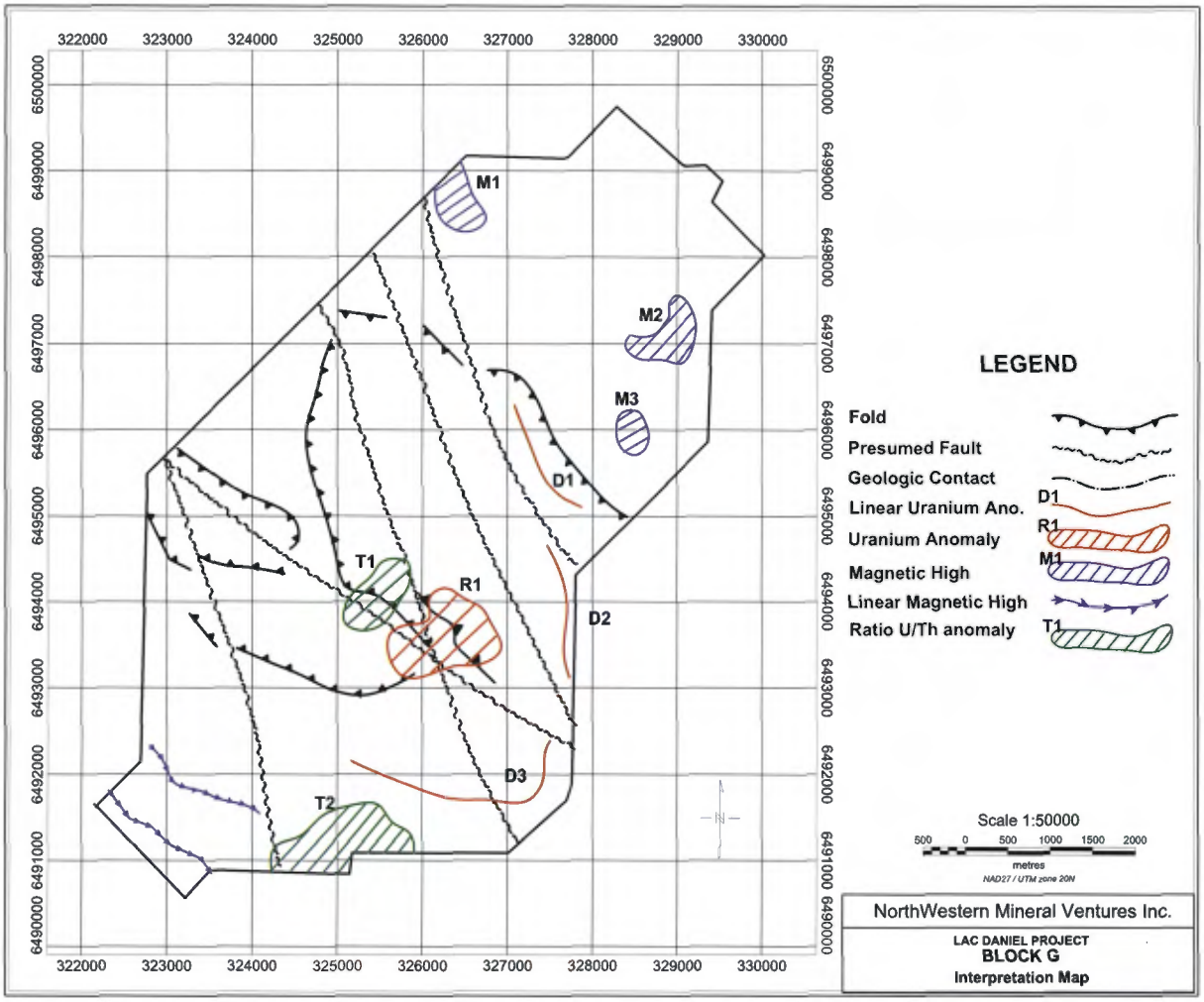


**Figure 51: Interpretation Map (Block G)**

## 6.0 CONCLUSIONS

The interpretation of an airborne magnetometer and gamma-ray spectrometer survey flown in September 2007 for **NorthWestern Mineral Ventures Inc.** allowed mapping of 15 significant spectrometric anomalies (table 6).

Ground follow up is recommended on all these priority targets (location with a portable spectrometer, rock sampling if possible, and if needed rock stripping or drill hole).

**Table 6: Selected Exploration Targets**

| Block | Anomaly | Co-ordinates (Nad27, z20N) | | Comments |
|---|---|---|---|---|
| | | X (m) | Y (m) | |
| ABE | R1 | 348 205 | 6 486 695 | Located near a geological contact, a N-S fault and a magnetic high. Good U/Th ratio. |
| | R7 | 348 650 | 6 468 130 | Seems to be related to the fold. Good U/Th ratio. |
| | R5 | 351 865 | 6 475 355 | Located along the Lac Daniel fault and crossed by a N-S fault. |
| | R4 | 348 725<br>348 082 | 6 475 530<br>6 476 797 | Long elongated anomaly with good U/Th ratio. |
| | R2 | 345 070 | 6 482 405 | Very large anomaly. Could be related to a granitic massif. |
| | R6 | 349 030 | 6 470 340 | Good U/Th ratio located along a N-N-W fault. |
| | R3 | 345 625 | 6 478 015 | Good U/Th ratio related to a magnetic high. |
| | D1 | 339 200<br>340 510 | 6 481 660<br>6 483 125 | 3 short linear anomalies with a fourth one located along the Lac Daniel Fault. |
| | D2 | 359 670 | 6 481 845 | 2 linear anomalies with poor U/Th ratios. |
| | D3 | 365 035 | 6 466 305 | A single linear anomaly with a medium U/Th ratio. |
| | D4 | 370 090<br>371 575 | 6 465 825<br>6 464 620 | 3 short linear anomalies along a geological contact. |
| | D5 | 377 725<br>371 205 | 6 468 690<br>6 459 175 | Many linear anomalies located near a geological contact, a fault and over a magnetic high. |
| C | T1 | 386 250 | 6 481 350 | One linear U/Th anomaly |
| F | R2 | 327 500 | 6 478 480 | U/Th anomaly with signal to noise ratio higher than 2 |
| | R4 | 327 800 | 6 476 380 | U/Th anomaly with signal to noise ratio higher than 2 |

It is hoped that the information presented in this report will be useful both in planning subsequent exploration efforts and in the interpretation of related exploration data.

Respectfully Submitted,

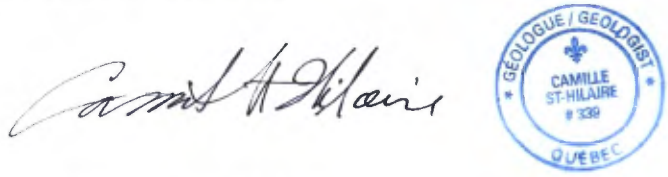


Camille St-Hilaire, M.Sc.A.
P.Geo.

# REFERENCES

Bhattacharya, B..K., 1966. Continuous Spectrum of Total Magnetic Field due to a Rectangular Body. Geophysics, vol.31, p.97-121.

Briggs, I., 1974. Machine contouring using minimum curvature, Geophysics, v.39, pp.39-48.

Cuney, M., 2006. U-deposit models. CREGU, Université Henri Poincaré. 176 pages

Duval, J., and Cook, M., 1971. Development of remote methods for obtaining soil information and location of construction materials using gamma-ray signatures for Project Tathemis. Rice University: Dept. of Geology.

Girard, R., 2007. Uranium Exploration Campaign in the Kangiqsualujjuaq George River Area, North Rae Project. Presented to NorthWestern Mineral Ventures Inc. by Ios Services Géoscientifiques Inc.

Grasty, R.L., 1975. Uranium Measurement by Airborne Gamma-Ray Spectrometry: Geophysics, v. 40, p. 503-519.

Hall, E.L., 1979. Computer Image Processing and Recognition: Academic press, Toronto.

Hovgaard, J., and Grasty, R.L., 1997, Reducing statistical noise in airborne gamma-ray data through spectral component analysis. In "Proceeding of Exploration 97: Fourth Decennial International Conference on Mineral Exploration", edited by A.G. Gubins, p.753-764.

International Atomic Energy Agency, Vienna, 1991, Airborne Gamma Ray Spectrometer surveying. Technical Reports Series no. 323.

International Atomic Energy Agency, Vienna, 2003. Guidelines for radioelement mapping using gamma ray spectrometry data. Technical Document 1363.

Lovborg et al. 1981, Pad Facility for the Calibration of Gamma-Ray Measurements on Rocks, RISO National Laboratory, Denmark. RISO-R-454.

Minty, B.R.S., 1992, Airborne gamma-ray spectrometric background estimation using full spectrum analysis. Geophysics, vol. 57, no. 2, p. 279-287.

Minty, B.R.S., 2003. Accurate noise reduction for airborne gamma-ray spectrometry. Exploration Geophysics (2003) 34, pp207-215.

Peters, L., 1949. The direct Approach to Magnetic Interpretation and its Practical Application. Geophysics, vol.14, p. 290-320.

Pilkington, M. and Keating, P., 1991. Recent advances in interpretation techniques for magnetic and gravity anomalies. In Interpretation of Gravity and Magnetic Anomalies for Non-Specialists. Note for Canadian Geophysical Union Short Course, January 23 and 24, 1991. Geological Survey of Canada.

Reford, M.S., 1964. Magnetic anomalies over thin sheets, Geophysics vol. 29, p. 532-536.

Reid, A.B., Allsop, J.M., Granser, H., Millet, A.J. and Somerton, I.W., 1990. Magnetic interpretation in three dimensions using Euler deconvolution. Geophysics, vol..55, p. 88-91

Spector, A., 1968. Spectral Analysis of Aeromagnetic Data, Ph.D. Thesis. University of Toronto, Toronto, Ontario, Canada.

Spector, A. and Grant, F.S., 1970. Statistical Methods for Iterpreting Aeromagnetic Data, Geophysics, vol.35, p. 293-302.

Taylor, F.C., 1979. Reconnaissance geology of a part of the Precambrian Shield, Northeastern Québec, Northern Labrador and Northwest Canada, memoir 393, 99 p.

Thompson, D.T., 1982. A new technique for making computer assisted depth estimates from magnetic data, Geophysics, vol.47, p.31-37

Verpaelst, P., Brisebois, D., Perreault S., Sharma, K N M, David, J., 2001. - Geology of the Koroc River Area and Part of the Hebron Area (NTS 24I AND 14L). 2001, Par 57 p. RG 2000-02